# UC San Diego
## UC San Diego Electronic Theses and Dissertations

**Title**

Controlled-Source Electromagnetic Studies of the Southern California Continental Shelf

**Permalink**

https://escholarship.org/uc/item/5j24w1ww

**Author**

King, Roslynn

**Publication Date**

2022

Peer reviewed|Thesis/dissertation

UNIVERSITY OF CALIFORNIA SAN DIEGO
SAN DIEGO STATE UNIVERSITY


Controlled-Source Electromagnetic Studies of the Southern California Continental Shelf


A Dissertation submitted in partial satisfaction of the requirements
for the degree Doctor of Philosophy


in


Geophysics


by


Roslynn Beatrice King


Committee in charge:

    San Diego State University
        Professor Jillian Maloney, Chair
        Professor Hilary McMillan

    University of California San Diego
        Professor Steven C. Constable, Co-Chair
        Professor Thomas E. Levy
        Professor Leonard J. Srnka


2022

The Dissertation of Roslynn Beatrice King is approved, and it is acceptable in quality and form for publication on microfilm and electronically.

University of California San Diego

2022

DEDICATION

To my parents and my sister, who first taught me how to explore and to my partner, who inspires

me to keep at it.

EPIGRAPH

*'I don't know where I'm going, but I am on my way'*

-Voltaire

TABLE OF CONTENTS

# LIST OF FIGURES

# LIST OF TABLES

# ACKNOWLEDGEMENTS

I would like to thank my advisors Steve Constable and Jillian Maloney who have consistently given me the freedom and support to pursue research questions that interest me. I would like to thank Steve for providing me many opportunities to learn both in the lab and in the field. Under his guidance, I have had the opportunity to work with and troubleshoot nearly every EM instrument type available in so many diverse settings. This has been enriching both as a scientist, but also as a person. Steve has also taught me how to be a scientist, regularly providing me with guidance on how to pursue information, improve designs, and question models; it wasn't always easy, but I am so grateful for these lessons. Thank you, Steve, for all the patience, for the insightful conversations, and for believing and standing up for me as a scientist.

Jillian hooked me on marine science by taking me on my first cruise and I have since repaid her by devising the most boring cruise plans imaginable which she has enthusiastically helped with despite the inevitable monotony. Jillian made time to help me even when things were chaotic, showing me the ropes of cruise planning, thinking on the fly, and taking things in stride. She is a great role model, showing me when to be and when not to be calm and frequently helped me navigate the academic world and become more comfortable with the difficulty of pushing boundaries and the unknown.

I would also like to thank Amy Gusick, who I now consider a mentor and good friend, for her guidance and valuable conversations. Amy has always been the picture of enthusiasm and her excitement is contagious, continually inspiring me to get back on the water and reminding me that being a scientist is a joy and a privilege. It has been such a pleasure to work, talk, and laugh with her regularly and I hope we can continue to interrupt each other's lives with more research schemes in the future.

my highs and taking me out for adventures or drinks when it's time to decompress. I am so grateful for all the lunch breaks, pandemic Zoom sessions, late-night cruise shenanigans, and soccer matches.

I am immensely grateful to my partner Craig, who has been my strongest supporter throughout my PhD. Craig has been with me through thick and thin; he has moved across the country, made a long-distance relationship fun, and made it so easy for me to pursue my research goals. His support is often what keeps me in the fight when I'm feeling discouraged, and his support has never wavered. This man has an inhuman amount of patience; he's listened to every rant and presentation, been my rubber ducky, and read over countless scripts and drafts. I'm so lucky to have a partner and friend that brings out the good in me and infuses every day with a bit of fun and madness.

Last, but absolutely not least, I would like to thank my parents and sister who have always made me feel like I could do anything. My family first instilled a love of adventure, nature, and learning from a young age and encouraged me to be whomever I want to be. My mom and sister have both taught me through doing that women can do anything and I feel lucky to have been given role models right from the start. And I would like to thank my dad, who despite many talks with teachers about my fidgeting and over excitement, reassured me that my 'energy is going to come in handy one day'. Thanks for celebrating me for being me.

Chapter 4, in full, is a reformatted reprint of the material as it appears in: King, R. B., Constable, S., & Maloney, J. M. (2022). A case study in controlled source electromagnetism: Near seabed hydrocarbon seep systems of Coal Oil Point, California, USA. Marine and Petroleum Geology, 139, 105636.The dissertation author was the primary investigator and author of this paper.

Chapter 5, in full, has been submitted for publication. King, R.B. & Constable, S. How low can you go: an investigation of sensitivity and resolution with depth using towed marine CSEM systems. The dissertation author was the primary investigator and author of this material.

Chapter 6, in part is currently being prepared for submission for publication of the material. King, R.B., Gusick, A., Constable, S., Maloney, J.M. CUESI: A near seafloor CSEM system. The dissertation author was the primary researcher and author of this material.

VITA

| | |
|---|---|
| 2012-2014 | Physical Scientist, United States Geological Survey |
| 2014 | Bachelor of Science in Geological Engineering *with Honors,* Colorado School of Mines |
| 2014-2016 | Exploration Geologist, Nyrstar Mining, Gordonsville, Tennessee |
| 2016-2017 | Geologist, G3SoilWorks, Costa Mesa, California |
| 2018-2021 | Teaching Assistant, San Diego State University |
| 2022 | Doctor of Philosophy in Geophysics, University of California San Diego San Diego State University |

PUBLICATIONS

King, R. B., Constable, S., Maloney, J. M. (2022). A case study in controlled source electromagnetism: Near seabed hydrocarbon seep systems of Coal Oil Point, California, USA. Marine and Petroleum Geology. https://doi.org/10.1016/j.marpetgeo.2022.105636

King, R. B., Danskin, W. R., Constable, S., & Maloney, J. M. (2022). Identification of fresh submarine groundwater off the coast of San Diego, USA, using electromagnetic methods. Hydrogeology Journal. https://doi.org/10.1007/s10040-022-02463-y

Duross, C., Hylland, M. D., Hiscock, A., Personius, S., Briggs, R., Gold, R. D., Beukelman, G. S., McDonald, G.N., Erickson, B.A., McLean, A. P., Angster, S. J., King, R. B., Crone, A. J., Mahan, S. A. (2017). *Holocene surface-faulting earthquakes at the Spring Lake and North Creek Sites on the Wasatch Fault Zone: Evidence for complex rupture of the Nephi Segment* (Vol. 28, pp. 1-119). Utah Geological Survey.

DuRoss, C. B., Hylland, M. D., Hiscock, A., Beukelman, G., McDonald, G. N., Erickson, B., McKean, A., Personius, S. F., Briggs, R., Gold, R., Angster, S., King, R., Crone, A. J., Mahan, S. A. (2014). Paleoseismic investigation to determine the mid-Holocene chronology of surface-faulting earthquakes on the Nephi segment of the Wasatch fault zone, Utah and Juab Counties, Utah. *US Geological Survey, NEHRP final technical report.*

ABSTRACT OF THE DISSERTATION

Controlled-Source Electromagnetic Studies of the Southern California Continental Shelf

by

Roslynn Beatrice King

Doctor of Philosophy in Geophysics

University of California San Diego, 2022
San Diego State University, 2022

Professor Jillian Maloney, Chair
Professor Steven C. Constable, Co-Chair

This dissertation presents research exploring the application of marine electromagnetic methods toward studying the nearshore continental shelf. The shallow-water controlled-source electromagnetic (CSEM) method has been shown to be a useful tool to study continental shelves. This marine CSEM method uses a man-made source of EM energy that passes through seawater and propagates into the seafloor and to towed-receivers which measure the resulting electric fields. These fields are processed into amplitude and phase data and then inverted to image

xx

subseafloor electrical resistivity. Electrical resistivity, while not a unique identifier, can be indicative of porosity and pore fluids, mineral chemistry, melt, and temperature. Thus, the CSEM method is well-suited to identify and characterize a variety of features and systems, both anthropogenic and naturally occurring, within continental shelves.

Offshore San Diego, surface-towed CSEM data were collected to detect the possible offshore extent of the county's onshore aquifer. Little was known of the offshore character of the aquifer, making it vulnerable to over-extraction and saltwater intrusion. Thus, this survey mapped pore-fluid salinity and groundwater pathways offshore to better constrain the freshwater-bearing formation. The results mapped a previously unidentified aquifer extending offshore San Diego which contains considerable volumes of fresh-to-brackish water, doubling the known groundwater volume of the county, in both continuous lenses and isolated pockets that appear influenced by fault systems and shallow stratigraphy. Near Santa Barbara, California, a surface-towed CSEM survey was used to target marine hydrocarbon seeps (MHS) within Coal Oil Point seep field (COP) at intermediate depths (<400 m). The results show significant spatial variability of MHS within COP and indicate at least two previously unidentified subseafloor accumulation sites. The depth and lateral extent of these accumulation sites could constrain overall seep-emission models for COP. From these studies, it became evident that the resolution and sensitivity of marine CSEM systems should be formally tested. Thus, rigorous and practical resolution and sensitivity studies were conducted to better constrain the depth of inference for several CSEM systems. The results from these tests indicate that the depth of inference for CSEM systems is deeper than previously thought. Finally, motivated by the search for archeological sites submerged offshore, a new CSEM system capable of detecting subtle and

small targets in culturally and biologically sensitive regions was developed. Initial inversions from first deployments of the new system offshore the northern Channel Islands, California show significant improvement in resolution when compared to surface-towed CSEM systems.

# CHAPTER 1

# Introduction

## 1.1 Geologic and Anthropogenic Resources on the Continental Shelves

Sea-level rise following the Last Glacial Maximum (~20 kya) submerged millions of square kilometers of coastal landscape, obscuring many geologic phenomena, resources, and cultural sites from direct observation. This submerged region is part of the continental shelf and plays an important role in human life from a political, industrial, and conservational perspective. The shelves are an extension of a present nation's land territory into the marine environment, allowing for exploration, conservation, and management of both living and non-living resources within and above the seabed, along with a variety of research and construction uses. As a result, the regions adjacent to the shelves are areas of intense industrial and recreational activity, and are associated with dense human populations which can put significant strain on local natural resources and ecosystems. In Southern California, ancient and modern human activity is evident along the coastline, from the presence of oil rigs on the continental shelf, water extraction wells that lie in close proximity to the present shoreline, and archeological sites half eroded by modern wave action. These features highlight coastal community interactions with, and the reliance upon, resources that lie just offshore on and within the continental shelf.

Traditionally, the subseafloor of the continental shelf is mapped and investigated using the seismic method, which is a valuable geophysical tool but is not sensitive to all physical properties. Thus, the marine controlled-source electromagnetic (CSEM) method has experienced

significant development in the past few decades (Constable, 2010), as the method can be sensitive to geology and features that have little or no seismic signature. The marine CSEM method uses a man-made source of EM energy to pass an electrical current through the seawater and seafloor, along with receivers that record the electric fields. These recorded fields are proportional to electrical resistivity which, although not a unique identifier, can be indicative of porosity and pore fluids, mineral chemistry, melt, and temperature. Thus, marine CSEM studies can yield important new datasets to better inform on the natural world, especially when investigating submarine fresh groundwater, hydrocarbons, and archeological sites.

This dissertation examines the use and development of marine CSEM systems on the continental shelf toward mapping and characterizing a variety of resources of geologic or anthropogenic origin at a variety of scales. Additionally, the works presented are an effort to collect baseline data to better understand and constrain geologic and cultural resources on the continental shelf offshore Southern California. Most of the work presented here uses a surface-towed CSEM system originally developed to map permafrost off Alaska (Sherman et al., 2017), but will also describe a new bottom-towed system developed for shallow shelf waters.

Chapter 2 will introduce the modern marine CSEM method. This chapter will focus on the advancement of marine CSEM through the past 4 decades from the deep marine environment until the present day, when CSEM systems can be used in water depths as shallow as 5 meters. Migration of CSEM systems into shallow water and even to the water surface has resulted in better navigational constraints, which has reduced one of the sources of noise in the method. Chapter 2 will highlight the processing workflow to take advantage of the increased signal to noise available with the shallow CSEM systems.

Chapter 3 will present results from a marine CSEM survey targeting fresh submarine groundwater that extends offshore San Diego, California. San Diego County is vulnerable to water shortages in the coming decades as snowpack in the Sierra Nevada Mountains and the water flow in the Colorado River declines (Udall & Overpeck, 2017). As such, the county is adopting policies to decrease water use and to develop additional local sources of water. Of these local sources of water, the main source of groundwater for San Diego County comes from a reverse osmosis plant that purifies brackish groundwater from the coastal San Diego Formation (SDF). The SDF has been extensively studied onshore, but little was known about the geology or groundwater quality offshore in the adjacent continental shelf. Because most groundwater systems are interconnected and complex, further analysis was needed to identify offshore geology, possible sequestration of freshwater in the shelf, and potential pathways for saltwater intrusion. This comprehensive understanding is important because seawater intrusion may limit use of the SDF and longevity of desalination facilities. Chapter 3 will present results from a series of surface-towed CSEM surveys designed to better constrain the pore-fluid salinity and possible fluid pathways in the continental shelf off the coast of San Diego. The results indicate a considerable volume of fresh-to-brackish water sequestered in the shelf, doubling the known freshwater volume of the SDF, in both continuous lenses and isolated pockets that appear influenced by fault systems and shallow stratigraphy. Fresh submarine water and the offshore portion of the SDF had not been mapped or studied prior to the study presented here.

Unlike submarine groundwater studies, the use of CSEM systems for the exploration of hydrocarbons offshore is an established and popular method used by industry. Yet, CSEM techniques have not been used to study the shallow character of hydrocarbon seeps on the shelf, which can contain pathways for upward fluid migration to the seafloor, releasing significant

volumes of greenhouse gases and hydrocarbons into the atmosphere and hydrosphere. These marine hydrocarbon seep systems have been studied using side scan sonar, multibeam bathymetry, seismic profiling systems, gas capture systems, airborne spectroscopy, remote operated vehicles, and many others (Hornafius et al., 1999; Leifer et al., 2006; Mitchell et al., 2018; Razaz et al., 2020). However, seeps can be temporarily inactive or migrate and these methods rely on seafloor observations or water column data which can lead to an incomplete understanding of the overall seep emission rates and activity. Chapter 4 details a case study of using CSEM to map and characterize the marine hydrocarbon seep system near Coal Oil Point, Santa Barbara, California to a depth of approximately 400 meters below the seafloor. The results of this study indicate significant spatial variability of the seafloor expression of the seeps and identify two previously unidentified intermediate depth accumulation sites of hydrocarbons. The existence of intermediate hydrocarbon accumulation sites was previously proposed from emission rate models (Leifer, 2019), but the depth and number of accumulation sites were unknown. Thus, the depth and lateral extent of the hydrocarbon accumulation sites identified beneath Coal Oil Point in the study presented in Chapter 4 may improve seep emission models for this seep field.

During the process of interpreting and presenting the work in Chapters 3 and 4, reviewers and other observers often assumed that the sensitivity and resolution of the towed CSEM systems were similar to nodal CSEM systems. However, there were several indicators from these and other studies that towed systems appear to have improved depth of investigation, but the issue was not formally studied and published. As it is important to understand the depth of investigation both when planning a survey and when interpreting inversions, it became apparent that a rigorous test of sensitivity and resolution with depth was needed. Chapter 6 describes a

series of two-dimensional sensitivity tests that expand upon tests first described by Parker (1982) and quarterspace tests on resolution with depth. The results highlight the importance of investigating data fit and possible signs of bias in residuals when interpreting data. The results show that when source receiver offset is held constant the towed CSEM systems have significantly better resolution and sensitivity to targets at depth compared to nodal CSEM systems.

Bottom-dragged marine EM systems can achieve higher sensitivity and resolution within the shallow subseafloor compared to other towed CSEM systems. However, these existing EM systems are limited to seafloor settings that are heavily sedimented and without protective status, eliminating many seafloor areas from study. Thus, when a project was launched in a National Park to identify archeological sites from Pleistocene hunter-gatherers for protection and study, these original EM systems were not appropriate for use. Instead, a new neutrally buoyant CSEM system was developed to fly between 1 to 2 meters above the seafloor thereby minimizing impact on the seafloor. Chapter 5 describes the process of developing a novel bottom-towed CSEM system and the resulting resistivity models. The new system known as 'CUESI' shows promising sensitivity to slight changes in porosity of the seafloor when compared with adjacent sediment core data and significant improvement in resolution when compared to surface-towed CSEM systems.

## 1.2 References

Constable, S. (2010). Ten years of marine CSEM for hydrocarbon exploration. Geophysics, 75, 75A67–75A81.

Hornafius, J. S., Quigley, D., & Luyendyk, B. P. (1999). The world's most spectacular marine hydrocarbon seeps (Coal Oil Point, Santa Barbara Channel, California): Quantification of

emissions. Journal of Geophysical Research: Oceans, 104(C9), 20703–20711. https://doi.org/10.1029/1999jc900148

Leifer, I. (2019). A Synthesis Review of Emissions and Fates for the Coal Oil Point Marine Hydrocarbon Seep Field and California Marine Seepage. In Geofluids (Vol. 2019). Hindawi Limited. https://doi.org/10.1155/2019/4724587

Leifer, I., Roberts, D., Margolis, J., & Kinnaman, F. (2006). In situ sensing of methane emissions from natural marine hydrocarbon seeps: A potential remote sensing technology. Earth and Planetary Science Letters, 245(3–4), 509–522. https://doi.org/10.1016/j.epsl.2006.01.047

Mitchell, G. A., Orange, D. L., Gharib, J. J., & Kennedy, P. (2018). Improved detection and mapping of deepwater hydrocarbon seeps: optimizing multibeam echosounder seafloor backscatter acquisition and processing techniques. Marine Geophysical Research, 39(1–2), 323–347. https://doi.org/10.1007/s11001-018-9345-8

Parker, R. L. (1982). The existence of a region inaccessible to magneto-telluric sounding (Vol. 68). https://academic.oup.com/gji/article/68/1/165/704026

Razaz, M., di Iorio, D., Wang, B., Daneshgar Asl, S., & Thurnherr, A. M. (2020). Variability of a natural hydrocarbon seep and its connection to the ocean surface. Scientific Reports, 10(1). https://doi.org/10.1038/s41598-020-68807-4

Sherman, D., Kannberg, P., & Constable, S. (2017).  Surface towed electromagnetic system for mapping subsea Arctic permafrost.  Earth and Planetary Science Letters, 460, 97—104.

Udall, B., & Overpeck, J. (2017). The twenty-first century Colorado River hot drought and implications for the future. Water Resources Research, 53(3), 2404–2418. https://doi.org/10.1002/2016WR019638

# CHAPTER 2

# Marine CSEM Development and Data Processing

## *2.1 The development of marine controlled-source electromagnetic methods*

The marine controlled-source electromagnetic (CSEM) method is a relatively new remote sensing tool for characterizing the subseafloor of the marine environment. The CSEM method is sensitive to changes in resistivity which can be a measure of the porosity, permeability, and resistivity of pore fluids within a material. Thus, the CSEM method can be used to image a variety of targets such as melt layers, freshwater lenses within the seafloor, gas hydrates, or even paleochannels to name a few examples. Furthermore, the CSEM method can be used as a powerful complimentary noninvasive tool paired with more established remote sensing techniques such as acoustic reflection methods to reduce non-uniqueness in models or better constrain the pore space of materials within the seafloor.

Prior to the development of marine CSEM technique, magnetotelluric (MT) methods were primarily used to image changes in resistivity within the subseafloor. However, high frequency signals were lost due to attenuation in the water column using MT methods in deep water. The development of broadband MT instruments around the turn of the century provided another decade of higher frequencies to replace those lost to the water (Constable et al., 1998), but marine MT methods were and still are somewhat limited to long period data collection. Thus, in the early- to mid-eighties, the CSEM method was developed in the academic sector to achieve high frequency data collection to investigate the upper oceanic lithosphere (Constable, 1990; Cox, 1981; Cox et al., 1986; Flosadóttir & Constable, 1996). With increased sensitivity to

shallow crustal depths combined with the ability to image upper mantle structure, marine CSEM techniques were used to study a variety of features such as magma chambers and hydrothermal systems at mid-ocean ridges (e.g., Evans et al., 1994, 1999; MacGregor et al., 2001; MacGregor et al., 1998; Sinha et al., 1998).

From these first uses of marine CSEM, the method was noted to be sensitive to thin resistive layers within conductive sediments which is an attractive feature for oil and gas exploration as hydrocarbons are significantly more resistive than other seafloor sediment. Thus, marine CSEM was quickly adopted by the oil and gas industry as a tool for exploration and reservoir characterization in the early 2000s (Constable, 2010; Eidesmo et al., 2002; Ellingsrud et al., 2002; Hesthammer & Boulaenko, 2005; Srnka et al., 2006).The adoption of CSEM by industry advanced CSEM techniques, both by transitioning the use of the method into shallower water depths and by increasing available funds to improve the CSEM method. Interest from industry led to a steady inflow of funds to develop new CSEM instruments and processing and inversion software. The uptake of CSEM by both industry and academia in the early 2000s is evident in the steady rise in publications related to marine CSEM shown in Fig. 2.1. Key (2012) published a very similar graph detailing the use of EM in industry and academia, but Fig. 2.1 is updated exclusively for marine CSEM publications through 2020. Peer-reviewed papers published after 2020 are excluded as Covid-19 pandemic appeared to decrease the publication rate for almost all branches of the geosciences.
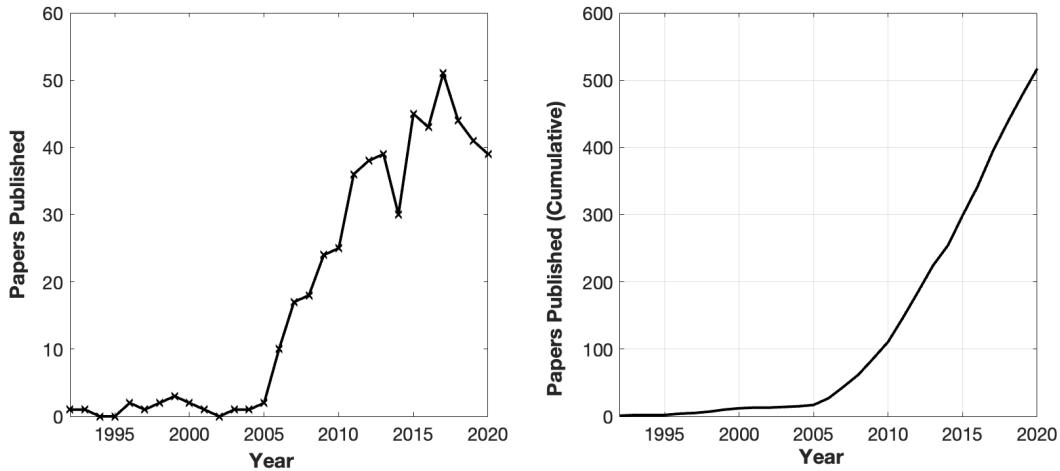
Fig. 2.1: The plot on the left is the number of papers published on marine CSEM per year until 2020. The right panel plots the cumulative papers published on marine CSEM until 2020. These panels show overall consistent growth over the last two decades. These plots are modified versions of the plots presented (Key, 2012) expanded to 2020 and limited to only show marine CSEM publications.

It is evident in the left panel of Fig 2.1, that there is an abrupt uptick in publications after 2005. This increase certainly contains industry papers related to offshore hydrocarbon exploration, but also is in part from increased interest in gas hydrate exploration. Gas hydrates can be potential hazards in offshore hydrocarbon drilling operations, but can also be a valuable energy resource for countries without more conventional sources of hydrocarbons. Before the early 2000's, seismic methods were typically used for gas hydrate detection as the presence of these materials would result in a bottom simulating reflector. A bottom simulating reflector can mark the phase change of solid hydrate above free gas (Shipley, 1979), but a bottom simulating reflector can also mark the presence of free gas without gas hydrate which leads to a non-uniqueness problem. As gas hydrates are more resistive than the surrounding sediment, Edwards (1997) first proposed the use of marine CSEM to help detect gas hydrates, but it was not until years later that this idea started to gain traction. Later, it was noted from well logs that resistivity of the sediments increases proportionally with hydrate volume fraction (Collett & Ladd, 2000).

Thus from 2006 onward, there has been an increasing number of studies investigating the use of CSEM to map and characterize gas hydrates offshore (Ellis et al., 2008; Evans, 2007; Harinarayana et al., 2012; Kannberg & Constable, 2020; Schwalenberg et al., 2010; Weitemeyer et al., 2006; Yuan & Edwards, 2000; Zach & Brauti, 2009)

Gas hydrates can be at or within in a few meters of the seafloor so increased sensitivity to shallow targets was favorable when detecting these features (e.g., Schwalenberg et al., 2010). Also, changes in resistivity from the presence of gas hydrates can be somewhat modest when compared to water saturated sediments so new CSEM techniques needed to be developed to improve the sensitivity of the method. Increasing the sensitivity and shallow resolution of CSEM systems would also enable the use of CSEM for mapping and characterizing paleochannels, hydrogeological systems, and even subtle changes in seafloor consolidation (Cheesman et al., 1993; Evans, 2001) Interest in mapping these shallow features propelled marine CSEM groups to work toward developing new methods of surveying and improve upon data processing and inversion techniques.

Typically, marine CSEM surveys were conducted using a towed source instrument that transmitted a frequency or time-domain signal that would be received by a series of bottom-deployed stationary receivers (see Fig. 2.2). These surveys, which will be referred to as a nodal CSEM surveys, result in variable source receiver offsets as well as potentially large (>50 km) transmitter-receiver offsets. The nodal survey design is sensitive to features several kilometers below the seafloor to only a few tens of meters below the seafloor. However, nodal surveys typically result in sparse datasets, which can decrease the resolution of the method, especially in the shallow subseafloor. So, as targets of interest became smaller and closer to the seafloor, such

10

as in the case of gas hydrates, new CSEM methods were developed that would result in denser data collection.
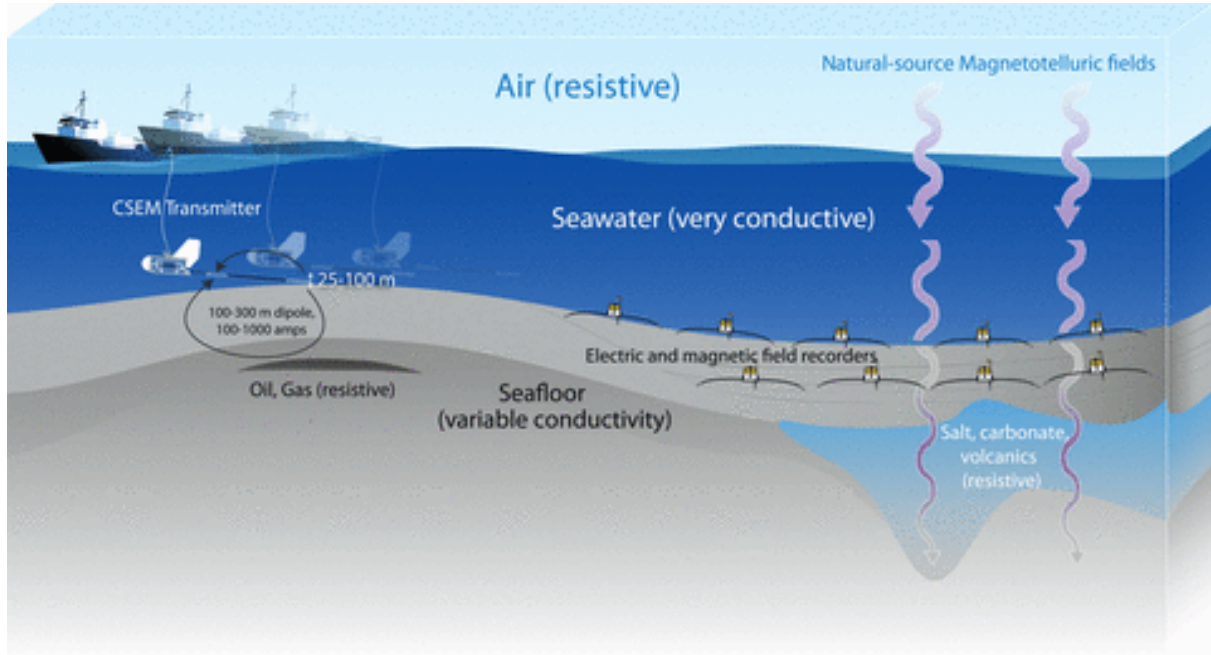


Fig. 2.2: Figure illustrating the typical arrangement of a nodal CSEM survey. Here a CSEM transmitter is towed above a series of bottom-deployed stationary receivers labeled here as 'Electric and magnetic field receivers'. This figure is from S. Constable (2013).

Increased data density was first addressed by continuously dragging both the transmitter and a tethered array of receivers over the seafloor. Initially, this new method involved very short tethers (<50 meters) between the transmitter and receivers as shown in Fig. 2.3, limiting the depth of investigation to only a few tens of meters below the seafloor (e.g., Cheesman et al., 1993). In later years, the depth of investigation increased as offsets between the transmitter and receiver were extended to up to 705 m (Schwalenberg et al., 2010). Several iterations of the dragged CSEM technique were tested over a variety of shallow targets such as groundwater lenses, hydrothermal vents, gas hydrates, and seafloor vents with promising results (e.g., Cheesman et al., 1993; Ellis et al., 2008; Evans, 2001, 2007; Goto et al., 2008; Schwalenberg et al., 2005, 2010; Yuan & Edwards, 2000).
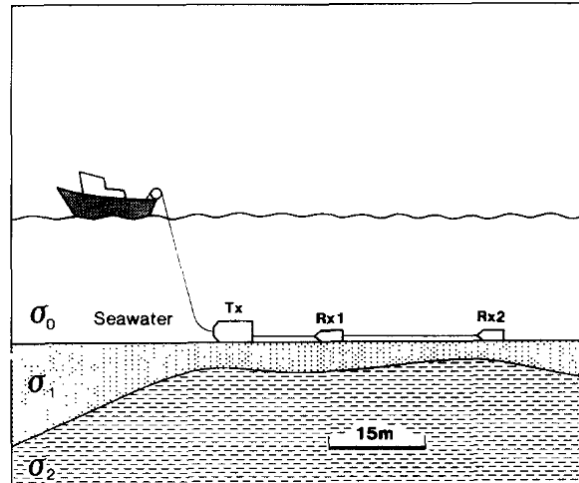
Fig. 2.3: Schematic of a bottom-dragged CSEM system. The transmitter is labeled here as 'Tx', followed by 2 receivers labeled 'Rx1' and 'Rx2'. This figure is from Cheesman et al. (1993).

The dragged CSEM systems have simple navigation, high frequency data collection at short source-receiver offsets, and maximum coupling with the seafloor. However, the use of such systems is limited to seafloor settings which are sedimented and without seafloor infrastructure. In order to expand the regions suitable for marine CSEM surveying, a new deep-towed CSEM system was developed (Weitemeyer & Constable, 2010). The first version of the deep-towed system was towed 60 meters above the seafloor and was designed as an electric dipole frequency domain system with a single 3-axis electric receiver towed 300 meters behind the transmitter. A novel frequency-domain waveform of a doubly symmetric square wave of Myer et al. (2011) was chosen for use so that a variety of depths could be investigated even with only one receiver. This is because the waveform of Myer et al. (2011) results in high amplitude responses over a wide range of frequencies allowing for a greater range of sampling depths. A horizontal electric dipole was chosen as the EM source because generating large signals (>100 Amp) on a dipole is more attainable than generating a similar magnetic signal (100 Amps) on a loop or coil of similar size. Additionally, a horizontal dipole transmitter alignment has the benefit of inducing both horizontal and vertical current flow which creates galvanic effects on both horizontal and vertical

boundaries unlike vertical dipole transmitters. Beneficial for simplifying surveying logistics, a horizontal dipole transmitter alignment also allows for in-line towing of the whole CSEM array.

Prior to the development of the deep-towed system, towed horizontal electric receivers were hypothesized to be prone to noise from streaming potentials related to towing the electrodes through conductive seawater (Evans, 2007). However, when the Scripps group tested this, it was observed that noise decreased with tow speed, rather than increase as would be expected from streaming potentials. It was inferred that lateral motion by the antenna cable in Earth's magnetic field was the source of the noise, which led to mounting the receiver electrodes on rigid arms. Towing CSEM systems above the seafloor reduced noise from seafloor interactions and allowed for the collection of vertical electric field data in addition to inline electric field data. Development of the deep-towed CSEM system first began in 2004, and within decade, the system had expanded to include 4 receivers and additional instruments to refine navigational data among other alterations. The current system is described by Constable et al. (2016) and an example of the array is shown in Fig. 2.4.
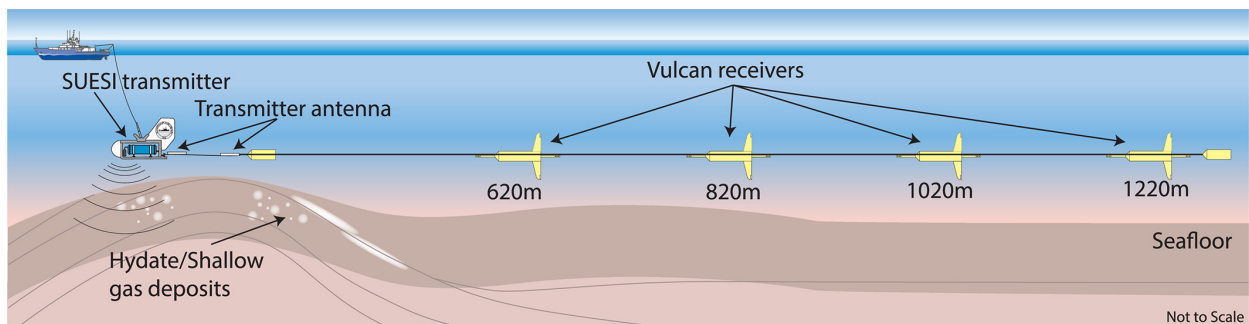


Fig. 2.4: Schematic of 1220 meter long bottom-towed CSEM array. Transmitter is labeled here as SUESI transmitter followed by transmitter antenna which function as a horizontal electric dipole. The 3-axis electric field receivers are labeled here as 'Vulcan receivers'. This figure is from Kannberg & Constable (2020)

## 2.2 Surface-towed CSEM

Following the successful deployments of deep-towed electric dipole receivers, development of a surface-towed CSEM system began at Scripps Institution of Oceanography in 2014 (Sherman, 2018). This system, known as the porpoise system, is shown in Fig. 2.5. The new surface-towed system packages repurposed receivers from the deep-towed system into buoyant PVC cases and, similar to the deep-towed system, holds the electrodes on rigid antennas to decrease noise associated with moving a cable in Earth's magnetic field (Constable et al., 2016). Unlike the deep-towed receivers, the surface-towed receivers only record the inline electric field because the vertical field disappears at the sea surface.

The proximity of the towed CSEM array to the sea surface led to four major benefits. First, each receiver is fitted with its own GPS mast which provides good constraints on navigation and a timing pulse which can later be used to obtain accurate phase drift. Second, the receivers do not need to transmit real-time depth telemetry as elevation is always at the sea surface. Third, towing speeds can be increased to up to 4 knots. And finally, since the transmitter did not need to be deep-towed, the transmitter is much smaller and simpler than deep-towed transmitters facilitating the use of much smaller vessels. The deep-towed transmitters of Southampton University and Scripps Institution of Oceanography are large, sophisticated instruments that generate large currents, allowing for deeper depths of investigation but requiring a specialized vessel for proper function. Conversely, the surface-towed system, which was originally developed to map permafrost in shallow waters near Prudhoe Bay, Alaska, needed to be deployed from small non-specialized fishing boats, operate off 110-240 VAC power, and be transported by airfreight and trucks (Sherman et al., 2017). To accomplish this, the transmitter is

kept onboard the ship and transmits the signal down cables which are towed in the water behind the vessel. The receivers are small and lightweight and can be easily disassembled for transport. With these modifications, the system is a mobile, cost-effective, and efficient new method to map the resistivity of the subseafloor to depths of up to 1000 meters in shallow (<200 meter water depth) marine environments such as on continental shelves.
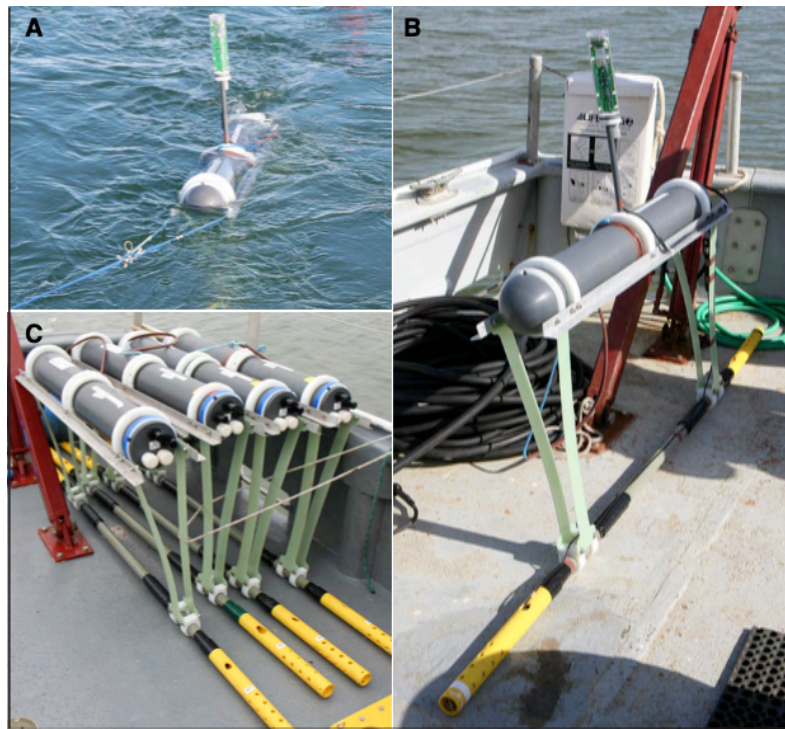


Fig. 2.5: A: Porpoise design as of 2015 floating on the surface after deployment. B: A porpoise on the deck ready for deployment. C: All four of the porpoises stored on deck; note that electrodes and GPS masts are not yet attached. This figure is from D. E. Sherman (2018).

The development of the porpoise system into the today's system illustrated and shown in Fig. 2.6 was iterative and has resulted in a system that can be deployed in under 45 minutes and can withstand a variety of ocean conditions. Today's porpoise frames have been redesigned to have a variety of points on the frame to secure cables, reducing snag points, and provide handholds. The frames of the most current system have been modified to slough off kelp and other ocean debris and provide a mounting point for a vertical GPS mast. The modern GPS mast,

15

as in the first iteration, functions both as a flashing beacon to improve visibility of the array, but also provides position data and timing for each porpoise. However, the GPS masts on the new system are not rigidly held upright like the prior versions, as this was noted to result in breakage if the mast encountered kelp, but instead are allowed to pivot backwards to reduce damage from floating debris while still recording navigational data. The navigational data, which includes speed, time, course over ground, and position data, is recorded on an internal serial logger which also records pitch, roll, and heading from an internal compass/tiltmeter every second. The rigid antennas for the electrodes have been moved to be slightly aft of the center of instrument and shielded by the frame, compared to the initial design, to reduce drag on the instrument and to decrease snagging from the antennas on ocean debris. Inline electric field responses from the silver chloride electrodes are recorded on one channel of a 250 Hz logger which also records acceleration in three directions on three other channels and a 1Hz timing pulse from the GPS mast on the fifth channel. The instrument at the end of the array, labeled 'dorsal' in Fig. 2.6, does not record electric field data, but instead records conductivity, temperature, and water depth on a serial logger. These data are later used to create starting models for inversions. In the initial system design, an instrument package like the dorsal was towed alongside the vessel. Today, the dorsal instrument is towed 30 meters behind the last porpoise and followed by a 30 cm diameter orange buoy which marks the end of the array to other ships, but also helps straighten the array when towing. The dorsal, like the porpoises, receives location data from an external GPS mast and records this data on a serial logger board.
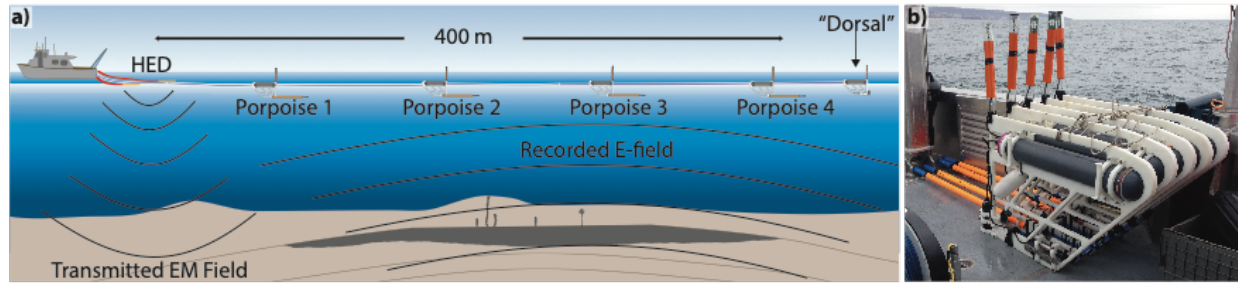
Fig. 2.6: a) Schematic of 400 meter long surface-towed CSEM array. Horizontal electric dipole is labeled here as 'HED'. The emitted electromagnetic field from the HED is labeled 'Transmitted EM Field'. b) Photo of all four modern porpoises (receivers) and dorsal (front) staged on deck. Logger is a grey pressurized case held in place with a white frame. GPS masts are orange vertical instruments affixed to the back of each white frame. The receiver frames have blue weights at the base to keep the instruments upright during towing operations. This figure is from King et al., (2022).

## 2.3 Processing and inverting CSEM data

Rather than a comprehensive description of CSEM processing and inversion, this section will describe the general method used in Chapters 3 and 4 of data processing and inversion relevant to data collected with the surface-towed CSEM system known as the 'porpoise' system (Sherman et al., 2017). Additionally, this section will highlight a variety of complications that are typically encountered during data processing and describe methods to identify and minimize complications.

## 2.3.1 Processing electric field data
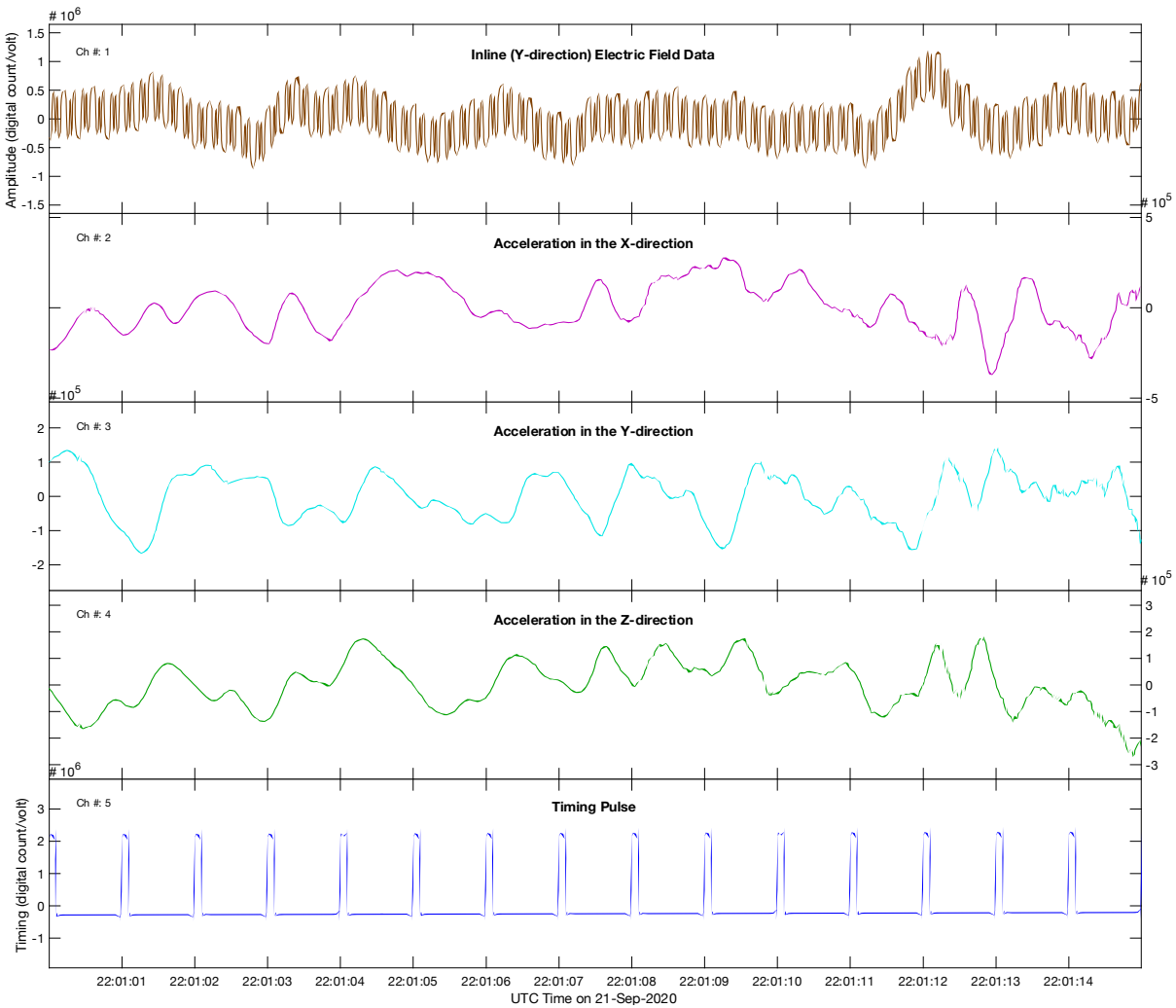


Fig. 2.7: Raw time-series recorded on a surface-towed CSEM logger for a receiver towed 300 meters behind the transmitter. Ch #.1 is the inline electric field data, Ch #.2, 3, and 4 are acceleration in 3 directions, and Ch #:5 is the timing pulse from the external GPS mast.

Data collected from the porpoise system are recorded as a time series which is shown in Fig. 2.7. In this example, the transmitter output a 32 Amp current-controlled 2.5 Hz waveform-D of Myer et al. (2011) on a 10 meter antenna. The inline electric field data was recorded on channel 1 while a 1 second timing pulse from an external GPS receiver was recorded on channel 5. To remove long-period magnetotelluric signal contamination and/or oceanographic noise from

the data and take advantage of the compact transmitted waveform, the time-series data collected on Channel 1 are pre-whitened in windows determined by the length of the first harmonic (in this example, 0.5 second windows), using first differencing. The data are then Fourier transformed into the frequency domain. The output frequencies will depend on which waveform was transmitted during the survey. In this example, a waveform-D was used which results in high amplitude responses over a broad frequency range as shown in Fig. 2.8. Considering the harmonic amplitude of this waveform and excluding any frequencies with less than 0.4 zero to peak amplitude, frequencies associated with the $1^{st}$, $3^{rd}$, $7^{th}$, and $13^{th}$ harmonics are included for further processing. Similarly, if a square-wave was transmitted, the harmonic amplitude falls off geometrically so, using the same 0.4 amplitude cutoff, the frequencies used in the Fourier transform would be only the $1^{st}$ and $3^{rd}$ harmonics. The complex numbers that are obtained from the Fourier transform are normalized by the source-dipole moment (320 amp meters in the example presented in Fig. 2.7) and corrected for receiver calibration. Finally, a post-darkener is applied to remove the effect of the pre-whitener.
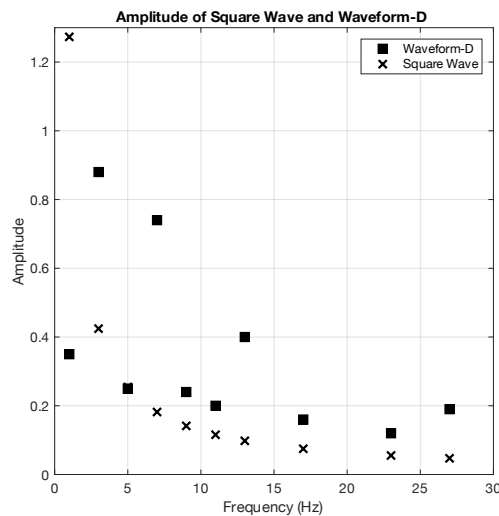


Fig. 2.8: Comparison of the amplitudes of waveform-D (Myer et al., 2011) with a square wave. The fundamental frequency of both waveforms is 1 Hz and the peak output cuttent is 1.

19

The complex transfer function estimates are stacked using an arithmetic mean to increase the signal to noise ratio and obtain an error estimate. Fig. 2.9 is a plot of the amplitude of the unstacked data versus the amplitude of the data stacked over a 30 second period and finally, the resulting signal-to-noise. The degree of stacking is dependent upon the survey conditions. For example, if there was significant wave action during the time of surveying, longer stacking windows may be necessary to reduce the effect of the oceanographic noise on the data.
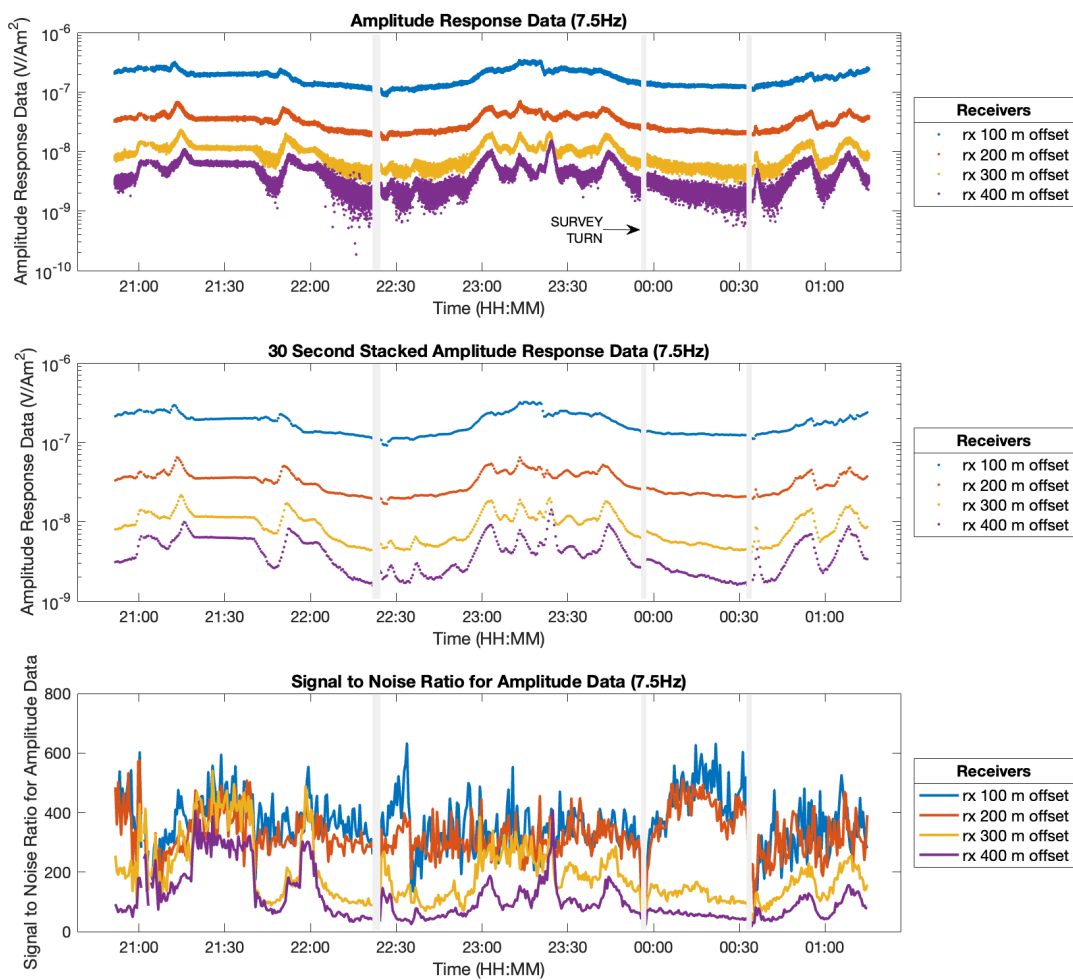


Fig. 2.9: The top panel is a plot of the amplitude of complex numbers yielded from the Fourier transform at 7.5 Hz on four receivers. The middle panel plots the amplitude data from 30 second stacks of complex numbers from the same data presented in the top panel. The bottom panel plots the signal to noise ratio for the same data. One may note that as distance between the transmitter and receiver increases, the signal to noise ratio decreases. The vertical grey bars indicate when the vessel and the array turning onto a new line in the survey.

20

## 2.3.2 Correcting for clock drift

The porpoise system is made up of a transmitter and four autonomous receivers towed on floating high-molecular-weight polyethylene rope. This instrument setup has the benefit of simplified deployments, recoveries, and surveying and, as each instrument is on the sea-surface, facilitates the use of an external GPS mast on each instrument. The GPS mast outputs location data, which is recorded on a serial logger, and provides a GPS stabilized 1 Hz timing pulse to each receiver. Before accurate timing was available, phase data have been historically much harder to model than amplitude data especially at higher frequencies. To remove or reduce the effects of timing errors on the phase data, clock drift is corrected using the 1 Hz timing pulse.

The inline electric field data are amplified, recorded, and time-stamped on an electric field logger that is regulated by an internal clock. This means that as the clock drifts, the electric field data will also appear to drift. Therefore, to have accurate phase data, the clock drift must first be calculated and then removed from the inline electric field data. One method to calculate the rate of drift is to assume a linear clock drift rate. Using this method, a time tag is recorded both before and after instrument recovery by synchronizing the internal clock with a GPS. Clock drift is then assumed to be linear between these two points in time so the slope of the clock drift can be calculated over the survey, converted to phase drift at various frequencies, and then applied to the data. However, in practice, this method can lead to inaccurate phase data as the internal clocks drift non-linearly depending on sea temperatures, battery, or other external factors. These small perturbations in drift rate are small (<0.002 ms over 20 seconds), but at higher frequencies such as 32.5 Hz, can result in a phase shift comparable to over 0.5% error in

phase. This amount of drift may seem inconsequential, but when phase data with 1% error floors are becoming more commonplace in CSEM studies, 0.5% error in phase is significant. Thus, instead of assuming linear drift rate, a dynamic clock drift rate is used, if possible, to effectively reduce error from clock drift.
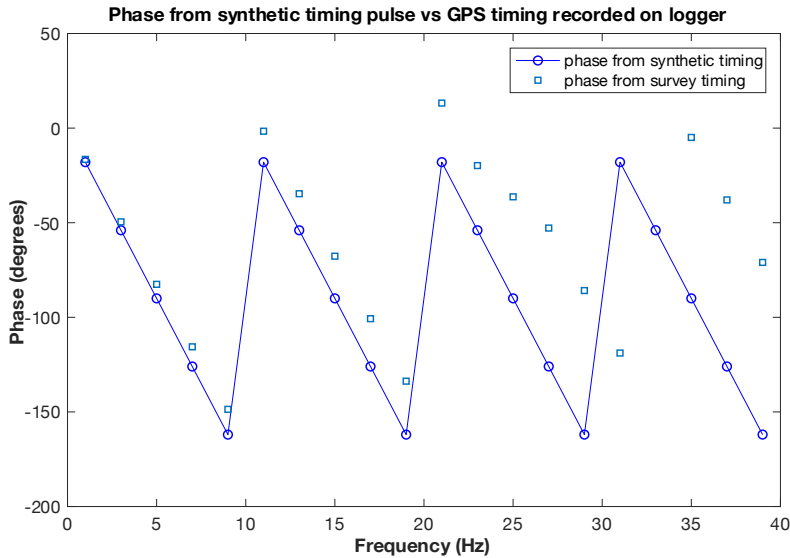


Fig. 2.10. Phase from a synthetic timing pulse versus phase from the GPS timing pulse recorded on logger. The deviation between the two datasets is the drift from the of the internal clock that regulates the logger.

Assuming dynamic clock drift, the timing pulse recorded on the loggers is processed as in section 2.3.1, but the windows used are adjusted to capture the timing pulse signal. The phase data from the GPS timing pulse recorded on the loggers is then compared to the phase from a synthetic timing pulse as shown in Fig. 2.10. The degrees of difference between the phase of the synthetic and recorded timing pulse is the drift from the clock. These values are converted into a vector of drift in seconds for the duration of the survey. Finally, the time drift per sampling interval of the survey can be scaled to represent drift for the frequencies used in the survey. This process results in a data array with the single column delineating the time of sampling and the

following columns recording degrees of drift with each harmonic (Fig. 2.11). The drift can now be applied to the phase data before further processing.
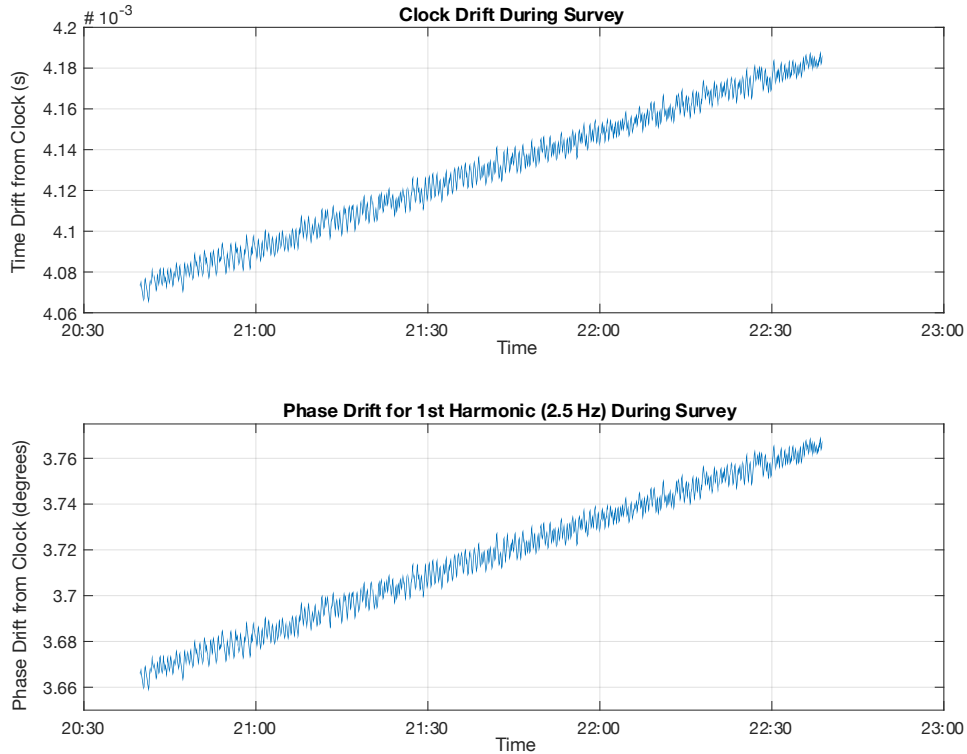


Fig. 2.11: Drift and drift corrections from one receiver. The top panel plots the time drift of the clock during the survey in seconds. The lower panel plots the related amount of phase shift that needs to be applied to the 2.5 Hz phase data to account for the clock drift shown in the top panel.

### *2.3.3 Processing navigational data*

Navigational uncertainties are typically the greatest source of error is CSEM surveys and so navigational data are inspected at nearly every point during processing (Myer et al., 2012). If all instruments functioned as designed, navigation can be simple; however, even with a complete set of navigation data, there can be some potential complications. A few examples: heading recordings within the serial loggers can be compromised by the batteries within the pressure cases, ocean debris can pull the instruments below the water surface resulting in gaps in the GPS

data stream, altimeter data can be inaccurate if there are bubbles in the water column or offline features, and currents may cause the array to 'crab' through the water. There is no single fix to identify and address these sources of error, but there are a few procedures that are useful to troubleshoot the navigation data. The output navigational data are plotted frequently and compared to cruise notes, expected values considering fixed offset distances, and sea-state records from nearby buoys. Bathymetric data are obtained from public sources and compared to the recorded data from the altimeter. And finally, electric field data are compared to forward models made using the processed navigational data.

### 2.3.4 Creating pseudosections

As 2D inversions can be computationally expensive, 1D forward models are a useful tool to check for bias in the data or model build before adding another dimension. Forward solutions are calculated for 1D models that use the water depth and seawater conductivity measured during the survey underlain by halfspaces ranging from 0.1 to 1000 Ωm. The forward solutions also include navigational data which uses depth, dipole length, heading, and pitch of the transmitter as well as transmitter-receiver offset, depth, and heading for the receivers. The forward solutions are then compared with the stacked amplitude and phase data from the survey to check for processing errors and incorrect assumptions. As seen in Fig. 2.12, the stacked amplitude data corresponds well with the forward responses from halfspaces between 1 and 5 Ωm which are expected values for the seafloor and subseafloor in this survey. This indicates that the data processing and model assumptions are reasonable and the processed data can advance to 2D inversions.

**1D Half-space model response vs. 400 m transmitter-receiver offset receiver amplitude data at 7.5 Hz**

Legend: Response to halfspace models
- 0.1 Ωm
- 0.3 Ωm
- 1 Ωm
- 2 Ωm
- 3 Ωm
- 5 Ωm
- 10 Ωm
- 20 Ωm
- 50 Ωm
- 100 Ωm
- 1000 Ωm

X-axis: Inline distance (m)
Y-axis: Amplitude (V/Am²)
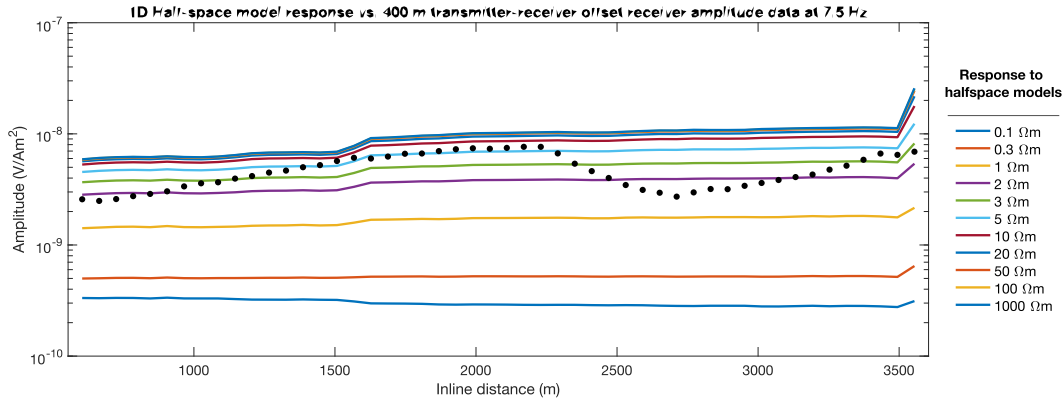
Fig. 2.12: 7.5 Hz amplitude responses from 1D halfspace models (solid lines) of varying resistivity compared with 7.5 Hz amplitude survey data (black dots) from a receiver towed 400 meters behind the transmitter.

If amplitude data are not in agreement with predicted responses, this may be an indicator of inaccurate assumptions or mistakes in data processing. This could be from an obvious source of error, such as inaccurate rotation of the data into a 2D space or reversing headings or pitch, but can also be indicators of model oversimplification. The processes described below provides a list of typical sources of error and methods to reduce error from model build or oversimplification.

If the forward responses are generally higher amplitude than the collected survey amplitude data, seawater conductivity may be higher than assumed. The surface-towed CSEM system measures seawater conductivity at the surface, but in some regions, stratification can occur in the water column leading to a varied conductivity profile. If this is not incorporated into the starting model, artifacts may be introduced into the final model to account for the water column resistivity. To avoid this, water conductivity with depth is typically measured during the survey. If survey was along the coastline (on the continental shelf) and no conductivity profiles were taken during the day of surveying or the conductivity sensor malfunctioned, one can usually find conductivity profiles from the time and day of surveying on the MEOP database

25

(https://www.meop.net/). Ocean currents can also cause complications while processing the data as currents that can cause the array to 'crab' through the water. This means that the depth profile generated from the instrument at the end of the array may not be representative of seafloor the receivers and transmitter passed over. A more representative depth profile can be built by downloading high resolution bathymetry data and taking 'slices' through it for each receiver and the transmitter location. If the 'crabbing' was minor and the bathymetry relatively simple, a depth profile can be found that represents the whole array to a reasonable degree. Finally, the depth profile is adjusted for tides either from nearby buoy data or by comparing the depth profile at the location of the dorsal instrument generated from public data with that of the survey data.

The 1D halfspace tests can be used to generate pseudosections which can provide a low-resolution resistivity profile of a given survey. Pseudosections are made by interpolating between forward responses to given halfspace models and the stacked amplitude data from the survey to find the apparent resistivity of each point of stacked amplitude data. The approximate depth of the apparent resistivity values can be roughly calculated using the source-receiver offset and the skin depth equation for each frequency (e.g., Weitemeyer & Constable, 2010) resulting in 2D plots of the resistivity of the subseafloor. Pseudosections have been noted to have a limited ability to constrain depth, but can be a good indicator of lateral variability of the dataset (Weitemeyer et al., 2006). Fig. 2.13 is a pseudosection using 7.5 Hz Amplitude data and Fig. 2.14 is a 2D vertical resistivity model from inverting the amplitude and phase data from the same survey line. One may note that the two models are in good agreement laterally, but the depths and definition of the structures vary between models. As previously noted, the depths used to create the pseudosection were found using the skin depth equation assuming a halfspace of 1

26

Ωm; it is evident from the inversion results that the subseafloor is more resistive, thus decreasing

the skin depth to around half of what was originally calculated.
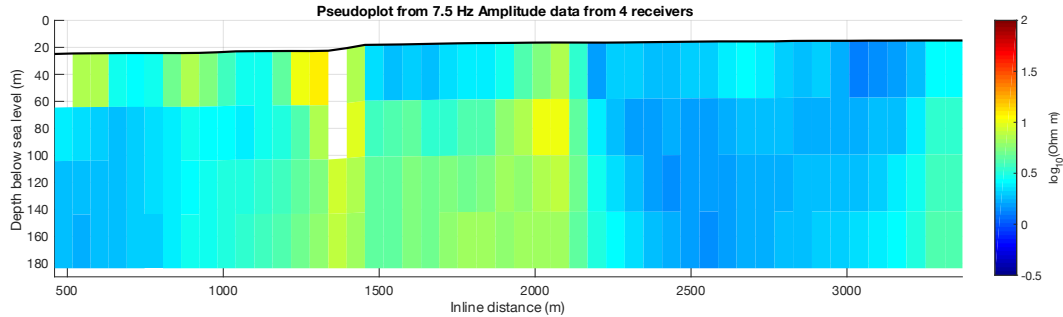


Fig. 2.13: Pseudosection of 7.5 Hz amplitude data from four recievers spaced 100, 200, 300, and 400 meters from the transmitter. The total depth of the profile was determined by skin depth assuming 1 Ωm sediment. There are four vertical pixels associated with the four receivers, with the shortest offset receiver profile corresponding to the shallowest profile and the longest offset receiver profile corresponding to the deepest profile. This pseudosection is from the same survey shown in Fig. 2.12.
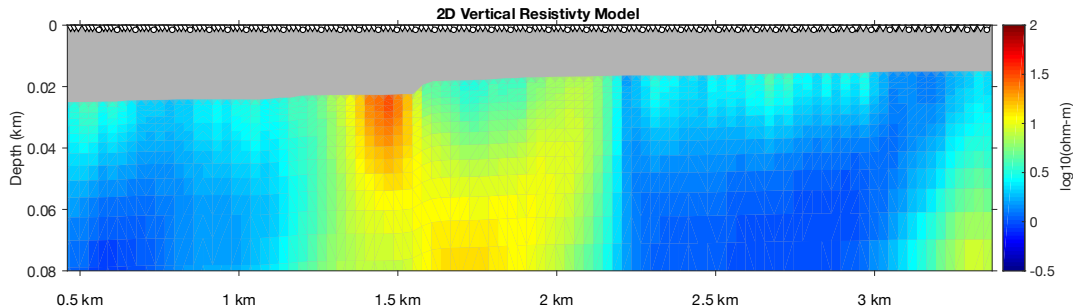


Fig. 2.14: 2D resistivity models of the same survey line presented in Fig. 2.12 and Fig. 2.13. The model was run with an anisotropic penalty weight of 0.05 and fit to a root mean square of 1. The amplitude and phase data were subjected to a 2% error floor in amplitude and 1% error floor in phase.

## 2.3.5 2D Model Build

While apparent resistivity pseudosections are a useful tool to understand the data prior to

inversion, 1D analysis does not take advantage of the density of data achieved with continuously

towed systems. Thus, 2D inversions can significantly improve the depth of investigation and

resolution compared to pseudosections or 1D analysis. Additionally, compared to pseudosections, 2D models use more of the available navigation data and allow for model penalties which can drive down uncertainty and improve the model fit to the data. This section will describe the general process of creating a 2D starting model for inversion using the publicly available MARE2DEM inversion code of Key (2016).

MARE2DEM is a finite-element adaptive modeling program that uses Occam's Inversion, a method that regularizes the inversion to obtain the smoothest resistivity model that fits the data (Constable et al., 1987). For marine CSEM surveys, the starting models are constructed with a series of fixed parameters and free parameters. The fixed parameters are typically made up of a highly resistive air layer underlain by the conductive ocean layer. The ocean layer can be divided into separate layers or sections to represent the water conditions during the time of surveying. For example, the ocean may become colder and thus more resistive past the continental shelf edge and this can be included in the model. Additionally, if combining magnetotelluric data with CSEM data, land may also be included in the model to reduce the coast effect (e.g., Constable et al., 2009; Wang et al., 2019).

The region below the seafloor is set as a free parameter with some starting resistivity value. The area below the seafloor can be parameterized using either parallelograms (quadrilateral grids) or triangles. The parallelogram parametrization uses a bathymetry conforming parallelogram mesh that can be set to increase in parallelogram height with depth below the seafloor. This mimics the loss of resolution of the EM method with distance. In areas with layered geology or a somewhat smooth seafloor, the parallelogram parametrization is an effective model grid. The triangle parametrization uses an unstructured triangular meshing

engine which can mesh complicated regions such as in areas with irregular bathymetry or

geologic structures. To carry out forward computations, the MARE2DEM code overlays a

triangular finite-element computation mesh onto the parameter mesh (the so-called dual grid

approach) which is then adaptively refined until the computational errors associated with the

mesh are below a set tolerance, usually 1%. This removes much of the burden from the user to

monitor and refine the computation grid or triangle size as the model develops structure to fit the

data because the code will automatically generate and refine the finite-element meshes with each

iteration (Key, 2016).

To stabilize the inversion, a roughness penalty is applied to the model. The model

roughness operator in MARE2DEM stabilizes the inversion away from creating artifacts in the

models (Key, 2022). In MARE2DEM the roughness penalties fall into two categories: anisotropy

and spatial roughness.

Anisotropy is a measure of how an electric field passes through a material given different

propagation directions. In the 2D code, anisotropic materials can have different resistivity values

in the vertical and horizontal directions, which is a good model for horizontally stratified

geology. Geologically, anisotropy is observed on a variety of scales originating from mineral

properties, rock or sediment texture, and macroscopic features such as in sedimentary horizons

(Constable, 2015). Anisotropy can be included in the MARE2DEM code and penalized to some

degree. A higher anisotropy penalty weight drives the model toward an isotropic solution,

penalizing any ratio above or below 1 between the vertical and horizontal resistivity values. A

lower anisotropy penalty weight does not heavily penalize the model if the vertical and

horizontal resistivities differ significantly (Key, 2016). Low anisotropy penalty weights can

result in overly smooth models because the inversions may reduce roughness by distributing

highly resistive or highly conductive features between the horizontal and vertical directions, thereby reducing the overall roughness in both directions (Constable et al., 2015). The degree of anisotropy needed in a model is challenging to discern and beyond the scope of this Chapter. More information on the effects of anisotropy on models can be found in a variety of publications (e.g., Constable et al., 2015; Kannberg & Constable, 2020b; Sherman et al., 2017).

However, in some survey areas, a priori knowledge on the geologic structure and characteristics of the area can allow for informed decisions on anisotropic ratios before building the models. For example, if gas hydrates are known to be within a study area, the initial inversions may include anisotropy because gas hydrate bearing sediments have been observed to have vertical resistivity values over an order of magnitude higher than the horizontal resistivity values (Cook et al., 2010). In a study characterizing gas hydrate in the California Borderlands, the authors determined the level of anisotropy needed by iterating upon the anisotropic ratio used in the models until a geologically feasible model and expected vertical to horizontal resistivity ratio was obtained (Kannberg & Constable, 2020).

In many instances, there is no expected level of anisotropy in a survey area. Initially, without prior evidence of anisotropy, isotropic inversions are run and scrutinized. If a root mean square of 1 is achieved and the misfit is normally distributed for both amplitude and phase, anisotropy may not be necessary in the model. If isotropic models do not result in a good fit to the data model fit can be examined for signs of anisotropy (Sherman, 2018). For example, during isotropic inversions of the data Sherman (2018) noted that if bias occurs in the phase residuals, but not in the amplitude data, this can be indicative of anisotropy. Thus, the degree of anisotropy can be better constrained by running a series of models using different anisotropy penalty weights until fit to both phase and amplitude data is achieved.
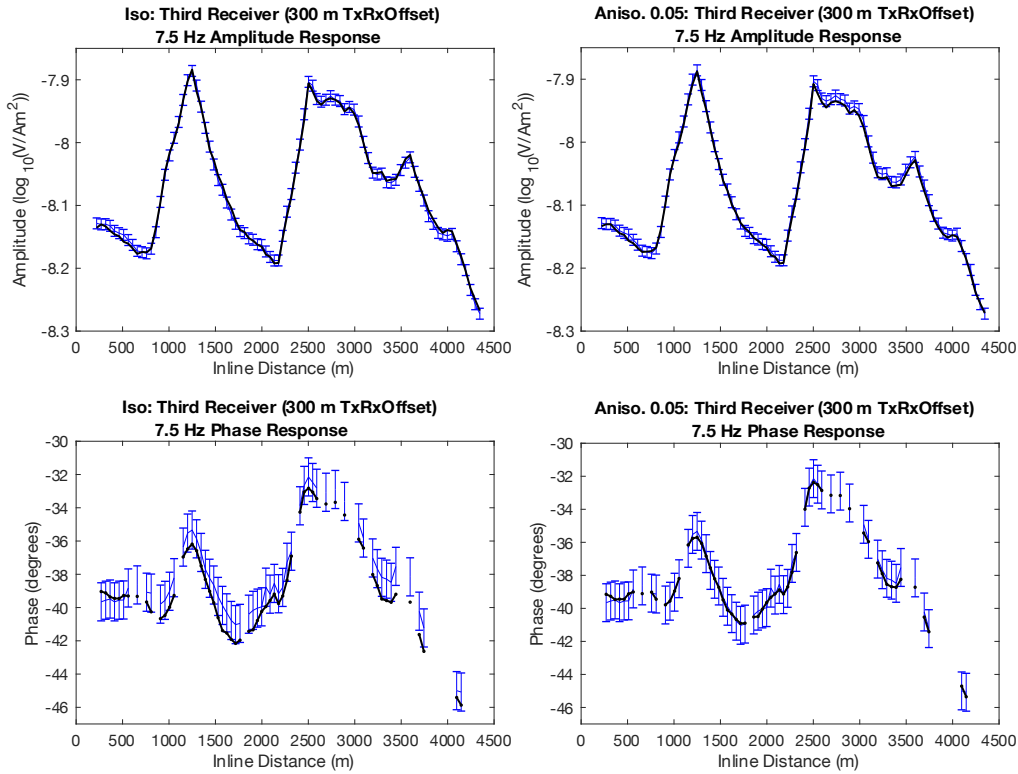
Fig. 2.15: The left two panels plot the data fit of both amplitude (top) and phase (bottom) from a receiver for the 10$^{th}$ iteration of an isotropic inversion of a surface-towed CSEM survey. The isotropic inversion could not reduce the root mean square below 1.13 and the modeled phase response appears to be biased high. The right two panels plot the data fit of both amplitude and phase from a receiver for an anisotropic inversion using an anisotropic penalty weight of 0.05 of the same surface-towed CSEM survey. The anisotropic inversion achieved a root mean square of 1 and the residuals for both amplitude and phase appear to be random.

As an illustration of Sherman's (2018) observations, in Fig. 2.15, the left two panels plot

the data fit of both amplitude and phase from a receiver for the 10$^{th}$ iteration of an isotropic

inversion of a surface-towed CSEM survey. The isotropic inversion could not reduce the root

mean square below 1.13 and bias was observed in the fit of the phase data. The right two panels

plot the data fit of both amplitude and phase from a receiver for an anisotropic inversion using an

anisotropic penalty weight of 0.05 of the same surface-towed CSEM survey. The anisotropic

inversion achieved a root mean square of 1 and the residuals for both amplitude and phase were

closer to zero-mean. Additionally, the vertical to horizontal resistivity ratios were found to align

well with nearby core data. Thus, the appropriate anisotropic penalty ratio was determined to be 0.05 in this instance.

In MARE2DEM, spatial roughness is penalized with both a horizontal and vertical penalty weight. The penalty ratio biases the inversion toward enhanced smoothness in the vertical or horizontal direction (Key, 2016). Geology or survey design is used to determine the appropriate vertical penalty weight. For example, the surface-towed CSEM system only measures the inline electric field which is more sensitive to horizontally oriented resistors than vertically oriented resistors. In this case, to avoid over-smoothing the changes in vertical resistivity from the horizontal resistors while also taking advantage of the dense data collection in the horizontal direction, a vertical penalty weight greater than 1 would be applicable. Conversely, in a heavily faulted region or an area with abrupt changes in lateral resistivity, a horizontal to vertical penalty weight of less than or close to 1 may be appropriate to avoid smoothing the changes in lateral resistivity.

### 2.3.6 Inversions and fit to data

Solutions to inversions are non-unique and unstable meaning that small to no changes in the data fit occur despite large changes in the model (S. Constable et al., 2015). This means that despite good fit to the data, the solution may not accurately reflect reality. However, models can be scrutinized to tease out the truth.

After the 2D models have been built and inverted using the MARE2DEM code, the resulting data fits are analyzed before interpreting the models. Initially, the amplitude and phase data for every receiver and frequency is inspected for fit. If overfitting is occurring, the error floors may need to be adjusted or error structure modified. If bias is forming in the residuals,

anisotropy, model build (bathymetry, water column, tidal effects, etc.), and navigational errors may also be the cause of the misfit. Only once the residuals are normally distributed and the data fit does not show signs of over or underfitting, the final resistivity models are accepted.
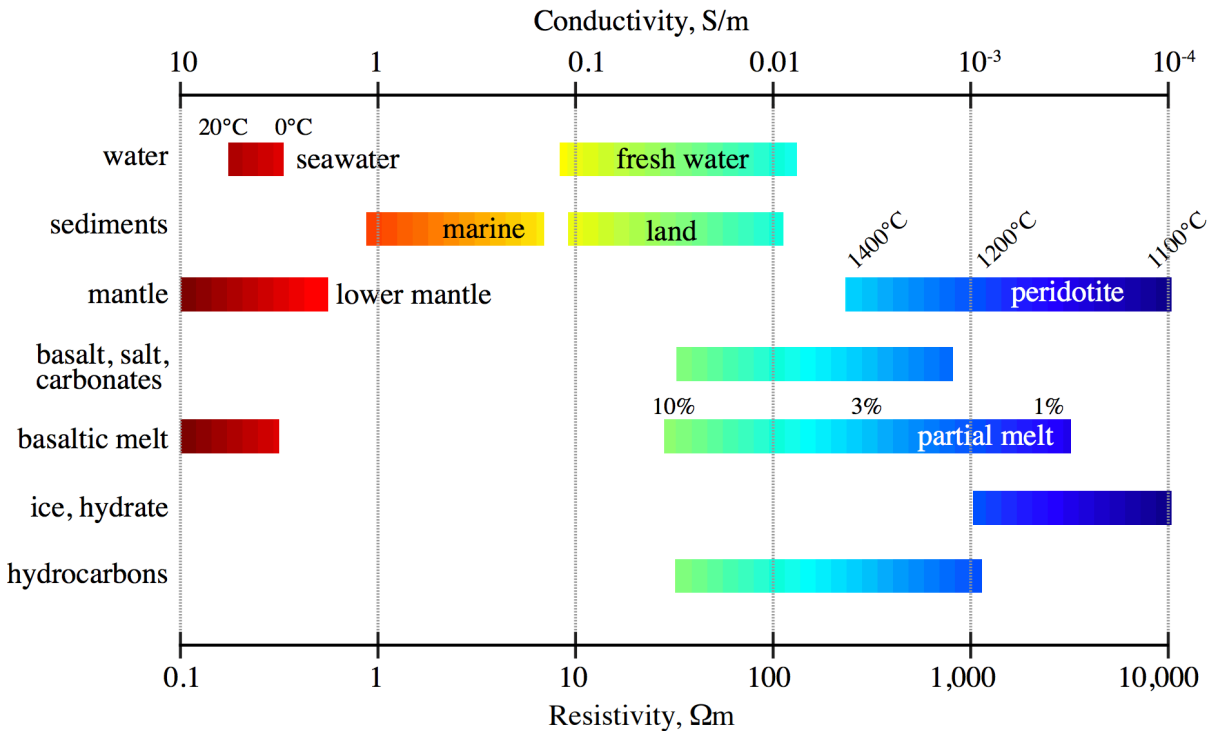
Fig. 2.16: Plot of expected resistivity values for a variety of materials. Image from Constable.

If there are few to no available existing datasets in a survey area, resistivity models are first examined for geologic feasibility. For instance, a reliable resistivity model will have values within the model that lie between ranges that are expected for the survey area as shown in Fig. 2.16 and vertical to horizontal resistivity ratios that are within expected bounds. CSEM data collected in a grid will result in tie-lines and these intersections are inspected for continuity. When available, other datasets are used to 'ground truth', interpret, and/or constrain resistivity models. As an example, Fig. 2.17 is from a study by Gustafson et al. (2019) mapping fresh

submarine groundwater offshore New Jersey. Here, Gustafson et al. (2019) compared datasets, such as borehole and acoustic reflection data, with resistivity models. The datasets are in good agreement and the borehole data was used to interpret the resistive features as trapped slightly saline pore fluids.

Finally, the depth of investigation is examined to limit the depth of interpretation depth of the inversions. The depth of sensitivity and the resolution are tested using rigorous and non-rigorous methods. Chapter 5 explores resolution and depth of a variety of CSEM systems.
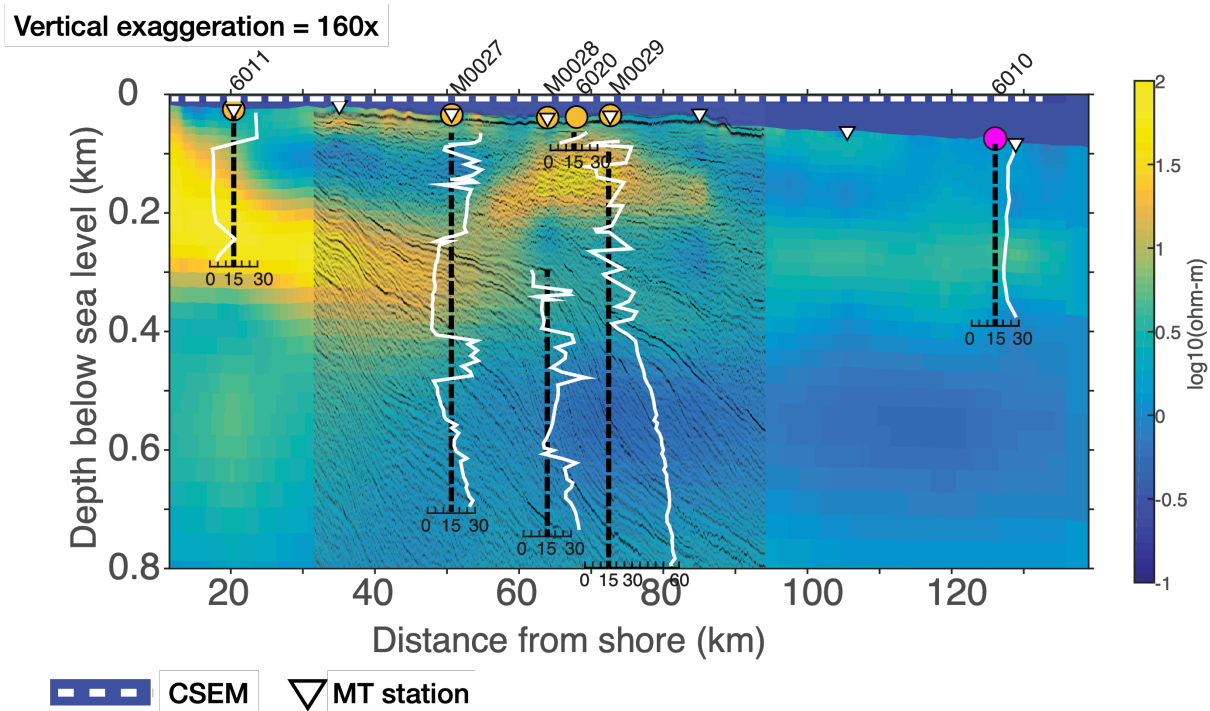


Fig. 2.17: Resistivity profile compared to borehole and seismic reflection data offshore New Jersey from Gustafson et al. (2019). Salinity data is plotted in white over borehole locations where low salinity (left of the dashed line) is collocated with regions of high resistivity (indicating fresh pore fluids) on the resistivity profile. The seismic reflection data, in black, generally maps out the confining unit, or top, of the resistivity (yellow) features in the resistivity profile.

## 2.4 References

Cheesman, S., Law, L., & St Louis, B. (1993). A porosity mapping survey in Hecate Strait using a seafloor electro-magnetic profiling system. In *Marine Geology* (Vol. 10).

Collett, T. S., & Ladd, J. (2000). 19. Detection of gas hydrate with downhole logs and assessment of gas hydrate concentrations (saturations) and gas volumes on the Blake Ridge with electrical resistivity log data 1. In C. K. Paull, R. Matsumoto, P. J. Wallace, & W. P. Dillon (Eds.), *Proceedings of the Ocean Drilling Program, Scientific Results* (Vol. 164).

Constable, S. (2010). Ten years of marine CSEM for hydrocarbon exploration. *Geophysics*, *75*(5). https://doi.org/10.1190/1.3483451

Constable, S. (2013). Review paper: Instrumentation for marine magnetotelluric and controlled source electromagnetic sounding. *Geophysical Prospecting*, *61*(SUPPL.1), 505–532. https://doi.org/10.1111/j.1365-2478.2012.01117.x

Constable, S. (2015). Geomagnetic Induction Studies. In *Treatise on Geophysics: Second Edition* (Vol. 5, pp. 219–254). Elsevier Inc. https://doi.org/10.1016/B978-0-444-53802-4.00101-9
Constable, S. C. (1990). Marine electromagnetic induction studies. *Surveys in Geophysics*, *11*(2), 303–327.

Constable, S. C., Parker, R. L., & Constable, C. G. (1987). Occam's inversion: A practical algorithm for generating smooth models from electromagnetic sounding data. *GEOPHYSICS*, *52*(3), 289–300.

Constable, S., Kannberg, P. K., & Weitemeyer, K. (2016). Vulcan: A deep-towed CSEM receiver. *Geochemistry, Geophysics, Geosystems*, *17*(3), 1042–1064. https://doi.org/10.1002/2015GC006174

Constable, S., Key, K., & Lewis, L. (2009). Mapping offshore sedimentary structure using electromagnetic methods and terrain effects in marine magnetotelluric data. *Geophysical Journal International*, *176*(2), 431–442. https://doi.org/10.1111/j.1365-246X.2008.03975.x

Constable, S., Orange, A., & Key, K. (2015). And the geophysicist replied: "Which model do you want?" *GEOPHYSICS*, *80*(3), E197–E212. https://doi.org/10.1190/geo2014-0381.1

Cook, A. E., Anderson, B. I., Malinverno, A., Mrozewski, S., & Goldberg, D. S. (2010). Electrical anisotropy due to gas hydrate-filled fractures. *Geophysics*, *75*(6). https://doi.org/10.1190/1.3506530

Cox, C. S. (1981). On the electrical conductivity of the oceanic lithosphere. *Physics of the Earth and Planetary Interiors*, *25*, 196–201.

Cox, C. S., Constable, S. C., Chave, A. D., & Webb, S. C. (1986). Controlled-source electromagnetic sounding of the oceanic lithosphere. *Nature*, *320*(6), 52–54.

Edwards, R. N. (1997). On the resource evaluation of marine gas hydrate deposits using sea-floor transient electric dipole-dipole methods. *Geophysics*, *62*(1), 63–74. https://doi.org/10.1190/1.1444146

Eidesmo, T., Ellingsrud, S., Macgregor, L. M., Constable, S., Sinha, M. C., Johansen, S., Kong, F. N., & Westerdahl, H. (2002). *Sea Bed Logging (SBL), a new method for remote and direct identification of hydrocarbon filled layers in deepwater areas*.

Ellingsrud, S., Eidesmo, T., Johansen, S., Sinha, M. C., MacGregor, L. M., & Constable, S. (2002). Remote sensing of hydrocarbon layers by seabed logging (SBL): Results from a cruise offshore Angola. *Leading Edge (Tulsa, OK)*, *21*(10), 972–982. https://doi.org/10.1190/1.1518433
Ellis, M., Evans, R. L., Hutchinson, D., Hart, P., Gardner, J., & Hagen, R. (2008).

Electromagnetic surveying of seafloor mounds in the northern Gulf of Mexico. *Marine and Petroleum Geology*, *25*(9), 960–968. https://doi.org/10.1016/j.marpetgeo.2007.12.006

Evans, R. L. (2001). Measuring the shallow porosity structure of sediments on the continental shelf: A comparison of an electromagnetic approach with cores and acoustic backscatter. *Journal of Geophysical Research*, *106*(C11), 27047–27060.

Evans, R. L. (2007). Using CSEM techniques to map the shallow section of seafloor: From the coastline to the edges of the continental slope. *Geophysics*, *72*(2). https://doi.org/10.1190/1.2434798

Evans, R. L., Law, L., St Louis, B., Cheesman, S., & Sananikone, K. (1999). The shallow porosity structure of the Eel shelf, northern California: results of a towed electromagnetic survey. In *Marine Geology* (Vol. 154).

Evans, R. L., Sinha, M. C., Constable, S. C., & Unsworth, M. J. (1994). On the electrical nature of the axial melt zone at 13°N on the East Pacific Rise. *Journal of Geophysical Research*, *99*(B1), 577–588. https://doi.org/10.1029/93JB02577

Flosadóttir, Á. H., & Constable, S. (1996). Marine controlled-source electromagnetic sounding: 1. Modeling and experimental design. *Journal of Geophysical Research: Solid Earth*, *101*(B3), 5507–5517. https://doi.org/10.1029/95jb03739

Goto, T. N., Kasaya, T., MacHiyama, H., Takagi, R., Matsumoto, R., Okuda, Y., Satoh, M., Watanabe, T., Seama, N., Mikada, H., Sanada, Y., & Kinoshita, M. (2008). A marine deep-towed DC resistivity survey in a methane hydrate area, Japan Sea. *Exploration Geophysics*, *39*(1), 52–59. https://doi.org/10.1071/EG08003

Gustafson, C., Key, K., & Evans, R. L. (2019). Aquifer systems extending far offshore on the U.S. Atlantic margin. *Scientific Reports*, *9*(1). https://doi.org/10.1038/s41598-019-44611-7

Harinarayana, T., Hardage, B., & Orange, A. (2012). Controlled-source marine electromagnetic 2-D modeling gas hydrate studies. *Marine Geophysical Research*, *33*(3), 239–250. https://doi.org/10.1007/s11001-012-9159-z

Hesthammer, J., & Boulaenko, M. (2005). The offshore EM challenge. *First Break*, *23*(11). Kannberg, P. K., & Constable, S. (2020a). Characterization and Quantification of Gas Hydrates in the California Borderlands. *Geophysical Research Letters*, *47*(6), no. https://doi.org/10.1029/2019GL084703

Kannberg, P. K., & Constable, S. (2020b). Characterization and Quantification of Gas Hydrates in the California Borderlands. *Geophysical Research Letters*, *47*(6), no. https://doi.org/10.1029/2019GL084703

Key, K. (2012). Marine Electromagnetic Studies of Seafloor Resources and Tectonics. In *Surveys in Geophysics* (Vol. 33, Issue 1, pp. 135–167). https://doi.org/10.1007/s10712-011-9139-x

Key, K. (2016). MARE2DEM: A 2-D inversion code for controlled-source electromagnetic and magnetotelluric data. *Geophysical Journal International*, *207*(1), 571–588. https://doi.org/10.1093/gji/ggw290

Key, K. (2022, April 20). *MARE2DEM: Modeling with Adaptively Refined Elements for 2D Electromagnetics*. https://mare2dem.bitbucket.io/about.html

King, R. B., Constable, S., & Maloney, J. M. (2022). A case study in controlled source electromagnetism: Near seabed hydrocarbon seep systems of Coal Oil Point, California, USA. *Marine and Petroleum Geology*, *139*. https://doi.org/10.1016/j.marpetgeo.2022.105636

MacGregor, L. M., Constable, S., & Sinha, M. C. (1998). The RAMESSES experiment-III. Controlled-source electromagnetic sounding of the Reykjanes Ridge at 57°45'N. *Geophysical Journal International*, *135*(3), 773–789. https://doi.org/10.1046/j.1365-246X.1998.00705.x

MacGregor, L., Sinha, M., & Constable, S. (2001). Electrical resistivity structure of the Valu Fa Ridge, Lau Basin, from marine Controlled-Source electromagnetic sounding. *Geophysical Journal International*, *146*(1), 217–236. https://doi.org/10.1046/j.1365-246X.2001.00440.x

Myer, D., Constable, S., & Key, K. (2011). Broad-band waveforms and robust processing for marine CSEM surveys. *Geophysical Journal International*, *184*(2), 689–698. https://doi.org/10.1111/j.1365-246X.2010.04887.x

Myer, D., Constable, S., Key, K., Glinsky, M. E., & Liu, G. (2012). Marine CSEM of the Scarborough gas field, Part 1: Experimental design and data uncertainty. *Geophysics*, *77*(4). https://doi.org/10.1190/geo2011-0380.1

Schwalenberg, K., Haeckel, M., Poort, J., & Jegen, M. (2010). Evaluation of gas hydrate deposits in an active seep area using marine controlled source electromagnetics: Results from Opouawe Bank, Hikurangi Margin, New Zealand. *Marine Geology*, *272*(1–4), 79–88. https://doi.org/10.1016/j.margeo.2009.07.006

Schwalenberg, K., Willoughby, E., Mir, R., & Edwards, R. N. (2005). Marine gas hydrate electromagnetic signatures in Cascadia and their correlation with seismic blank zones. *First Break*, *23*(4).

Sherman, D. E. (2018). *Surface-towed controlled source electromagnetic system for mapping extent of subsea permafrost on the Beaufort shelf, Alaska* [PhD thesis]. University of California, San Diego.

Sherman, D., Kannberg, P., & Constable, S. (2017). Surface towed electromagnetic system for mapping of subsea Arctic permafrost. *Earth and Planetary Science Letters*, *460*, 97–104. https://doi.org/10.1016/j.epsl.2016.12.002

Shipley, T. H. (1979). Seismic evidence for widespread possible gas hydrate horizons on continental slopes and rises. *AAPG Bulletin*, *63*(12), 2204–2213.

Sinha, M. C., Constable, S. C., Peirce, C., White, A., Heinson, G., MacGregor, L. M., & Navin, D. A. (1998). Magmatic processes at slow spreading ridges: Implications of the RAMESSES experiment at 57°45'N on the Mid-Atlantic Ridge. *Geophysical Journal International*, *135*(3), 731–745. https://doi.org/10.1046/j.1365-246X.1998.00704.x

Srnka, L. J., Carazzone, J. J., Ephron, M. S., & Eriksen, E. A. (2006). Remote reservoir resistivity mapping. *The Leading Edge*, *25*(8), 972-975.

Wang, S., Constable, S., Reyes-Ortega, V., & Rychert, C. A. (2019). A newly distinguished marine magnetotelluric coast effect sensitive to the lithosphere-Asthenosphere boundary. *Geophysical Journal International*, *218*(2), 978–987. https://doi.org/10.1093/gji/ggz202

Weitemeyer, K. A., Constable, S. C., Key, K. W., & Behrens, J. P. (2006). First results from a marine controlled-source electromagnetic survey to detect gas hydrates offshore Oregon. *Geophysical Research Letters*, *33*(3). https://doi.org/10.1029/2005GL024896

Weitemeyer, K., & Constable, S. (2010). Mapping shallow geology and gas hydrate with marine CSEM surveys. *First Break*, *28*(6).

Yuan, J., & Edwards, R. N. (2000). The assessment of marine gas hydrates through electrical remote sounding: Hydrate without a BSR ? *Geophysical Research Letters*, *27*(16), 2397–2400. https://doi.org/10.1029/2000GL011585

Zach, J. J., & Brauti, K. (2009). Methane hydrates in controlled-source electromagnetic surveys – analysis of a recent data example. *Geophysical Prospecting*, *57*(4), 601–614.

# CHAPTER 3

# Identification of fresh submarine groundwater off the coast of San Diego, USA, using electromagnetic methods

Co-authors: Wesley R. Danskin, Steven Constable, and Jillian M. Maloney

## 3.1 Abstract

Climate change has a pronounced effect on water resources in many semiarid climates, causing populated areas such as San Diego County (USA), to become more vulnerable to water shortages in the coming decades. To prepare for decreased water supply, San Diego County is adopting policies to decrease water use and to develop additional local sources of water. One new local source of freshwater is produced by a desalination facility that purifies brackish groundwater from the coastal San Diego Formation. This formation has been studied extensively onshore, but little is known about the geology or groundwater quality offshore in the adjacent continental shelf. Because most groundwater systems are interconnected and complex, further analysis is needed to identify offshore geology, possible sequestration of freshwater in the shelf, and potential pathways for saltwater intrusion. This comprehensive understanding is important

because seawater intrusion may limit use of the San Diego Formation and longevity of desalination facilities. Controlled-source electromagnetic methods are uniquely suited to detecting offshore groundwater as they are sensitive to changes in pore fluids such as the transition from fresh to brackish groundwater. This paper describes results from surface-towed electromagnetic surveys that mapped the pore-fluid salinity and possible fluid pathways in the continental shelf off the coast of San Diego. The results indicate a considerable volume of fresh-to-brackish groundwater sequestered in the shelf, both in continuous lenses and isolated pockets, that appear influenced by fault systems and shallow stratigraphy.

## 3.2 Introduction

Climate change significantly impacts the water resources available in semiarid climates and populations living within these regions are likely to become more vulnerable to water shortages. The southwestern United States is a semiarid region hosting several large population centers, including coastal southern California with the three highest population density counties in the state (Los Angeles, Orange, and San Diego). This region is dependent upon water from snowpack in northern California which is expected to experience a 48–65% loss by the end of this century and the Colorado River which is expected to see an additional 20% drop in flow by 2050 (Udall and Overpeck 2017). San Diego County is especially vulnerable to these predicted water disruptions as the county currently purchases 85–90% of its water from northern California and the Colorado River.

So that water supply agencies can adapt to the changing climate in semiarid regions, groundwater resources could be further developed to account for an expected decrease in over-all water supplies. In coastal semiarid areas such as San Diego County, development of

groundwater resources is complicated by saltwater intrusion and the potential presence of fresh groundwater reservoirs offshore. Groundwater in the San Diego region is further complicated by its location along the North American-Pacific Plate boundary where several strike- slip fault systems influence coastal geomorphology and sub- surface geology.

The San Diego Formation (SDF) is a heavily faulted coast- al aquifer that is currently supplying about 5% of the total water used in the San Diego area. The salinity of water extracted from the SDF generally ranges between slightly-saline to brackish (1,500–2,500 ppm), with some regions producing freshwater (defined as less than 500 ppm). The combination of increasing water demand and diminishing sources of imported water suggests that groundwater extraction from the SDF may increase, in particular to supply municipal water to communities in southwestern San Diego area (San Diego County Water Authority 2021). Groundwater extracted from the SDF could originate from naturally recharged precipitation, or alternatively, from aquifer storage and recovery, a method that involves artificial recharge of the SDF with excess water during periods of low water use followed by extraction of this water during periods of high-water use (Keller and Ward 2001).

To provide water agencies with the scientific under- standing to evaluate these water-management scenarios, the United States Geological Survey (USGS)—in cooperation with the Sweetwater Authority, the City of San Diego, and the Otay Water District—began an extensive hydrogeology project in 2001 to map the geology and the water resources of the San Diego area (US Geological Survey 2020). A major part of this project focused on mapping the San Diego coastal aquifer, determining groundwater recharge and discharge rates, identifying groundwater flowpaths, and assessing groundwater quality. Installation of 16 USGS multiple-depth,

monitoring-well sites enabled collection of three-dimensional (3D) geologic data, ground- water levels, and groundwater quality. The project study area, the generalized geology of the San Diego area, and the locations of USGS monitoring-well sites are shown in Fig. 3.1. Hydrogeologic understanding gained from these sites and from development and testing of geologic and hydrologic models helped to define the onshore coastal geology, groundwater recharge and discharge rates, and groundwater flowpaths.



Fig. 3.1: Map illustrating the USGS San Diego Hydrogeology project study area, which extends offshore of San Diego. Sedimentary deposits are shown in yellow; hard rock is shown in pink; streams and water bodies are shown in blue; USGS monitoring-well sites are indicated by red dots (US Geological Survey 2021)

Data collected from these onshore USGS monitoring sites from 2001 to 2020 indicate that fresh and brackish groundwater flows onshore from the continental shelf under San Diego Bay, driven by onshore groundwater extraction from the SDF (Anders et al. 2013). Additionally, noble gas isotope analyses of sampled well water indicate that groundwater age generally

42

increases with proximity to the coastline (Seltzer et al. 2019). These observations, combined with the geologic model of the San Diego coastal aquifer, suggest that the SDF extends about 5 km west of the present shoreline and indicate that freshwater may have been sequestered in the SDF when the continental shelf was subaerially exposed approximately 20,000 years ago (Danskin 2012). Because most hydrogeologic information has been collected onshore, the location and extent of offshore groundwater are not well understood. Historically, electro- magnetic (EM) surveying has been used on land to map groundwater resources with great success (Knight et al. 2018; McNeill 1988). Also, EM methods have been proposed by many authors to identify salinity of submarine ground- water (Cohen et al. 2010; Haroon et al. 2021; Micallef et al. 2020, 2021; Post et al. 2013) and several controlled-source electromagnetic (CSEM) surveys have been successful at identifying groundwater offshore, most notably offshore Martha's Vineyard (Gustafson et al. 2019) and Hawaii (Attias et al. 2021). The geologic setting of San Diego varies from these previous studies in that the presence of offshore groundwater has not yet been confirmed, and the SDF is heavily faulted, possibly isolating pockets of fresh- water offshore. This current study aims to further the understanding of the onshore groundwater system by characterizing and mapping pore fluids within the offshore part of the SDF using CSEM methods.

## 3.3 The CSEM method

The marine CSEM method uses a human-made source of EM energy that passes through seawater and propagates into the seafloor and to receivers, deployed either on the seafloor or towed through the water, which measure the resulting electric fields. The recorded fields are proportional to electrical resistivity, making the method suitable for detecting fresh groundwater,

which is significantly more resistive in comparison to seawater or the surrounding seafloor

sediment. Additionally, as the porosity and cementation of the SDF are well studied onshore, the

salinity of the submarine aquifer can be predicted with electrical conductivity data by applying

Archie's Law. Using observations and data collected from USGS monitoring-well sites and

hydrogeologic models, the porosity of the SDF is constrained to values between 30–45% with a

mean value of 38% and the cementation exponent used in Archie's Law was determined to be

1.8. Of these two variables, porosity has the greatest effect on the predicted salinity of the pore

fluids. The relationship between salinity and bulk resistivity given these values is shown in Fig.

3.2.
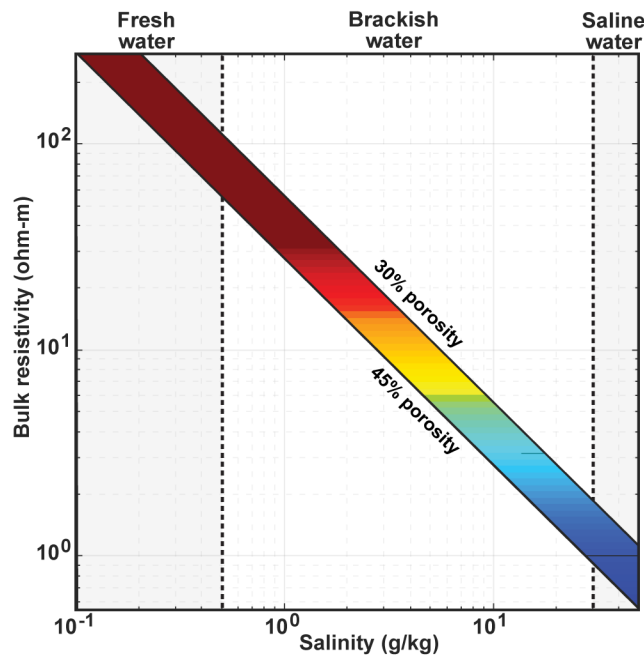


Fig. 3.2: Graph illustrating the predicted changes in bulk resistivity with changing pore fluid salinity using characteristic SDF attributes such as porosity values between 30 and 45%. Pore fluid salinity can be estimated from the resistivity models generated with controlled-source electromagnetic (CSEM) data using Archie's Law which describes the relationship between cementation factor, porosity, bulk resistivity, and pore fluid conductivity of a material

Because the water depths on the continental shelf are shallow and the SDF is not

expected to extend more than 500 m below sea level, the small and low-power surface- towed

CSEM system of Sherman et al. (2017) can be used effectively to map the SDF. This system has the added benefit that it is inexpensive to use, can be hand-deployed, and requires a nonspecialized vessel to efficiently survey the shelf. The system, illustrated in Fig. 3.3, consists of an EM transmitter that generates an electric dipole, four electric field receivers, and a dorsal device that collects water- conductivity and water-depth data. The electric dipole, four receivers (referred to as porpoises), and dorsal are towed on the surface of the water behind a vessel traveling between 2 and 4 knots (approximately 1–2 m/s) on floating high-molecular-weight polyethylene rope. The frames of the receivers and dorsal are made from rigid plastic that is designed to slough off kelp or other ocean debris, hold a rigid dipole 0.67 m beneath the sea surface, and provide mounting for a vertical global positioning system (GPS) mast that doubles as a flashing beacon for better visibility to other vessels. To maximize sensitivity to the predicted geometry of the SDF, the receivers were separated by 100 m, creating a maximum source-receiver spacing of 400 m and a total towed array length of 430 m.
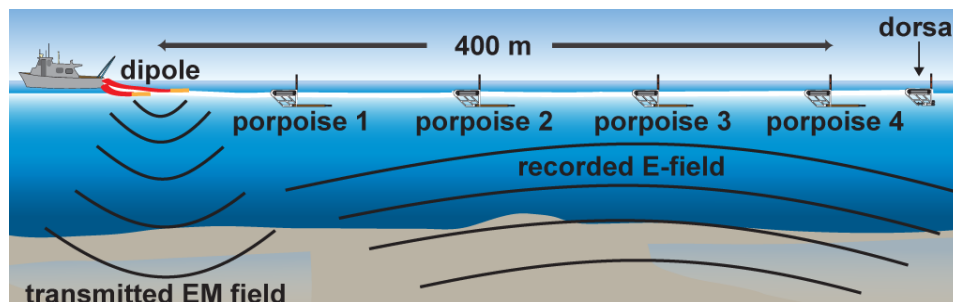


Fig. 3.3: Schematic of the CSEM array used for the survey offshore San Diego County, California. The dipole is a 10-m horizontal electric dipole source. For the surveys discussed here, the dipole center is located 28.2 m from the GPS mast-mounted on the vessel.

The EM transmitter operates on 110–240 VAC power and can output a GPS stabilized binary or ternary waveform of as much as 50 amps on an antenna typically 50 m long. For this survey, the transmitter outputs a 30-amp current-controlled 2.5-Hz fundamental waveform-D,

described by Meyer et al. (2011), on a 10-m antenna. This configuration resulted in a 300-amp-m horizontal electric dipole moment, which is a signal strength well suited to the source-receiver spacing chosen for this survey. Waveform-D was chosen as it generates higher amplitude responses in the 1st, 3rd, 7th, and 13th harmonics than other binary and ternary waveforms, allowing the collection of data across a broad frequency range (Meyer et al. 2011).

## 3.4 Survey data quality

The data presented here were collected from September 2019 to September 2020 on 5 separate days of surveying aboard the Scripps Institution of Oceanography research vessel Bob and Betty Beyster. The cruises were designed to initially survey the shelf with a broad exploration method followed by increasingly focused surveys targeting resistive anomalies identified within the SDF from the initial results. The location of the survey lines presented here are shown in Fig. 3.4.

A total of 141 km of high-quality inline electric field response data were collected. For each day of survey, the data were inspected for quality before further processing. GPS data from the towed receivers were lost on the first day of data collection because of user error; however, redundant onboard GPS data were found to be sufficient and thus used. For the following three survey days, all instruments functioned as designed.
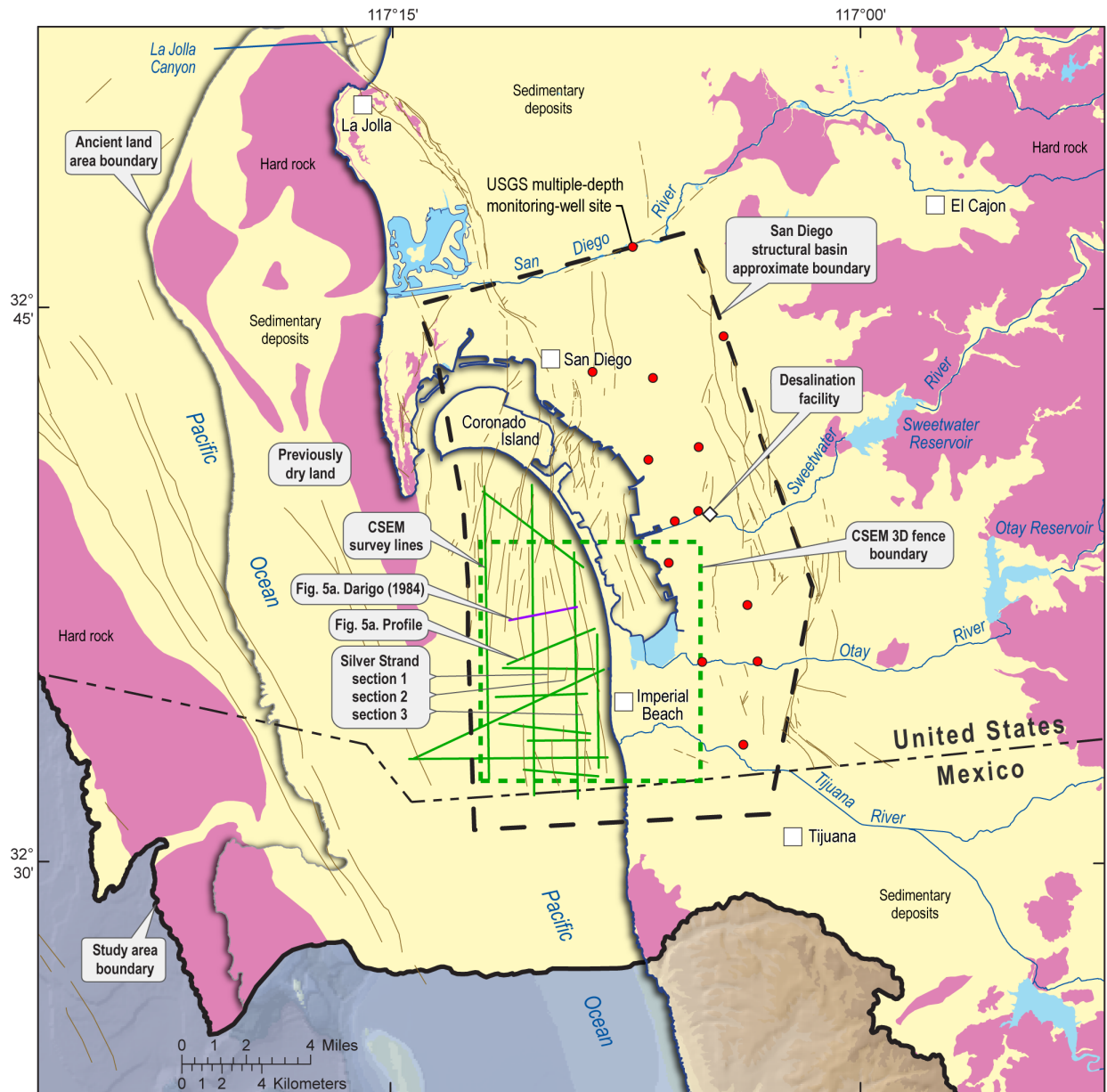
Fig. 3.4: Map of San Diego area with simplified geology. Sedimentary deposits are shown in yellow; hard, mostly crystalline and metamorphic, rock is shown in pink; known and inferred fault locations are shown in black. CSEM survey lines presented here are shown in green. The dashed green box indicates the boundary of Fig. 3.6. The location of the two-dimensional (2D) geologic interpretation from Darigo (1984) used in Fig. 3.5 is shown here in purple. USGS monitoring-well sites are indicated with red dots (US Geological Survey 2021)

## 3.5 Results

Amplitude and phases of the CSEM response functions were extracted from the collected raw time-series data using a method detailed by Meyer et al. (2011). To increase the signal-to-noise ratio, the resulting transfer function estimates were stacked using an arithmetic mean to obtain the transfer function estimates for every 30 s along with an error estimate. This method yielded high quality amplitude and phase response data for all four receivers as a function of position and frequency. Amplitude data for all four receivers at 2.5, 7.5, 13.5, and 32.5 Hz and phase data for 7.5 and 13.5 Hz were included in the inversion code. The amplitude data for these frequencies were well above the noise floor and sensitive to the known depths of the SDF. Phase was neglected at 2.5 Hz as there was little variability in the signal and addition of these data in the models resulted in an unbalanced misfit between frequencies due to the model fitting noise in the 2.5 Hz phase. Phase was also neglected at 32.5 Hz as there was significant impact from clock drift at this frequency.

The modeling software used in this study is the publicly available, goal-oriented, adaptive, finite-element two-dimensional (2D) MARE2DEM inversion and modeling code of Key (2016). This code uses Occam's Inversion, a method that regularizes the inversion to the smoothest resistivity model that fits the data to a specified misfit (Constable et al. 1987). CSEM data were scrutinized manually for obvious outliers and subjected to a 2% error floor before being included in the inversion as finite-length dipoles.

The starting models included the seawater as a fixed parameter, using conductivity data collected by the dorsal and available bathymetric data. Therefore, the free inversion regions were reduced to the area below the seafloor and set to a uniform starting resistivity of 1 $\Omega$m. Inversion

parameter grids were constructed using 30-m-wide quadrilateral cells that increased in height with depth to mimic the loss of resolution of the EM method. Due to the adaptive nature of the MARE2DEM code, the computation mesh was allowed to fine where necessary to produce accurate responses. The resolution depth was investigated by including a highly conductive (0.1 Ωm) or highly resistive (1,000 Ωm) layer as a base to the model at varying depths. From these tests, the limits of sensitivity are estimated to be at a depth between 400 to 500 m below sea level; thus, the final model interpretation and presentation is limited to these depths. Isotropic inversions fit the amplitude data, but these models produced biased phase residuals and a normalized root-mean-square of 1 was not achieved, suggesting the need to include anisotropy in the models (Sherman and Constable 2018). Thus, differing resistivity values in the vertical and horizontal directions were included in the models, and allowed for simultaneous fit of both the amplitude and phase data. These inversions resulted in anisotropic ratio (vertical resistivity/ horizontal resistivity) of up to 5 in the SDF, consistent with the geology of the SDF which has been observed to have a series of fining-upward stratigraphic sequences. The anisotropic resistivity inversions fit the data to a normalized root- mean-square of 1 with a two-percent error floor. See Fig. 3.5a for an example resistivity model and Fig. 3.5b for the data and data fits from this model, which are representative of the data quality and model fit of the surveys and resulting models discussed in this paper. The final resistivity models that focus on the main resistive anomalies offshore Imperial Beach, located in the southern coastal San Diego area, are shown in Fig. 3.6.
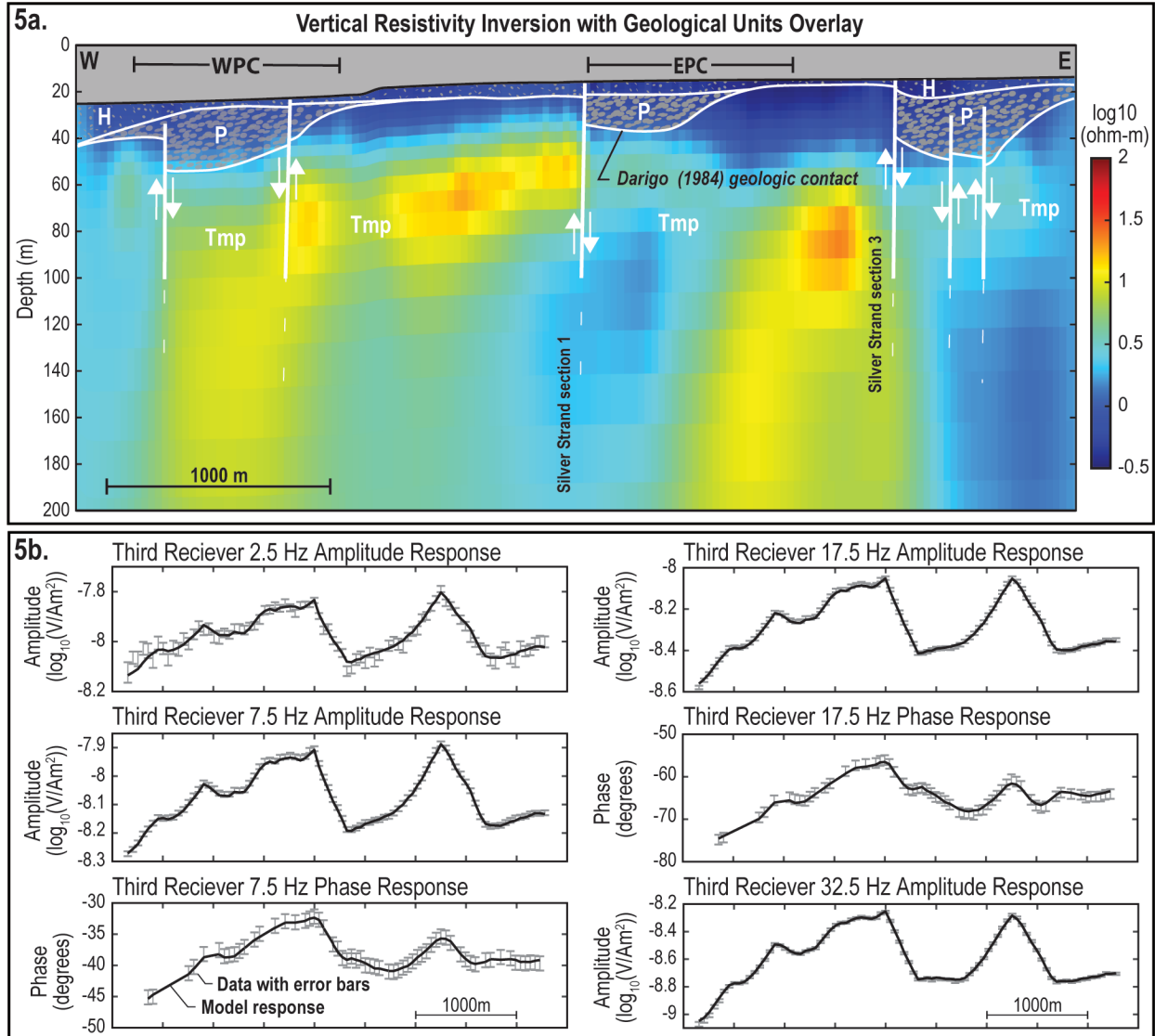
Fig. 3.5: **a** Plot of 2D vertical resistivity model from one line of data, with data and data fits from the third receiver in the array (300-m transmitter to receiver offset). 2D vertical resistivity model with overlain geologic interpretations (marked in white) by Darigo (1984) are shown (a). The location of the vertical resistivity model is shown in Figs. 4 and 6 and the location of the geologic interpretations by Darigo (1984) are shown on Fig. 3.4. The resistivity model is run with an anisotropic penalty weight of 0.05 and is fit to a normalized root mean square of 1. Warm colors (red, yellow) indicate areas where pore fluids are fresh-to-slightly saline (<3,000 ppm total dissolved solids), assuming a porosity value between 30 and 45%. Cool colors (blue) indicate moderately-saline-to-highly-saline pore fluids. The white labels are from Darigo (1984): H Holocene sediment; P Pleistocene channel fill; Tmp undifferentiated Miocene and Pliocene (SDF). Conductive U-shaped features interpreted as paleochannels are labeled EPC (eastern paleochannel) and WPC (west- ern paleochannel). **b** Plots the data and error (error bars) and modeled response (black lines) for all data used in the inversion from the third receiver in the array. The data quality and data fit presented here are representative of both the data quality of the other receivers in the array and the data fit achieved by the other inversion results discussed in this paper.

## 3.6 Discussion

The structural San Diego basin is a pull-apart sedimentary basin which underlies much of the San Diego area and was formed concurrently with deposition of the SDF during the middle-to-late Pliocene to Pleistocene (Kennedy and Peterson 1973. The San Diego basin is observed to increase in depth from north to south, with the SDF also thickening until both the basin and the SDF gradually shallow and flatten near the USA–Mexico border. The SDF also shallows and thins both to the east and west and is interpreted to be thickest beneath the city of Imperial Beach (Huntley et al. 1996). The western edge of the SDF is not well defined, but current hydrogeologic models which incorporate gravity, seismic, and borehole data indicate that the western boundary occurs approximately 5 km west of the present shoreline.

The 2D models of vertical resistivity contain numerous highly resistive anomalies offshore Imperial Beach. The depth to these resistive anomalies is approximately 50–80 m below sea level, which is consistent with the depth at which the SDF is encountered in nearby USGS monitoring-well sites. Additionally, Darigo (1984), using acoustic reflection methods, interpreted the locations of these resistive features to be the SDF (see Fig. 3.5a). As such, the locations of these resistive anomalies are interpreted to be within the SDF. Archie's law, the resistivity models, and known geologic parameters of the SDF were used to predict the salinity of the pore fluids within these resistive anomalies. The resistive anomalies (>10 $\Omega$m) offshore Imperial Beach correspond to areas where pore fluids are fresh-to-slightly saline (<3,000 ppm). Assuming a porosity of 30% and a thickness of 100 m, consistent with model geometries, the volume of the mapped fresh-to-slightly-saline groundwater is approximately 390 million $m^3$ (103 billion gallons). The onshore volume of the SDF is estimated to be between 341 and 532

million m$^3$ (City of San Diego 2016). The estimated offshore volume of groundwater nearly

doubles the total volume of the SDF which is consistent with predictions by Keller and Ward

(2001).
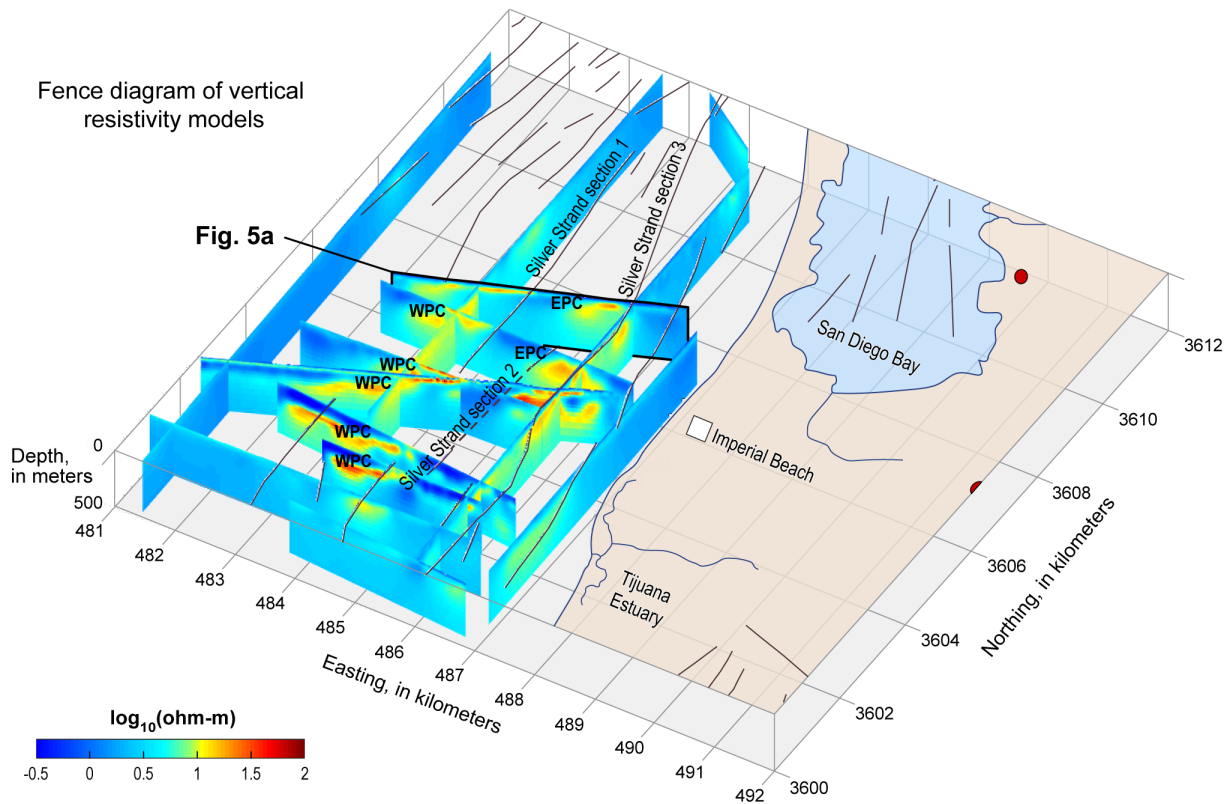


Fig. 3.6: Fence plot of 2D vertical resistivity models offshore Imperial Beach; CSEM survey lines and fence plot extent also are shown in Fig. 3.4. Models are run with an anisotropic penalty weight of 0.05 and are fit to a root mean square of 1. Black lines indicate the surface locations of known faults (USGS Interactive Fault Database 2019); thin blue lines indicate the present-day shoreline. Red dots onshore indicate locations of USGS monitoring-well sites (US Geological Survey 2021). Warm colors (red, yellow) indicate areas where pore fluids are fresh-to-slightly saline (<3,000 ppm total dissolved solids), assuming a porosity value between 30 and 45%. Cool colors (blue) indicate moderately-saline-to- highly-saline pore fluids. Conductive U-shaped features interpreted as paleochannels are labeled EPC (eastern paleochannel) and WPC (western paleochannel).

The resistive anomalies appear to be north-south trending and are separated by down-

dropped blocks controlled by segments of the Silver Strand fault zone. In previous seismic

surveys, the down-dropped blocks have been observed to be collocated with Pleistocene and Quaternary paleochannels that were incised into the continental shelf during the last glacial maximum, a time when the continental shelf was sub- aerially exposed (Darigo 1984; Graves et al. 2021). Similar west (W) and east (E) paleochannels (PC) were found in this CSEM survey and are indicated by conductive U-shaped features labeled respectively as WPC and EPC on Figs. 5a and 6.

The paleochannels marked EPC are collocated with areas in which the SDF appears to be conductive, signifying saline pore fluids. This observation indicates, in these areas, that the paleochannels may have been incised into the lower- permeability sediment that functionally trapped the fresh SDF pore fluids, allowing for fluid migration into and out of the SDF. As sea level rose, drowning the shelf, these incisions would allow for diffusion of saltwater into the SDF below the paleochannels. Saline pore fluids appear to have infilled the SDF below the paleochannels marked EPC. Conversely, the paleochannels marked WPC, which run parallel and west of Silver Stand section 1, also appear to have been incised into the SDF, but the resistive anomalies remain intact below these paleochannels. This preservation of fresh-to-slightly-saline pore fluids within the SDF, despite the presence of overlying paleochannels, may result from locational differences in the SDF stratigraphy.

Depositionally, the SDF is a mixture of shallow marine and nonmarine sediment (Keller and Ward 2001). As a result, the SDF contains multiple fining-upward sequences, sandy marls, conglomerates, and clayey layers (Ellis 1919) which is evident in the anisotropic ratios generated from the final resistivity models. The fining-upward sequences and clayey layers may form a series of less permeable sediment, which could aid in preserving freshwater in the more

permeable layers below. This vertical restriction to groundwater flow is illustrated in the confined response observed during regional-scale, multiple-well aquifer tests and single-well pumping tests (Brandt et al. 2020). The depositional character of the SDF may be one reason that the fresh-to-slightly-saline pore fluids are preserved below the paleochannels marked WPC, west of Silver Strand section 1. In these areas, the fining-upward sequences may form a series of caps to pore fluids within the SDF. The WPC paleochannels may have been incised into some, but not all, of these caps, which could leave parts of the SDF undisturbed.

An additional reason for irregularities in the highly resistive locations could be the discontinuous nature of the more permeable parts of the SDF, which are separated by clayey sediment (Huntley et al. 1996). This depositional pattern may explain the discontinuous nature of the resistors offshore, but it does not explain the boundaries being collocated with fault traces. Therefore, geometries and lo- cations of the highly resistive features mapped via CSEM may result from a combination of stratigraphy, regional faulting, and lithification.

Finally, the Silver Strand fault zone is made up of a series of strike-slip, right-lateral faults within a generally transtensional regime (Maloney et al. 2016). These faults transect the offshore SDF, creating migration pathways for freshwater flushing. This phenomenon, in the form of freshwater springs along the fault zone, has been noted in historical records of Coronado Island (Keller and Ward 2001). The 2D resistivity models suggest upward fluid migration from the lower fresh-to-slightly-saline anomalies along the Silver Stand fault sections 1 and 3. These anomalies extend in some cases to the seafloor. The vertical orientation of, depth to the tops of, and collocation with known faults of these resistive features suggest the presence of freshwater flushing along Silver Stand fault sections 1 and 3.

## 3.7 Conclusion

The use of CSEM offshore San Diego, California, USA, has resulted in a resistivity model identifying sections of the SDF with substantial volumes of fresh-to-slightly- saline pore fluids, sequestered offshore. These results also indicate that CSEM could be a useful and efficient tool for mapping the extent of other coastal aquifers across diverse geologic settings. The results, however, also illustrate the potential complications related to withdrawing water from the naturally charged SDF or using the SDF for aquifer storage and recovery. Possible freshwater flushing from these sections has been interpreted along the transtensional faults related to the Silver Strand fault zone. In this case, offshore faulting may act as conduits for saltwater intrusion into the onshore SDF. Conversely, offshore faulting may act as partial barriers to groundwater flow and inhibit movement of fresh or saline ground- water into the onshore SDF. Further research and data collection are needed to understand how well this off-shore, submarine groundwater is connected hydraulically to the onshore SDF.

## 3.8 Acknowledgements

This chapter, in full, is a reformatted reprint of the material published in: King, R. B., Danskin, W. R., Constable, S., & Maloney, J. M. (2022). Identification of fresh submarine groundwater off the coast of San Diego, USA, using electromagnetic methods. *Hydrogeology Journal*, *30*(3), 965-973. The dissertation author was the primary investigator and author of this paper.

## 3.9 References

Anders R, Mendez GO, Futa K, Danskin WR (2013) A geochemical approach to determine sources and movement of saline groundwater in a coastal aquifer. Ground Water 52:756–768. https://doi.org/10. 1111/gwat.12108

Attias E, Constable S, Sherman D, Ismail K, Shuler C, Dulai H (2021) Marine electromagnetic imaging and volumetric estimation of fresh- water plumes offshore Hawaiʻi. Geophys Res Lett 48(7): e2020GL091249

Brandt JT, Sneed M, Danskin WR (2020) Detection and measurement of land subsidence and uplift using interferometric synthetic aperture radar, San Diego, California, USA, 2016–2018. Proc IAHS 382:45– 49. https://doi.org/10.5194/piahs-382-45-2020

City of San Diego (2016) 2015 San Diego Urban Water Management Plan. City of San Diego. https://www.sandiego.gov/sites/default/ files/2015_uwmp_report.pdf. Accessed February 2022

Cohen D, Person M, Wang P, Gable CW, Hutchinson D, Marksamer A, Dugan B, Kooi H, Groen K, Lizarralde D, Evans RL, Day-Lewis FD, Lane JW Jr (2010) Origin and extent of fresh paleowaters on the Atlantic continental shelf, USA. Groundwater 48(1):143–158

Constable SC, Parker RL, Constable CG (1987) Occam's inversion: a practical algorithm for generating smooth models from electromagnetic sounding data. Geophysics 52(3):289–300

Danskin WR (2012) Gaining the necessary geologic, hydrologic, and geochemical understanding for additional brackish groundwater development, coastal San Diego, California, USA. Extended abstract. 22nd Salt Water Intrusion Meeting, Buzios, Brazil, June 2012

Darigo NJ (1984) Quaternary stratigraphy and sedimentation of the main- land shelf of San Diego County, California. PhD Thesis, University of Southern California, Los Angeles

Ellis AJ (1919) Geology and ground waters of the western part of San Diego County, California. Nos. 444–446, US Government Printing Office, Washington, DC

Graves LG, Driscoll NW, Maloney JM (2021) Tectonic and eustatic control on channel formation, erosion, and deposition along a strike-slip margin, San Diego, California, USA. Cont Shelf Res 231:104571

Gustafson C, Key K, Evans RL (2019) Aquifer systems extending far offshore on the US Atlantic margin. Sci Rep 9(1):1–10

Haroon A, Micallef A, Jegen M, Schwalenberg K, Karstens J, Berndt C, Garcia X, Kuehn M, Rizzo E, Fusi NC, Ahaneku CV, Petronio L, Faghih Z, Weymer BA, Biase MD, Chidichimo F (2021) Electrical resistivity anomalies offshore a carbonate coastline: evidence for freshened groundwater? Geophys Res Lett 48(14):e2020GL091909

Huntley D, Biehler S, Marshall CM (1996) Distribution and hydrogeologic properties of the San Diego Formation, southwestern San Diego County. San Diego Formation Task Force, Report of Investigation 2005-1032. Cal Groundw Bull 118

Keller B, Ward A (2001) Tectonic setting of the San Diego formation aquifer, considered for conjunctive use storage. J S Am Earth Sci 14(5):533–540

Kennedy MP, Peterson GL (1973) Geology of the San Diego metropolitan area, California, vol 200. California Division of Mines and Geology, Sacramento, CA

Key K (2016) MARE2DEM: a 2-D inversion code for controlled-source electromagnetic and magnetotelluric data. Geophys J Int 207(1): 571–588

Knight R, Smith R, Asch T, Abraham J, Cannia J, Viezzoli A, Fogg G (2018) Mapping aquifer systems with airborne electromagnetics in the Central Valley of California. Groundwater 56(6):893–908

Maloney JM, Driscoll N, Kent G, Duke S, Freeman T, Bormann J, Anderson R, Ferriz H (2016) Segmentation and step-overs along strike-slip fault systems in the inner California borderlands: implications for fault architecture and basin formation. Appl Geol Cal 26:655–677

McNeill JD (1988) Advances in electromagnetic methods for groundwater studies. In: 1st EEGS symposium on the application of geophysics to engineering and environmental problems. cp-214-00003, European Association of Geoscientists and Engineers, Houten, The Netherlands

Meyer D, Constable S, Key K (2011) Broad-band waveforms and robust processing for marine CSEM surveys. Geophys J Int 184(2):689– 698. https://doi.org/10.1111/j.1365-246X.2010.04887.x

Micallef A, Person M, Berndt C, Bertoni C, Cohen D, Dugan B, Evans R, Haroon A, Hensen C, Jegen M, Key K, Kooi H, Liebetrau V, Lofi J, Mailoux BJ, Martin-Nagle R, Michael HA, Muller T, Schmidt M et al (2021) Offshore freshened groundwater in continental margins. Rev Geophys 59(1):e2020RG000706

Micallef A, Person M, Haroon A, Weymer BA, Jegen M, Schwalenberg K, Faghih Z, Duan S, Cohen D, Mountjoy JJ, Woelz S, Gable CW, Averes T, Tiwari AK (2020) 3D characterization and quantification of an offshore freshened groundwater system in the Canterbury Bight. Nat Commun 11(1):1–15

Post VE, Groen J, Kooi H, Person M, Ge S, Edmunds WM (2013) Offshore fresh groundwater reserves as a global phenomenon. Nature 504(7478):71–78

San Diego County Water Authority (2021) 2020 Urban water management plan. San Diego County Water Authority, San Diego

Seltzer AM, Ng J, Danskin WR, Kulongoski JT, Gannon RS, Stute M, Severinghaus JP (2019) Deglacial water-table decline in southern California recorded by noble gas isotopes. Nat Commun 10(1):1–6

Sherman D, Constable SC (2018) Permafrost extent on the Alaskan Beaufort shelf from surface-towed controlled-source electromagnetic surveys. J Geophys Res: Solid Earth 123(9):7253–7265

Sherman D, Kannberg P, Constable S (2017) Surface towed electromagnetic system for mapping of subsea Arctic permafrost. Earth Planet Sci Lett 460:97–104

US Geological Survey (2020) San Diego hydrogeology. https://ca.water. usgs.gov/sandiego/. Accessed December 2021

US Geological Survey (2020–2021) USGS water data for USA. National Water Information System: Web Interface. https://doi.org/10.5066/ F7P55KJN. Accessed May 10, 2021

US Geological Survey and California Geological Survey (2019) Quaternary fault and fold database of the United States. https:// www.usgs.gov/natural-hazards/earthquake-hazards/faults. Accessed April 10, 2019

Udall B, Overpeck J (2017) The twenty-first century Colorado River hot drought and implications for the future. Water Resour Res 53(3): 2404–2418

# CHAPTER 4

# A case study in controlled source electromagnetism: Near seabed hydrocarbon seep systems of Coal Oil Point, California, USA

Co-authors: Steven Constable and Jillian M. Maloney

## 4.1 Abstract

Marine hydrocarbon seeps are found on all continental margins and release significant amounts of greenhouse gases and hydrocarbons into the atmosphere and hydrosphere. Most methods of studying seeps rely on seafloor or near-seafloor observations, but seepage rates and seep locations can be variable, leading to uncertainty. We exploit the fact that hydrocarbons are electrically resistive compared with surrounding sediments and use marine electromagnetic methods to study the deeper sources and accumulation sites, which are controlled by local geology and should be more stable than the seabed expressions. Our surface towed marine controlled source electromagnetic system used a horizontal electric dipole transmitter and floating electric dipole receivers spaced 100–400 m from the transmitter, collecting frequency domain amplitude and phase data at ~2 Hz and harmonics. The survey targeted known and

inferred hydrocarbon seeps within the Coal Oil Point seep field offshore Santa Barbara, California, USA. Two dimensional inversions of the data indicate that the method is sensitive to the shallowly buried (<400 m) structure of the marine hydrocarbon seeps and is an efficient and effective tool in their identification and characterization. The results show spatial variability of seafloor hydrocarbons along the Coal Oil Point seep field and indicate at least two previously unidentified intermediate depth accumulation sites. The depth and lateral extent of these hydrocarbon accumulation sites may improve seep emission models for the Coal Oil Point seep field.

## 4.2 Introduction

Marine hydrocarbon seeps (MHS) are pervasive across almost all continental margins and are an important part of the global carbon budget. Recent estimates indicate that these seeps account for up to a fifth of all global geological methane emissions (Etiope, 2009; Etiope et al., 2019). However, estimates of the total emissions from MHS have significant uncertainties as seeps can be irregularly active and the hydrocarbon migration pathways and shallow (<400 m) or near seabed accumulation of hydrocarbons are under-studied (Leifer, 2019). Many previously successful methods used to identify and estimate emission rates of MHS rely on the seep being active at the time of surveying. These methods have included side scan sonar, multibeam bathymetry, seismic profiling systems, gas capture systems, airborne spectroscopy, remote operated vehicles, and many others (e.g., Hornafius et al., 1999; Mitchell et al., 2018; Razaz et al., 2020; Leifer et al., 2006). Although these methods are useful for identifying seepage rates at the time of surveying, it has been noted in numerous studies that seep rates and seep areal extent can vary on subhourly, semidiurnal, diurnal, seasonal, and even on decadal scales (Leifer and

Boles, 2005b; Fischer, 1975). Therefore, more information of the migration pathways and surrounding structures of MHS systems will aid in the understanding of overall seep activity.

A new method was developed to image hydrocarbon accumulation and migration related to MHS fields within the surrounding geology to a depth of 400 m below sea level. As hydrocarbons are significantly more electrically resistive than sediment, MHS systems are well-suited to detection by marine controlled-source electromagnetic (CSEM) methods (Constable, 2010; Constable and Srnka, 2007 & Orange et al., 2009). For the surveys presented here, a newly developed surface-towed CSEM system was deployed. This system is inexpensive and easy to use in a coastal setting (Sherman et al., 2017).

## 4.3 Study Area

The Coal Oil Point (COP) MHS field is located offshore Isla Vista in Santa Barbara County, California, in water depths from a few meters to 80 m (Fig. 4.1) and has two primary trends. The trend closer to the shoreline is in a few meters water depth and is associated with the folded and fractured source rock outcropping and seeping at the seabed. The offshore trend is in water depths of 50–100 m and is generally controlled by the South Ellwood Anticline. In this paper, the study area and the term COP are limited to the offshore seep area associated with the South Ellwood Anticline (see Fig. 4.1 for extent). Due to the prolific nature of this field and proximity to dense coastal populations, this area has been subject to numerous field investigations that have identified many seeps, geochemical markers, and the geologic structure underlying the region (e.g., Leifer, 2019; Lorenson et al., 2009; Hornafius et al., 1999; Kamerling et al., 2003). The stratigraphy of the COP seep field is folded, creating a series of structural traps for hydrocarbon accumulation within and above the source rock (Eichhubl et al.,

2000). The source rock is capped by the relatively impermeable Sisquoc Formation and the traps

are fed by fractures, faults, or through updip migration along bedding planes (Fig. 4.2)

(Finkbeiner et al., 1997; Ogle et al., 1987).
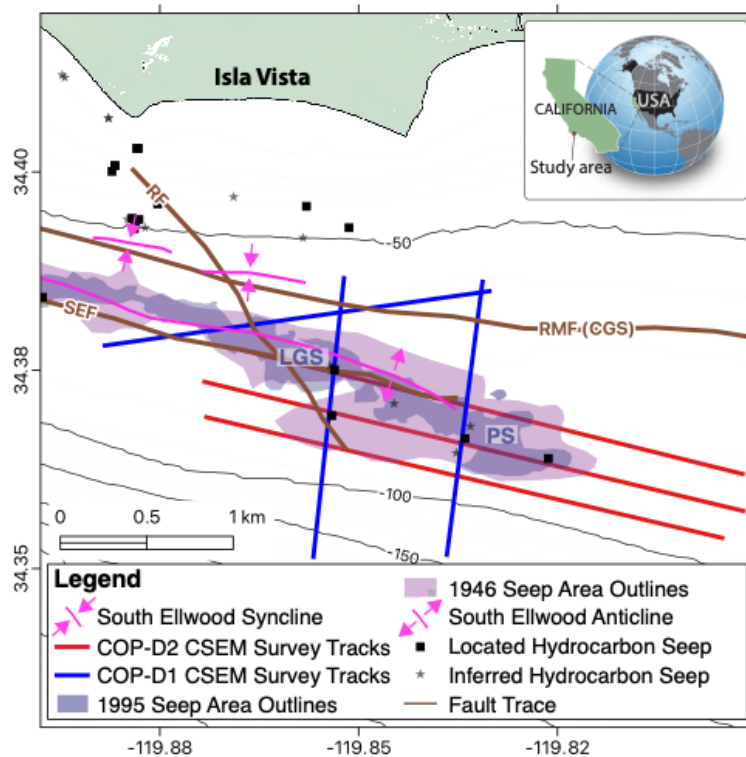


Fig. 4.1: Coal Oil Point seep field area offshore Isla Vista located within Santa Barbara County, California. COP-D1 CSEM Survey tracks (red lines) represent locations of data collected in January 2019. COP-D2 CSEM Survey tracks (blue lines) represent locations of data collected in May 2021. Survey track lines were chosen based on proximity to seep area outlined from 1995 seep gas spatial distributions by Hornafius et al. (1996) and inferred and located seep locations identified and defined by the USGS (Lorenson et al., 2009). The seep area outlined from 1946 gas and oil distributions is by Fischer (1978). La Goleta seep field is labeled LGS and Patch Seep is labeled PS (all seep names are informal). Finally, South Ellwood Anticline, South Ellwood Syncline, and fault locations from Leifer et al., (2010) and California Geological Survey are plotted: RF - Rudder Fault, RMF (CGS) - Red Mountain Fault trace by California Geological Survey (Treiman, 2006), SEF – South Ellwood Fault. Water depth contours are marked in black.

Within the COP seep field, there are two main seep areas located along the South

Ellwood anticline. The La Goleta MHS field is located near the shallowest crest of the Monterey

Formation below the COP seep field and Patch Seep is located toward the eastern end of the

COP seep field (Fig. 4.1). Based on the local geology, the accumulation site of the La Goleta MHS field and the Patch Seep should be located at least 1 km below sea level and controlled by the South Ellwood Anticline and South Ellwood Fault System (Leifer et al., 2010). La Goleta MHS field has displayed variable emission trends and hydraulic conductivity between different seeps (Bradley et al., 2010; Leifer, 2019) and delays have been observed between deep reservoir pressure changes and seepage rates (Leifer, 2019). These observations indicate that individual seeps may be connected at depth above the source rock. However, the locations of possible shared migration pathways or accumulation sites are not well defined.

The seep model for the COP MHS field described by Leifer and Boles (2005a) assumes a deep hydrocarbon reservoir plus an additional near-seabed reservoir to account for seepage behavior at La Goleta MHS field and Patch Seep. According to the model, seepage rates are pressure-sensitive and related to changes in hydrostatic pressure from tidal forcing and pressures from deep reservoirs. The balance of over- pressure and reservoir pressure result in changing emission rates at the seep sites (Leifer and Boles, 2005a; Leifer and Wilson, 2007). Generally, the effect of hydrostatic pressure decreases with seabed depth (Boles et al., 2001). Leifer and Boles (2005b) predicted the lower bounds of tidal influencing through changing hydrostatic pressure in the COP region to be in water depths of 100–200 m. The flow of oil and gas from seep systems also is controlled by reservoir pressure, which increases with depth (Leifer and Wilson, 2007). The relationship between these two pressures is significantly impacted by the depth of the reservoir and the surrounding geology.

This marine CSEM study aimed to test the seep model of Leifer and Wilson (2007) by mapping the location of the hydrocarbon accumulation beneath La Goleta MHS field and Patch

Seep. These fields are attractive targets to test for the existence of near-seabed hydrocarbon accumulation as upward hydrocarbon migration is controlled by the many local faults and the anticlinal structure could provide many potential intermediate traps for accumulation below the field.
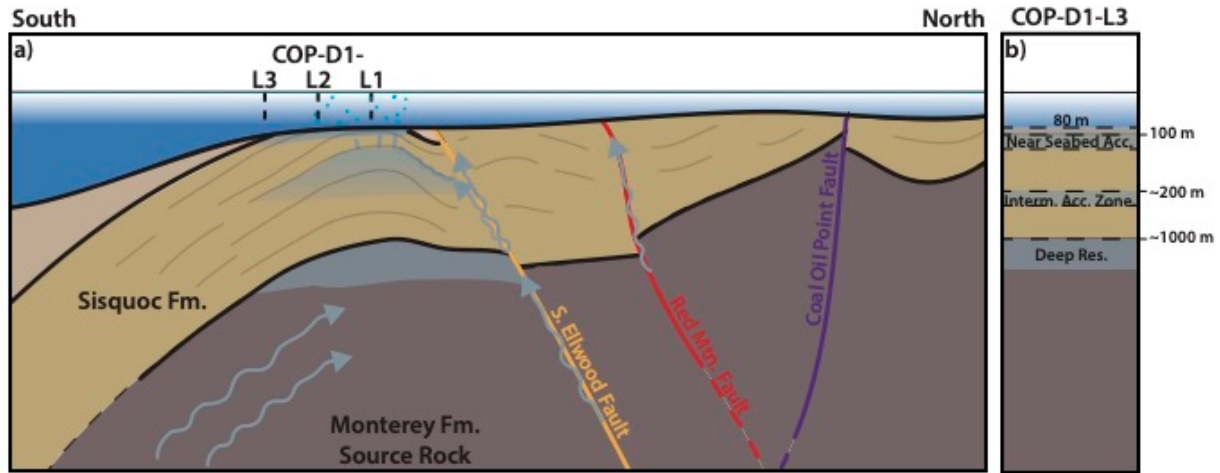


Fig. 4.2: a) Cartoon demonstrating potential fluid migration pathways (light blue arrows) upward from lower Monterey Formation (source rock) to intermediate near- seabed accumulation sites below the survey area. Illustration based on geologic models by Leifer et al., (2010). Note: illustration is not to scale. Dashed black lines indicate the intersection points of 2D resistivity profiles associated with the 2019 EM survey. b) illustrates hydrocarbon accumulation sites imaged in EM line COP-D1_L3 as well as a deep reservoir from previous studies (Leifer et al., 2010; Tennyson and Kropp, 1998).

## 4.4 Methodology

### 4.4.1 CSEM survey design

The marine CSEM method uses an electric current transmitter that emits electromagnetic fields that pass through seawater and propagate into the seafloor and to receivers, which measure the resulting electric fields, either on the seafloor or towed through the water. The recorded fields are proportional to electrical resistivity, making the method suitable for detecting hydrocarbons

which are significantly more resistive in comparison to seawater or the surrounding seafloor sediment (e. g., Constable, 2010).

Because the water depths of La Goleta MHS field and Patch Seep are shallow, the custom-built small, low power, surface-towed CSEM system of Sherman et al. (2017) can be used effectively to map hydrocarbon occurrences to depths of 400 m below sea level. This system has the added benefit that it is inexpensive to use, can be hand-deployed, and requires a non-specialized vessel to efficiently survey the shelf. The system, illustrated in Fig. 4.3, consists of an electromagnetic transmitter, four electric field receivers, and a dorsal device that collects water-conductivity and water-depth data. The horizontal electric dipole, four receivers (referred to as porpoises), and dorsal are towed on the surface of the water on floating high molecular weight polyethylene rope, behind a vessel traveling between 2 and 4 knots. The frames of the receivers and dorsal are made from rigid plastic that is designed to slough off kelp or other ocean debris, to hold a rigid 2 m dipole 0.67 m beneath the sea surface, and to provide mounting for a vertical GPS mast that provides position and timing, and doubles as a flashing beacon for better visibility to other vessels. To maximize sensitivity to the predicted geology related to La Goleta MHS field, the receivers were separated by 100 m creating a maximum source-receiver spacing of 400 m and a total towed array length of 430 m. From sensitivity tests, the limits of sensitivity using this array are estimated to be at a depth between 400 and 500 m below sea level. Horizontal resolution is roughly 5–10% of the receiver to target distance; for example, if the investigation depth is 100 m below sea level, this array could yield horizontal resolution of 5–10 m at this depth.
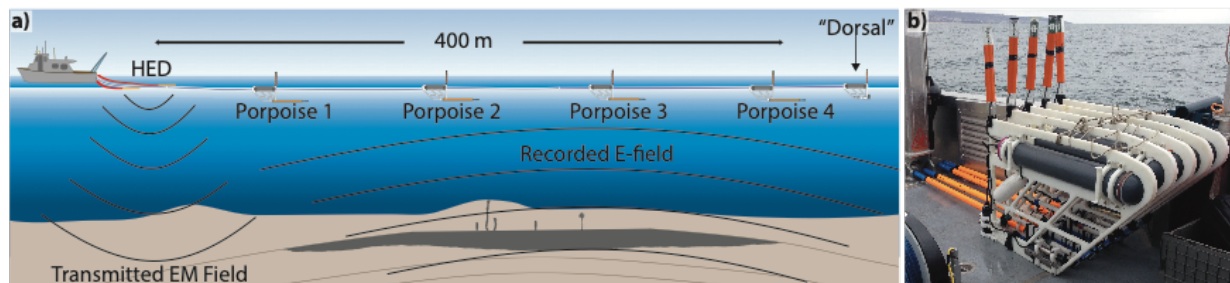
Fig. 4.3: a) Schematic of CSEM array used for survey offshore Isla Vista, Santa Barbara County, California. Horizontal electric dipole is labeled here as 'HED'. Here, the emitted electromagnetic field from the HED is labeled 'Transmitted EM Field'. b) Photo of all four porpoises (receivers) and dorsal (front) staged on deck. Logger is a grey pressurized case held in place with a white frame. GPS masts are orange vertical instruments affixed to the back of each white frame. The receiver frames have blue weights at the base to keep the instruments upright during towing operations.

The electromagnetic transmitter operates on 110–240 VAC power and outputs a GPS stabilized binary or ternary waveform. For this survey, the transmitter output was a 30-amp, current-controlled waveform- D of Meyer et al. (2011) on a 10-meter antenna. This configuration resulted in a 300 amp-meter horizontal electric dipole moment, a signal strength well suited to the source-receiver spacing chosen for this survey. Waveform-D was chosen as it generates higher amplitude responses in the 1st, 3rd, 7th, and 13th harmonics than other waveforms, allowing for collection of data across a broad frequency range (Meyer et al., 2011). The data presented here were collected during two separate cruises in January of 2019 and May of 2021. The survey design remained the same for both surveys except for the fundamental frequency of the waveform. A 2 Hz fundamental waveform was used to collect the initial 2019 CSEM data; following analysis of the data, the fundamental frequency was increased to 2.5 Hz for surveying in 2021 to increase the frequencies of the higher harmonics.

### 4.4.2 Survey data quality

A total of 37 km of high-quality inline electric field responses were collected in 350 min over the course of two survey days, one for each survey year (see Fig. 4.1 for survey locations). Following both surveys, the data were inspected for quality before processing. In January of 2019 (shown in red on Fig. 4.1), surveying from the FV Amigo, the last receiver in the array did not function because it reset, probably because of an impact that occurred during transportation, and the GPS mast of the first receiver in the array did not transmit data due to problems with a pin connection. In May of 2021 (shown in blue on Fig. 4.1), surveying from the RV Bob and Betty Beyster, the first receiver in the array malfunctioned due to a faulty battery. The rest of the receiver systems in both surveys functioned as designed.

### 4.4.3 Data processing and model design

Amplitude and phases of the CSEM response functions were extracted from the raw time-series data using a method detailed by Meyer et al. (2011). To increase the signal-to-noise ratio, the resulting transfer function estimates were stacked using an arithmetic mean to obtain the complex transfer function estimates for every stacking window along with an error estimate. Due to rough wave conditions (3 plus meter wave heights and 7 m/s wind gusts) in January 2019, stacking windows of 30 s were used. Sea state was calm in May of 2021 allowing for smaller stacking windows of 10 s to achieve similar errors to the previous survey in 2019. This method yielded high quality amplitude and phase response data for two receivers and three receivers as a function of position and frequency for the 2019 and 2020 surveys respectfully, although the first harmonic was excluded due to low signal to noise of the responses. The CSEM

data associated with the 3rd, 7th, and 13th harmonics were well above the noise floor, making them suitable for inversion.

The modeling software used in this study is the publicly available, goal-oriented, adaptive, finite-element two-dimensional (2D) MARE2DEM inversion and modeling code of Key (2016). This code uses Occam's Inversion, a method that regularizes the inversion to obtain the smoothest resistivity model that fits the data (Constable et al., 1987). CSEM data were scrutinized manually for obvious outliers and subjected to a two-percent error floor for amplitude data and a one-percent error floor for phase data before being included in the model as finite-length dipoles. The 10 m-long horizontal electric dipole (HED) was modeled as a finite-length electric bipole and assumed to have a dip of 10°, consistent with direct observations during the survey.

The starting models included seawater as a fixed parameter, using conductivity data collected by the dorsal and available bathymetric data. Thus, the free inversion regions were reduced to the area below the seafloor and set to a uniform starting resistivity of 1 $\Omega$m. Inversion parameter grids were constructed using quadrilateral cells that increased in height with depth to mimic the loss of resolution of the EM method with distance. Due to the adaptive nature of the MARE2DEM code, the computation grid was allowed to refine where necessary to accurately predict the model's data response (this is sometimes called the dual grid approach). The resistivity inversions were run to the minimum root mean square misfit possible; this value was then increased by ten percent to avoid overfitting and the final resistivity inversions converged to a root-mean-square misfit between 1 and 1.1, and are shown in Fig. 4.4.
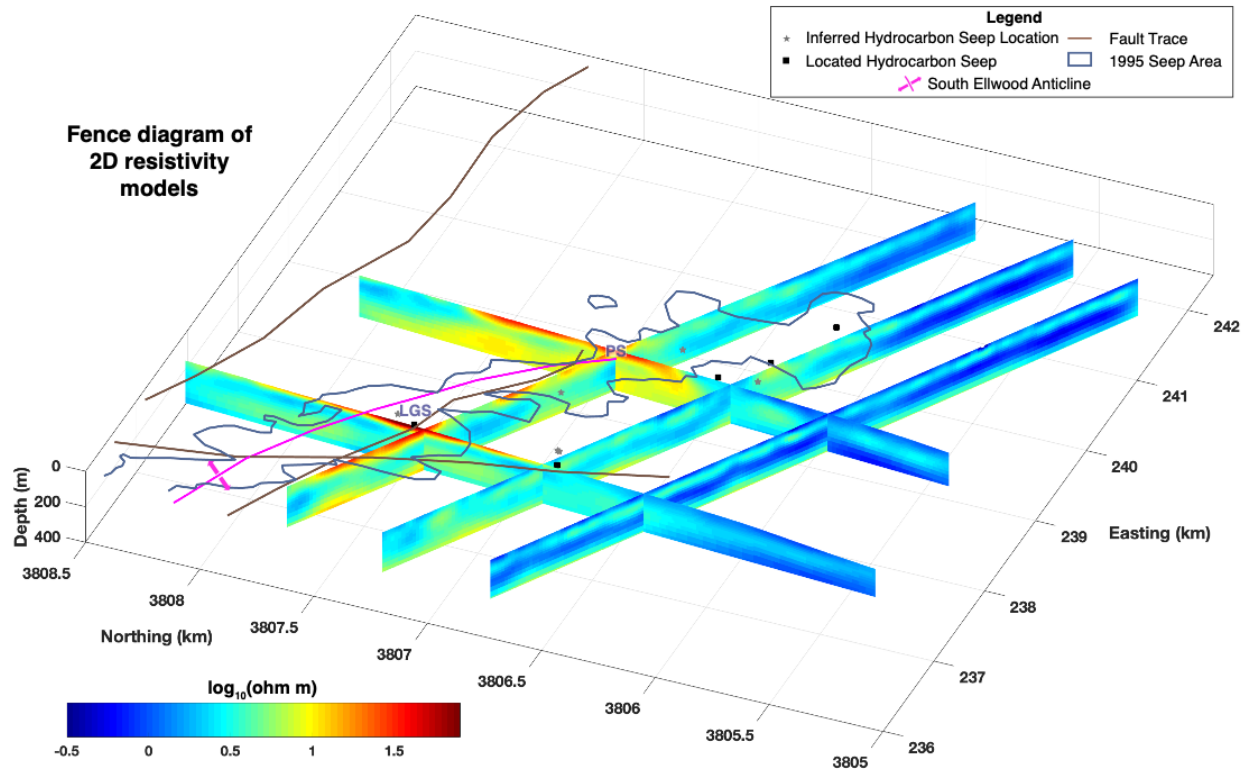
Fig. 18.4: Fence plot of 2D resistivity models over La Goleta MHS field (labeled here as 'LGS') and Patch Seep (labeled here as 'PS'); CSEM survey lines and dates of collection are also shown in Fig. 4.1. Dark blue lines indicate areal extent of seep gas distributions from Hornafius et al. (1996). Black squares indicate located seeps, and grey stars indicate the inferred location of seeps identified and defined by the USGS (Lorenson et al., 2009). Brown lines indicate the surface locations of the Rudder Fault, South Ellwood Fault (Leifer et al., 2010), and Red Mountain Fault (Treiman, 2006). Warm colors indicate high resistivity, inferred to be hydrocarbons. Coordinates in fence plot are UTM – Zone 11.

## 4.5 Results and discussion

Below La Goleta MHS field and PS, the South Ellwood Anticline locally creates a trap in the fractured reservoir approximately 1 km below sea level (Fig. 4.2) (Leifer et al., 2010; Tennyson and Kropp, 1998). This reservoir is supplied by updip and near vertical hydrocarbon migration along thick damage zones (<20 m) associated with the South Ellwood Fault System (Leifer et al., 2010) from the deeper source rock (Kamerling et al., 2003). Further upward migration to shallow traps or to the seafloor is facilitated by the South Ellwood Fault System,

69

Rudder Fault, other unmapped faults in the Monterey Formation, and open fractures and joints within the Sisquoc Formation.

The 2D resistivity models presented here contain several resistive anomalies below La Goleta MHS field, Patch Seep, and several unnamed seep sites (Fig. 4.4). The resistive anomalies collocated with known and inferred seep sites have resistivity values consistent with those expected from hydrocarbons (Constable, 2010), and so resistors encountered in this survey are interpreted to be hydrocarbons. Prior studies, based on water column and seafloor observations, have indicated that the areal extent of La Goleta MHS field is consistent and controlled by the South Ellwood Anticline and damage zones associated with the Rudder Fault (Washburn et al., 2005; Hornafius et al., 1999;Leifer et al., 2005a; Leifer, 2019). Conversely, the spatial extent of the Patch Seep has been observed to change based on water column sampling studies; for example, the northern edge of the seep field has been recorded to shift up to ~600 m depending on the time of surveying (Fig. 4.1). The seafloor resistivity values modeled here are in agreement with these observations (Fig. 4.5). Previous maps of the La Goleta MHS field are collocated with high seafloor resistivity and vertical resistors below the seep field (Figs. 4, Fig. 4.5, and Fig. 4.6) (Hornafius et al., 1996; Fischer, 1978; Lorenson et al., 2009). These resistive features are collocated with the Rudder Fault, indicating hydrocarbon migration along related damage zones. Possibly due to changes in spatial extent of the Patch Seep, the highest seafloor resistivities near the Patch Seep are north of the area most recently mapped as an active seep site, although they are within previously mapped seep extents (Figs. 1 and 4). Additionally, a vertical resistor is imaged below Patch Seep which may be a hydrocarbon migration pathway within open fractures related to anticlinal flexure from the South Ellwood anticline (labeled in Fig. 4.6). There are several plausible reasons for the mismatch in seafloor resistivity and the most recent

70

Patch Seep locations, most notably the presence of oily bubbles that can lead to oil deposition

within the seep vents and bacterial or tar mats which can obstruct seepage, resulting in vent

evolution or movement (Leifer, 2010).
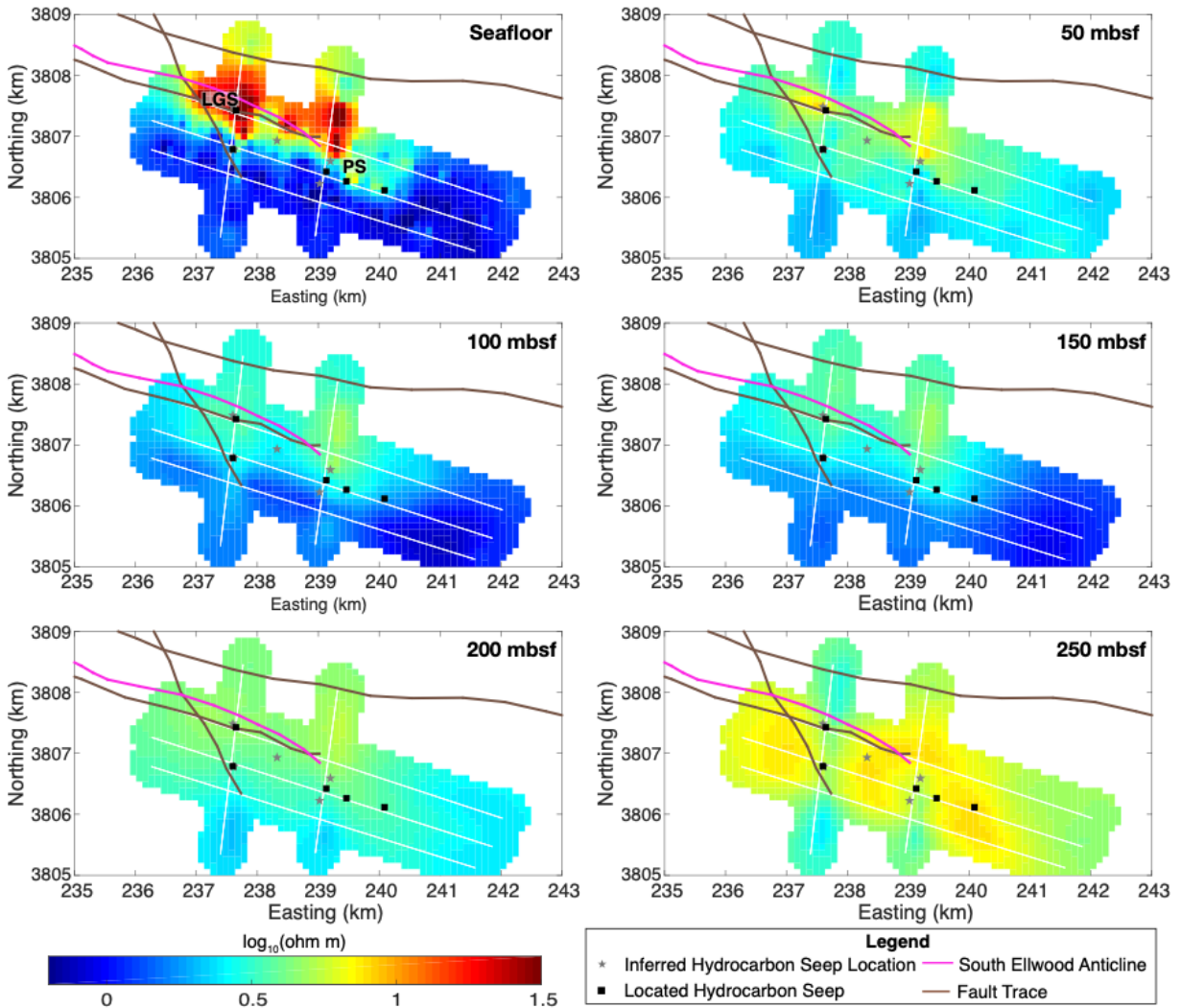


Fig. 4.5: Maps of logarithmic resistivity at and below the seafloor. Peak resistivity appears to correspond to the South Ellwood Anticline and is collocated with La Goleta MHS field, but is not collocated with Patch Seep. Peak resistivity is encountered both at the seafloor and again at approximately 250 m below seafloor (mbsf). The geometry of the seafloor and 250 mbsf resistor generally trend with the South Ellwood Anticline.

Below the MHS presented here, a resistor approximately 25 m below the seafloor (mbsf)

is pervasive across all survey lines (Fig. 4.4 and labeled 'near seabed reservoir' in Fig. 4.6).

According to geologic models and seismic reflection profiles, this resistive layer is located within the Sisquoc Formation (Leifer et al., 2010; Kamerling et al., 2003; Sliter et al., 2008) and the feature could be produced from horizontal migration of hydrocarbons within a coarse layer of this formation (Fig. 4.2) (Boles et al., 2001; Boetius and Suess, 2004; Chen et al., 2021). This interpretation is supported by chip analysis from onshore and offshore wells that indicate local sandstone layers within the Sisquoc Formation (MacKinnon, 1989) and that the resistive layer appears to be constrained by the mapped anticline and synclines with several vertical features extending to known MHS locations. A trapping mechanism such as pore throat blockage or a change in permeability may lead to this near seafloor build-up of hydrocarbons. As this accumulation site is shallowly buried (~150 m total depth), changes in hydrostatic pressure through tidal forces may have a more pronounced effect on the associated MHS fields when compared to MHS fields supplied by deeper reservoirs.

Finally, a deeper resistor is encountered at approximately 200–250 mbsf within the Sisquoc Formation (Fig. 4.5 and labeled 'intermediate reservoir' in Fig. 4.6). This resistor appears to be constrained by the South Ellwood Anticline and has multiple vertical resistors connecting it to the seafloor seep locations (Fig. 4.6). Due to these observations, this resistor is interpreted as a hydrocarbon accumulation site that supplies the MHS fields above and the vertical features are interpreted to be migration pathways facilitated by open fractures related to the Rudder Fault or anticlinal flexure from the South Ellwood Anticline (Ogle et al., 1987). This accumulation zone is shallower than the previously identified hydrocarbon reservoirs located approximately 1000 m below La Goleta MHS Field. Therefore, the resistor located 200 to 250 mbsf could be an intermediate reservoir; a feature most recently proposed by Leifer (2019) to accurately model the temporal variability of seepage observed within COP. Before this CSEM

survey, the existence of intermediate reservoirs beneath COP were inferred, but the depth and

extent were not known.
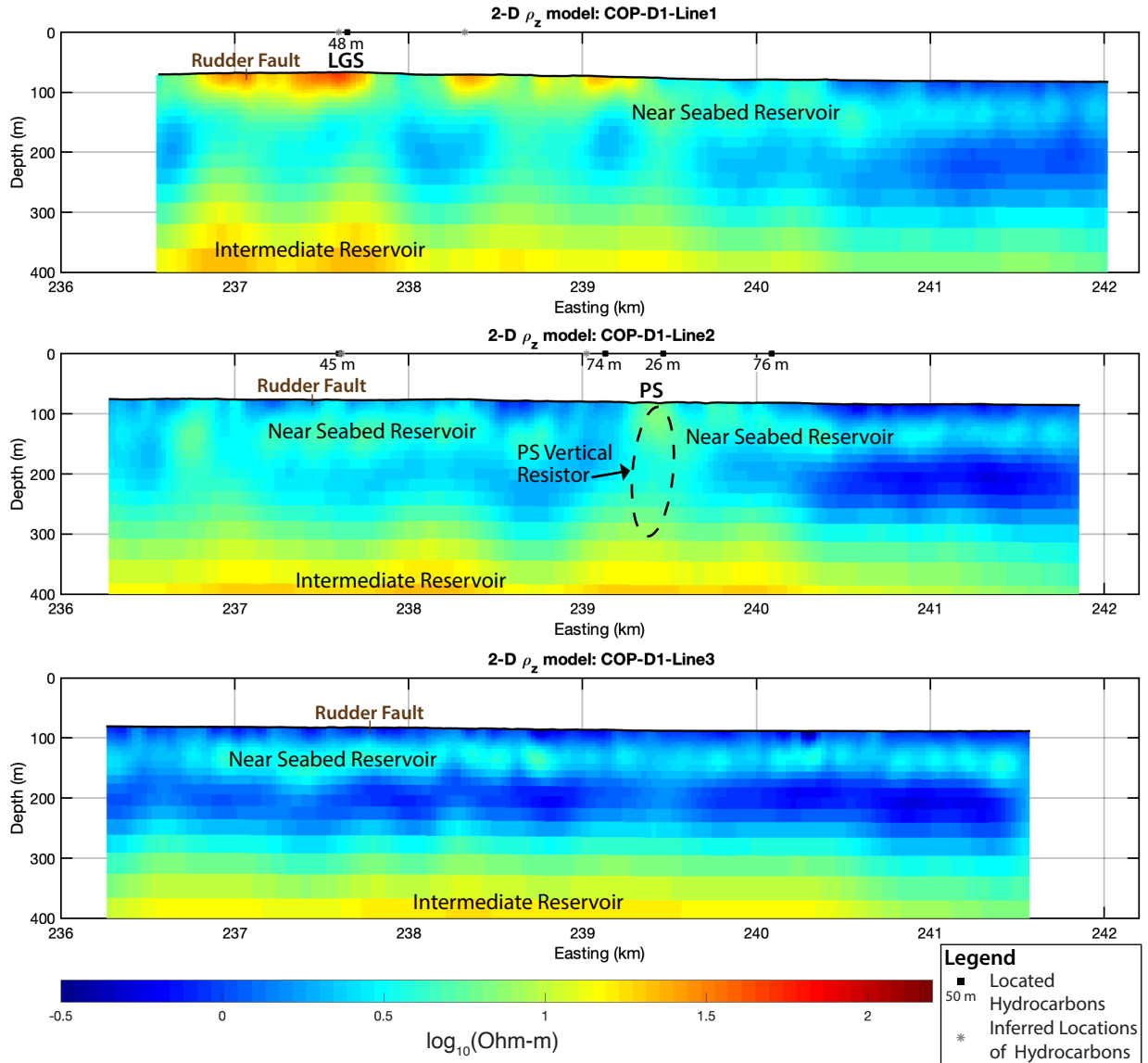


Fig. 4.6: 2D Resistivity Models of COP- D1 Lines 1 through 3 plotted with approximate locations of major seepage associated with La Goleta MHS Field (LGS) and Patch Seep (PD). Also plotted are locations of known and inferred seep locations as identified and defined by the USGS (Lorenson et al., 2009) with crossline distances to known hydrocarbon seep locations indicated. See Fig. 4.1 for plan view of model locations. The surface trace of the Rudder Fault is plotted in brown. Here, depth refers to meter below sea-level.

## 4.6 Conclusion

The surface towed CSEM method used in this survey has been shown to be both efficient and effective at detecting marine hydrocarbon seep systems to total depths of 400 m. Our system detected two previously unidentified near seabed hydrocarbon accumulation sites which may supply the overlying MHS fields. The existence of one accumulation site is assumed in the model of Leifer (2019); however, the depth and lateral extent has not been characterized until now. The addition of this new knowledge in seep models could better constrain overall seep emission rates. Additionally, the 2D resistivity models indicate significant changes in extent and movement of the Patch Seep at the seafloor while the underlying MHS sources remain controlled by the South Ellwood Anticline. These results highlight the variability in the seafloor location of seeps and importance of studying the buried hydrocarbon accumulation sites and migration pathways to gain further insights into MHS character. More information is needed to characterize and predict the seep behavior in this region; however, CSEM methods could be useful in the identification of other hydrocarbon seep systems, as they can survey large regions relatively quickly and are sensitive to these targets.

## 4.7 Acknowledgements

This chapter, in full, is a reformatted reprint of the material published in: King, R. B., Constable, S., & Maloney, J. M. (2022). A case study in controlled source electromagnetism: Near seabed hydrocarbon seep systems of Coal Oil Point, California, USA. Marine and Petroleum Geology, 139, 105636.

## 4.8 References

Boetius, A., Suess, E., 2004. Hydrate Ridge: a natural laboratory for the study of microbial life fueled by methane from near-surface gas hydrates. Chem. Geol. 205, 291–310.

Boles, J.R., Clark, J.F., Leifer, I., Washburn, L., 2001. Temporal variation in natural methane seep rate due to tides, Coal Oil Point area, California. J. Geophys. Res.: Oceans 106 (C11), 27077–27086.

Bradley, E., Leifer, I., Roberts, D., 2010. Long-term monitoring of a marine geologic hydrocarbon source by a coastal air pollution station in Southern California. Atmos. Environ. 44 (38), 4973–4981.

Chen, C., Zheng, Z., Zeng, L.F., Xiao, F., Tian, L.P., Huang, K.Y., 2021. A combined geophysical and lithological study on eruptive history and Quaternary lacustrine stratigraphy of a maar in Leizhou Peninsula, China. J. Palaeogeogr. 10 (1), 1–14.

Constable, S., 2010. Ten years of marine CSEM for hydrocarbon exploration. Geophysics 75 (5), 75A67–75A81.

Constable, S.C., Parker, R.L., Constable, C.G., 1987. Occam's inversion: a practical algorithm for generating smooth models from electromagnetic sounding data. Geophysics 52 (3), 289–300.

Constable, S., Srnka, L.J., 2007. An introduction to marine controlled-source electromagnetic methods for hydrocarbon exploration. Geophysics 72 (2), WA3–WA12.

Eichhubl, P., Greene, H.G., Naehr, T., Maher, N., 2000. Structural control of fluid flow: offshore fluid seepage in the Santa Barbara Basin, California. J. Geochem. Explor. 69, 545–549. https://doi.org/10.1016/S0375-6742(00)00107-2.

Etiope, G., 2009. Natural emissions of methane from geological seepage in Europe. Atmos. Environ. 43 (7), 1430–1443.

Etiope, G., Schwietzke, S., Helmig, D., Palmer, P., 2019. Global geological methane emissions: an update of top-down and bottom-up estimates. Elementa: Science of the Anthropocene 7.

Finkbeiner, T., Barton, C.A., Zoback, M.D., 1997. Relationships among in-situ stress, fractures and faults, and fluid flow: Monterey Formation, Santa Maria Basin, California. AAPG Bull. 81 (12), 1975–1999.

Fischer, P.J., 1975. Natural Gas and Oil Seeps, Santa Barbara Basin. California State University, Department of Geosciences, California.

Fischer, P.J., 1978. Oil and tar seeps, Santa Barbara basin, California. In: Everitts, D.J., Paul, R.G., Eaton, C.F., Welday, E.E. (Eds.), California Offshore Gas, Oil and Tar Seeps. California State Lands Commission, Sacramento, California, pp. 1–62.

Hornafius, J.S., Luyendyk, B.P., Kamerling, M.J., 1996. Seismic Mapping of the North Channel Fault Near Santa Barbara, California, vol. 2. Annual Rep Southern California Earthquake Center, pp. D13–D17, 1995.

Hornafius, J.S., Quigley, D., Luyendyk, B.P., 1999. The world's most spectacular marine hydrocarbon seeps (Coal Oil Point, Santa Barbara Channel, California): quantification of emissions. J. Geophys. Res. 104 (C9), 20703–20711. https://doi. org/10.1029/1999JC900148.

Kamerling, M., Horner, S., Thompson, L., 2003. The Monterey Formation at South Ellwood field, Santa Barbara channel, California. In: Proceedings Society of Petroleum Engineers Western Regional/AAPG Pacific Section Joint Meeting, Long Beach. California, Bakersfield, CA, USA. May.

Key, K., 2016. MARE2DEM: a 2-D inversion code for controlled-source electromagnetic and magnetotelluric data. Geophys. J. Int. 207 (1), 571–588.

Leifer, I., 2010. Characteristics and scaling of bubble plumes from marine hydrocarbon seepage in the Coal Oil Point seep field. J. Geophys. Res.: Oceans 115 (C11).

Leifer, I., 2019. A Synthesis Review of Emissions and Fates for the Coal Oil Point Marine Hydrocarbon Seep Field and California Marine Seepage. Geofluids, 2019.

Leifer, I., Boles, J., 2005a. Measurement of marine hydrocarbon seep flow through fractured rock and unconsolidated sediment. Mar. Petrol. Geol. 22 (4), 551–568.

Leifer, I., Boles, J., 2005b. Turbine tent measurements of marine hydrocarbon seeps on subhourly timescales. J. Geophys. Res.: Oceans 110 (C1).

Leifer, I., Kamerling, M.J., Luyendyk, B.P., Wilson, D.S., 2010. Geologic control of natural marine hydrocarbon seep emissions, Coal Oil Point seep field, California. Geo Mar. Lett. 30, 331–338, 3–4.

Leifer, I., Roberts, D., Margolis, J., Kinnaman, F., 2006. In situ sensing of methane emissions from natural marine hydrocarbon seeps: a potential remote sensing technology. Earth Planet Sci. Lett. 245, 509–522, 3–4.

Leifer, I., Wilson, K., 2007. The tidal influence on oil and gas emissions from an abandoned oil well: nearshore Summerland, California. Mar. Pollut. Bull. 54 (9), 1495–1506.

Lorenson, T.D., Hostettler, F.D., Rosenbauer, R.J., Peters, K.E., Dougherty, J.A., Kvenvolden, K.A., Gutmacher, C.E., Wong, F.L., Normark, W.R., 2009. Natural Offshore Oil Seepage and Related Tarball Accumulation on the California Coastline – Santa Barbara Channel and the Southern Santa Maria Basin; Source Identification and Inventory, p. 116. USGS Open-File Report 2009-1225.

MacKinnon, T.C., 1989. Petroleum geology of the Monterey Formation in the Santa maria and Santa Barbara coastal and offshore areas. Oil in the California Monterey Formation: Field Trip Guide Bk. 311, 11–27.

Mitchell, G.A., Orange, D.L., Gharib, J.J., Kennedy, P., 2018. Improved detection and mapping of deepwater hydrocarbon seeps: optimizing multibeam echosounder seafloor backscatter acquisition and processing techniques. Mar. Geophys. Res. 39, 323–347, 1–2.

Meyer, D., Constable, S., Key, K., 2011. Broad-band waveforms and robust processing for marine CSEM surveys. Geophys. J. Int. 184 (2), 689–698. https://doi.org/10.1111/ j.1365-246X.2010.04887.x.

Ogle, B.A., Wallis, W.S., Heck, R.G., Edwards, E.B., 1987. Petroleum Geology of the Monterey Formation in the Offshore Santa Maria/Santa Barbara Areas. Prentice- Hall, Englewood Cliffs, New Jersey, pp. 382–406.

Orange, A., Key, K., Constable, S., 2009. The feasibility of reservoir monitoring using time-lapse marine CSEM. Geophysics 74 (2).

Razaz, M., Di Iorio, D., Wang, B., Asl, S.D., Thurnherr, A.M., 2020. Variability of a natural hydrocarbon seep and its connection to the ocean surface. Sci. Rep. 10 (1), 1–13.

Sherman, D., Kannberg, P., Constable, S., 2017. Surface towed electromagnetic system for mapping of subsea Arctic permafrost. Earth Planet Sci. Lett. 460, 97–104.

Sliter, R.W., Triezenberg, P.J., Hart, P.E., 2008. High-Resolution Chirp and Mini-Sparker Seismic-Reflection Data from the Southern California Continental Shelf–Gaviota to Mugu Canyon.

Tennyson, M.E., Kropp, A.P., 1998. Regional cross section across Santa Barbara channel from northwestern Santa rosa island to Canada de Molino. In: Kunitomi, D.S., Hopps, T.E., Galloway, J.M. (Eds.), Structure and Petroleum Geology, Santa Barbara Channel, California, Miscellaneous Publication 46. Pacific Section AAPG, Bakersfiled, CA, pp. 185–193.

Treiman, J.A., 2006. Fault number 90, Red Mountain fault zone in Quaternary fault and fold database of the United States. US Geol. Survey Available at. https://earthquakes.usgs.gov/hazards/qfaults.

Washburn, L., Clark, J.F., Kyriakidis, P., 2005. The spatial scales, distribution, and intensity of natural marine hydrocarbon seeps near Coal Oil Point, California. Mar. Petrol. Geol. 22 (4), 569–578.

# CHAPTER 5

# How low can you go: an investigation of sensitivity and resolution with depth using towed marine CSEM systems.

*Co-author: Steven Constable*

This chapter, in full, has been submitted for publication. King, R.B. & Constable, S. How low can you go: an investigation of sensitivity and resolution with depth using towed marine CSEM systems. The dissertation author was the primary investigator and author of this material.

## 5.1 Abstract

Understanding the depth of investigation for electromagnetic and electrical methods is important in experimental design and for interpreting inversions. Many studies have defined the depth of investigation for electromagnetic sounding methods, but none have included continuously towed CSEM methods. Nodal CSEM surveys using ocean-bottom electromagnetic (OBEM) receivers have generally been found to have a depth of investigation limited to about half the maximum source–receiver spacing, but experience using continuously towed arrays suggests a sensitivity to targets at depths approaching the source–receiver spacing. We test this on 2D synthetic data using two methods. A rigorous approach is to re-invert data as a highly conductive or resistive basement is included at successively shallower depths. When the data misfit becomes unacceptably high we can conclude that the maximum depth of inference has been passed. Rather than use overall misfit, we note that it is more realistic to examine the data sensitive to largest depths (longest offsets and lowest frequencies). A more practical approach is to determine the depth at which a conductivity contrast can be imaged by inversion, noting that

knowledge of a contrast is geologically useful even if the actual conductivities cannot be recovered. Both approaches confirm that the increased data density of towed EM systems increases the depth of investigation to about the maximum offset distance.

## 5.2 Introduction

The depth of investigation (DOI) of electrical and electromagnetic methods has been of interest since the Schlumberger brothers first started to develop electrical methods for geophysical prospecting (Schlumberger & Schlumberger, 1932). Some understanding of the DOI is essential to the design of geophysical surveys – if the geology of interest is thought to be, say, one kilometer deep, then it is pointless using a geophysical method that optimistically has a maximum DOI of 500 m. The study presented in this paper investigates the practical DOI for continuously towed, dipole-dipole, marine controlled-source electromagnetic (CSEM) methods, such as those described by Edwards (1997), Ming et al. (2010), Schwalenberg et al. (2010), Engelmark et al. (2014), Constable et al. (2016), Sherman et al. (2017), and Wang et al. (2017). While marine CSEM methods using ocean-bottom electromagnetic (OBEM) receivers are generally thought to have a DOI limited to about half the maximum source–receiver spacing (e.g., Constable, 2010), recent studies using deep- and surface-towed CSEM arrays suggest that structure as deep as the maximum source-receiver spacing is resolvable (Kannberg & Constable, 2020; King et al., 2022). However, one reviewer of the King et al. paper questioned the method's ability to resolve such deep structures. While beyond the scope of the King et al. paper, this is an important question worthy of further study. Here we show that continuously towed systems are indeed sensitive to depths as deep as the maximum source–receiver separation.

Marine CSEM surveys combine both parametric (variable frequency) and geometric (variable source–receiver spacing) sounding in order to control depth sensitivity. Both magnetotelluric (MT) sounding and time domain electromagnetic (TEM) sounding are parametric methods. The depth penetration of MT signals is controlled by (1) period, $T$, through the skin depth, $z_s$, which is dependent on electrical conductivity, $\sigma$, and for a uniform conductor is given by:

$$z_s = \sqrt{\frac{2T}{\sigma\mu_o}} \tag{1}$$

or the distance over which electric and magnetic fields decay by about 37%. The DOI for MT is about 1.5 skin depths in simple structures, but since the MT magnetic source field spectrum increases as frequency decreases (i.e., a red spectrum), for MT the DOI is limited only by the time taken to make the measurement (or until the electric field response becomes too small – at which point geomagnetic depth sounding can be used instead).

For TEM sounding, Spies (1989) showed (2) that the analogous quantity is the time-domain diffusion depth:

$$z_t = \sqrt{\frac{2t}{\sigma\mu_o}} \tag{2}$$

where $t$ is the time after transmitter switch-off. Again, the diffusion depth is dependent on conductivity, but since the signal to noise ratio of the longest measurement time is given by the power of the transmitter (and is degraded by a red noise spectrum), the DOI for TEM methods is limited by instrumentation.

DC resistivity sounding is purely geometric. Roy and Apparao (1971) estimated the DOI of various resistivity arrays as $0.25L$ at best, where $L$ is the largest electrode spacing, assuming transmission current is high enough to make measurements with this electrode spacing.

In marine CSEM sounding, an electric transmitter antenna is towed through the water while emitting a current shaped by some waveform. Because of the highly conducting seawater, currents of up to 1,000 amps are achievable, and 100 amps are possible with only a few kilowatts of power. Time domain can be used, but a modified square wave with a broad frequency content is more efficient (Connell & Key, 2013) since the energy is concentrated in delta functions at the frequencies of the discrete harmonics. Classically, OBEM receivers are placed on the seafloor to record transmissions at distances of several tens of kilometers, at which point signals become too small to be measured. As long as the skin depth in the seafloor at the lowest frequency is large enough, the DOI is determined by the maximum source–receiver offset at which the signal to noise ratio is adequate. Constable (2010) estimated this to be about half the source–receiver spacing for OBEM surveys based on a perturbation analysis. Constable and Cox (1996) and Key et al. (2012) observed similar depths for real data using the maximum depth of inference method of Parker (1982). As an alternative to deploying ocean-bottom instruments, receivers spaced at regular intervals can be towed behind the transmitter, up to a fixed maximum offset, and is the subject of the current paper.

## 5.3 Maximum Depth of Inference

Skin depth and diffusion time provide only approximate guidelines as to the DOI that might be achieved by a given method. In practice, the DOI will depend on data quality (signal to noise ratio), conductivity structure, as well as the parameters/geometry of the method. In other

words, it will be specific for every survey and will vary across a particular 2D or 3D model. It is also important to distinguish between *sensitivity* and *resolution*. An inversion of a data set may include structure at depth that, when removed, degrades the model's fit to the data. Clearly then, the data are sensitive to structure at this depth for this particular model, and the sensitivity kernels can extend to considerable depth, but that does not mean that this particular structure must be included in some other model. That is, it is possible that the structure is not truly resolved by the data.

The most rigorous approach to this question was outlined by Parker (1982). Armed with the analytical least squares solution to the one-dimensional (1D) MT problem developed by Parker and Whaler (1981), Parker introduced an infinite conductor at increasingly shallow depths and repeatedly inverted the rest of the model to see if the data could still be fit to an acceptable level. The maximum depth of inference was defined when the rest of the model could not compensate for the infinite conductor and the data misfit became statistically unacceptable. Although not as rigorous as the study presented by Parker (1982), modern derivative-based algorithms such as the Occam algorithm of Constable et al. (1987) can in practice fit the data as well as is practically possible, and so can be used to re-invert a data set as the model is terminated by an extreme conductor or resistor at increasingly shallow depths. Once the algorithm cannot find an acceptable fit to the data, the maximum depth of inference is defined.

Model regularization provides some insight as to DOI. If structure is penalized, the model will go featureless at some depth. If the penalty is against a starting model, then the inversion will revert to this model at depths too deep to constrain. Oldenburg and Li (1999) exploited this by inverting data using different starting models and compared the results to infer DOI. Many schemes use information in the Jacobian matrix, the derivatives of data with respect to model

parameters, to infer the DOI for a particular data set (see, for example, the recent paper of Christensen, 2022). Ultimately, stochastic inversion, the so-called Bayesian methods, can be used to infer model resolution, but currently these require a prohibitive amount of computation for any but 1D models.

Our current paper does not seek to add to the rich literature on a-posteriori model assessment. Rather, we ask a simpler, but very important question: Do the continuously towed CSEM methods have a deeper DOI than one would infer from other geometric sounding methods such as resistivity, or the conventional OBEM type CSEM surveys? This is important because of the logistical limits of towed arrays. Increasing the length of an array makes towing close to the seafloor hazardous, and loses more time during turns. However, deploying OBEM instruments to extend source–receiver offsets adds considerable additional expense to a survey. Our hypothesis is that the increased data density of towed arrays contributes to an improved DOI, and so we take a 2D approach to this study in order to capture the behavior of typical data sets. There is some evidence that 1D analysis significantly underestimates the DOI (Sherman, 2018) since the full data density of continuous towing is not captured. There is also a pragmatic aspect to a 2D approach – variations in resistivity at depth along a survey line can provide useful information on geological structure, even if the true resistivities cannot be resolved.

## 5.4 Two-Dimensional Tests of Maximum Depth of Inference

The rigorous test used below was first developed by Parker (1982) for 1D electromagnetic induction. Parker's test aimed to resolve the depth in which the addition of a conductive or resistive layer ceases to influence magnetotelluric admittance. We have expanded

this test into 2D media using the publicly available MARE2DEM inversion and modeling code of Key (2016).

We tested the maximum depth of inference for three commonly-used CSEM systems: the conventional OBEM type CSEM surveys referred to as a nodal system from hereon, a deep-towed system, and a surface-towed system. We aimed to find the relationship between source-receiver offset and DOI in these differing systems. Despite the obvious benefit of potentially high source-receiver offsets gained from the use of a nodal system, we chose to limit maximum source-receiver offsets in all three systems to 1000 meters in order to make a direct comparison. Additionally, as we aim to test the depth of sensitivity of these systems in regards to geometric sounding, a 0.25 Hz waveform-D (Myer et al., 2011) was used. This frequency results in a skin depth of approximately ~1400 meters in typical marine sediments, well below the previously encountered sensitivity limits of these three systems.

### 5.4.1 Forward Model Design

Synthetic response data were generated from 1 $\Omega$m half-space models representative of typical survey environments encountered by all three CSEM system types. The model parameters for each starting model are shown in Table 5.1. All three systems use a towed transmitter which advances through the model in 50-meter increments to mimic 30-second stacking intervals often used in EM processing to increase signal-to-noise. In the nodal models, the receivers remain in place on the seafloor while the transmitter is towed 50 m above the seafloor; in towed-systems the entire array advances with the transmitter, either 50 m above the seafloor or on the sea surface. Using these parameters, we ran forward models to obtain response functions. Vertical and inline responses were used in the deep-towed system models while only inline responses were included in the nodal and surface-towed system models, consistent with

typical survey design. To mimic the environmental and navigational noise common in marine surveys, 2 percent random Gaussian noise was added to all synthetic data used in these tests before being included in the inversions. As surface-towed systems receive a GPS timing pulse during typical surveys, noise associated with phase response is lower than the noise in the amplitude data. Therefore, we added only 1 percent random Gaussian noise to the synthetic phase data for the surface-towed data to most closely simulate noise encountered in these types of surveys.  (Although the absolute noise floor is much smaller for nodal systems than towed systems, at the 1,000 m offsets modeled here all data are above the absolute noise floor.)

Table 5.1: Model parameters used in 2D tests of maximum depth of inference

| System | Nodal | Deep-Towed | Surface-Towed |
|---|---|---|---|
| Seawater Resistivity (ohm m) | 0.3 | 0.3 | 0.225 |
| Depth to Seafloor (m) | 1000 | 1000 | 50 |
| Receiver Depth (m) | 999.9 | 950 | 0.67 |
| Transmitter Depth (m) | 950 | 950 | 1.5 |
| Number of Receivers | 9 | 4 | 4 |
| Receiver Spacing (m) | 500 | 250 | 250 |

*5.4.2 Inversion Parameters and Maximum Depth of Inference*

The synthetic data generated from half-space models were included in a series of inversions in which a 1000 $\Omega$m resistor was added iteratively at varying depths from 500 meters to 2000 meters below the seafloor (mbsf). The resistor, air, and seawater were fixed parameters reducing the free region for inversion to be between the seafloor and the resistor. The inversions were allowed to run until either an RMS of 1 was achieved or the model could no longer improve the fit to the data.  Tests were also run with the addition of a conductor; however, depth constraints derived from conductive layer tests were deeper than those derived from the addition of a resistor so we limit discussion to only the results gained from tests using a resistor at depth.

### 5.4.3 Lessons in Data Fit

Inversions were run for the three systems and the final depth of inference was determined from overall RMS. These results are shown in Table 5.2. One may note that the nodal system was less sensitive to the addition of a resistor at depth. However, a 700-meter depth of inference for nodal systems is still an improvement to previous estimates using 1D sensitivity tests which indicated a loss of sensitivity at approximately 50 to 60 percent of the total source-receiver offset (Constable, 2010; Key et al., 2012). This improvement in depth of sensitivity may not necessarily be due entirely to the change from 1D tests to 2D tests, which significantly increases the overall data included, but may also be a result of lower noise used in our tests versus the noise encountered in early applications of this system. The surface-towed system could no longer fit the data to an RMS of 1 when a resistor was added 800 mbsf and the deep-towed system could no longer fit the data to an RMS of 1 when a resistor was added 900 mbsf. This indicates that the initial observations that the depth of inference for marine CSEM systems is around half of the maximum source-receiver offset is not accurate for towed systems. Instead, the depth is improved to 80 to 90 percent of the maximum source-receiver offset, probably due to the density of data made possible by continuously towing the receiver array.

Table 5.2: Depth of inference obtained from overall RMS value compared to inequal RMS values from data channels

| System | Nodal | Deep-Towed | Surface-Towed |
|---|---|---|---|
| Depth of Inference (mbsf) from overall RMS value | 700 | 900 | 800 |
| Depth of Inference (mbsf) from >20% change in RMS in at least one data channel | 700 | 1500 | 900 |

It is worth noting that when the model is broken down by receiver, amplitude, and phase, more information as to the behavior of the models with the addition of a resistor can be gained.

For example, bias in the residuals of the data begins to develop before the overall RMS of the model indicates poor fit to the data (see Fig. 5.1). From the plots in Fig. 5.1, the RMS from the lowest frequency data, both amplitude and phase, tends to increase before the overall fit to the data can no longer achieve an RMS of 1. Most prominently, the RMS associated the 0.25 Hz phase data from the deep-towed system tests approaches an RMS of 1.2 at a depth of 1500 mbsf, 600 meters deeper than the depth of inference inferred from overall RMS. This can also be seen in the surface-towed 0.25 Hz amplitude data, but to a lesser degree. Interestingly, in all three systems, the RMS from the amplitude and phase responses do not linearly increase as the overall RMS increases. Instead, the RMS of the amplitude and phase responses tend to oscillate between higher and lower RMS values. This could be due to prior iteration results placing structure within the free portions of the models resulting in complicated interactions between the model fit at different frequencies.

These changes in the individual RMS values associated with different response data indicates that the model is influenced by the addition of a resistor at greater depths than was inferred by the overall RMS. To further illustrate the formation of structure, or bias, within the models with the addition of the resistor, histograms of the residuals for the furthest receiver in the array of the surface-towed system for several sensitivity tests are presented in Fig. 5.2. When a resistor is placed in the models 2000 mbsf, the residuals from the lowest frequency phase data are nearly indistinguishable from zero-mean normal distribution (plotted in red in Fig. 5.2.). However, as the resistor is moved toward the seafloor, the residuals in the lowest frequency of phase data begin to deviate from a normal distribution and the mean of the residuals moves away from zero.
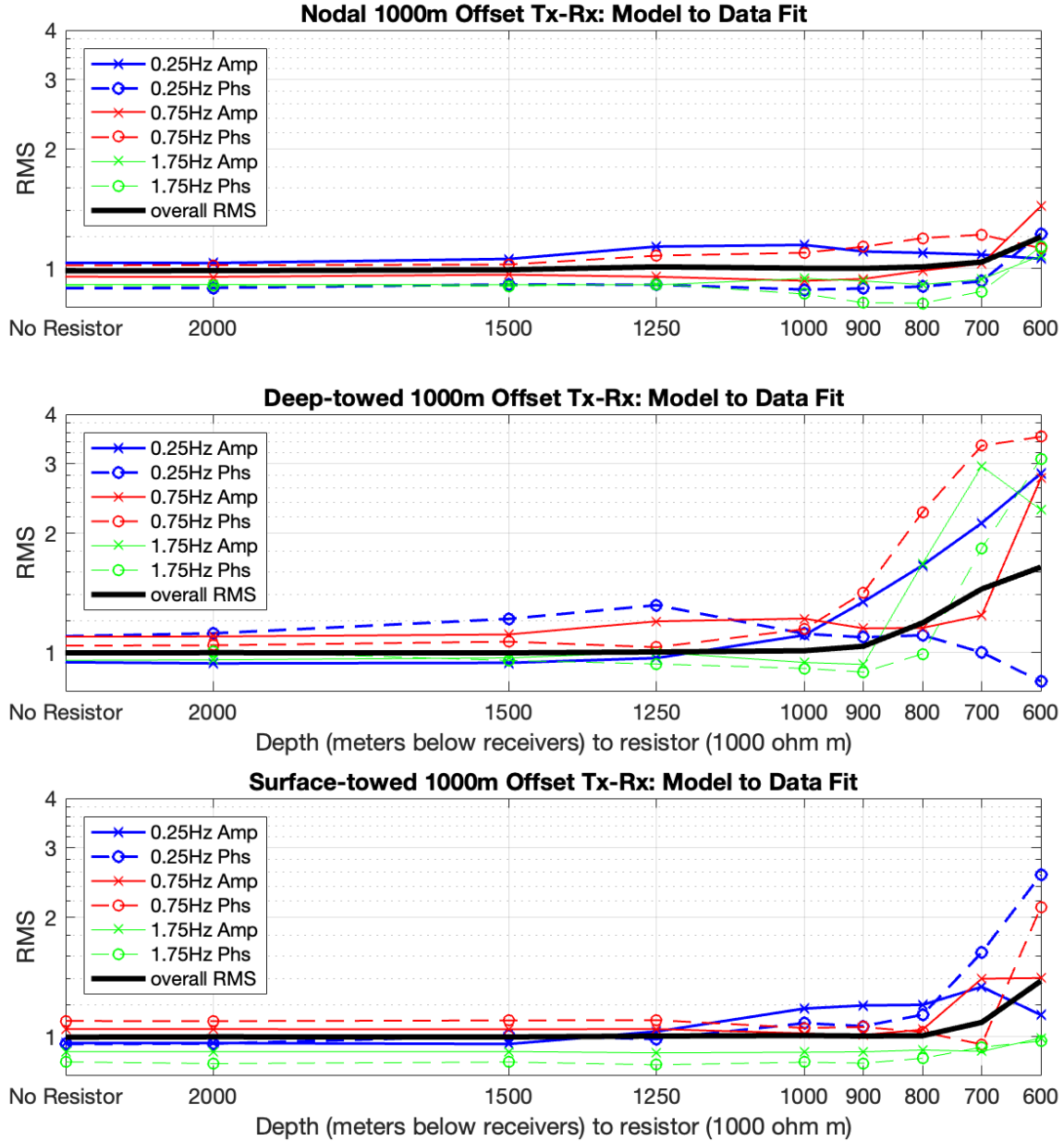
Fig. 5.1: Overall RMS of the model and RMS from individual data groupings from the receiver with the maximum source-receiver offset are plotted for all three CSEM system sensitivity tests as a terminating resistor is made successively shallower. On the far left, the RMS values are plotted for a half-space model, indicated here as 'No Resistor'.

This suggests that one should not rely heavily on total RMS unless the residual

distribution is random, but instead investigate data fit and possible signs of bias within the

residuals. The development of structure in the residuals indicates that the models may be
sensitive to the resistor at greater depths than is inferred by the RMS value of the model as a
whole. It also suggests that the model may be influenced by these resistive features at depth, but
is able to accommodate the resulting misfit in one data type by overfitting the data in another. It
is therefore advisable to review the entirety of the model fit to the data, as structure in the
residuals may be indicative of potential features at depth.
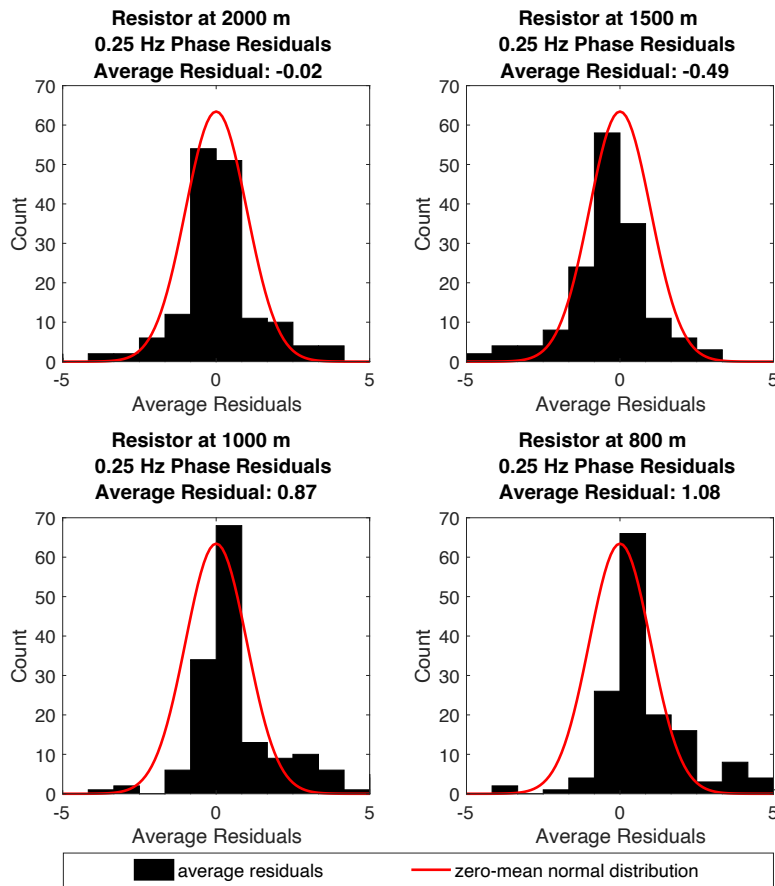


Fig. 5.2: Histograms of normalized residuals for 0.25 Hz phase data from the last receiver in the
surface-towed array (1000 meter source-receiver offset) from a series of inversions fitting the half
space data set to RMS 1 with a fixed resistor placed at 800m, 1000m, 1500m, and 2000m. As the
resistor decreases in depth, the residuals become biased away from a zero-mean normal
distribution. A zero-mean normal distribution is plotted in red on each plot for comparison to the
residual distributions.

## 5.5 Resolution with Depth

To gain greater insight into the DOI of these CSEM systems, we can also investigate the limits of resolution by asking: at what point are we no longer able to resolve structure at depth? For these tests, we created a series of quarter space models that included a 100 $\Omega$m feature that was moved iteratively toward the seafloor in a series of tests. For the sake of clarity, we will refer to this resistor included in the quarter space models as the 'starting QS resistor'; the starting QS resistors are outlined with a dashed white line for all models shown in Fig. 5.3. Forward models were run on each of these quarterspace models to obtain responses using the three CSEM systems. The responses were then degraded with 2 percent gaussian noise and inverted. The starting models used the same parameters as shown in Table 1 and the seawater and air in all the models were set as fixed parameters. The region below the seafloor was set as a free parameter and initialized to a uniform starting resistivity of 1 $\Omega$m. Inversion parameter grids were constructed using 50-meter-wide quadrilateral cells that increased in height with depth. The models were run until the models achieved an RMS of 1 before comparing the results.

Examples of the resulting models from all three systems are plotted in Fig. 5.3. When the starting QS resistor is well within the sensitivity limits predicted in the previous section of this paper, a strong resistor of the correct approximate size and shape is resolved in the inversions. However, the resistivity of the starting QS resistor is never truly attained. Additionally, the depth to the top of the resolved resistor is at a deeper depth than the starting QS resistor. As these are not parameterized inversions, it is not surprising that the starting QS resistivity values are not resolved and the depth of the resolved resistor is shifted deeper, as regularized inversion drives the model toward the smoothest solution possible while still fitting the data. The Occam's inversion algorithm attempts to fit a step function in resistivity by smoothing the true amplitude

91

of the step, which has been noted in a variety of publications since the algorithm was first released (e.g. Key, 2009). This results in a Gibbs type oscillation in the structure of the inversions which is evident in Fig. 5.3 by the downward shift of the peak resistor (defined as the maximum resistivity value encountered in the inversion) from the starting QS resistor depth, but also by the addition of a minor conductor above the resistor.

When the starting QS resistor is placed at the sensitivity limit obtained in the previous section, a resistive feature must be included in the inversion to achieve an RMS of 1, but the resistivity of that feature is near the starting resistivity of the model (1 $\Omega$m) (see Fig. 5.3 f, g, and h). In tests with a starting QS resistor at 1100 mbsf, a faint resistor was needed in the final inversions to achieve fit to the data in towed systems, suggesting a resolution limit of approximately 110% of maximum source-receiver offset in these systems. For nodal systems, the starting QS resistor was barely resolved in the inversions to a maximum depth of 800 mbsf or 80% of the of the maximum source-receiver offset in these systems.

Previous efforts to estimate sensitivity of non-linear inverse problems have linearized the problem by making use of the Jacobian (or sensitivity) matrix (Farquharson & Oldenburg, 1996; McGillivray et al., 1994), even though these methods can be computationally expensive and dependent on data distribution (Farquharson & Oldenburg, 1996). The MARE2DEM code of Key (2022) computes a normalized sensitivity from the Jacobian derivative matrix by normalizing the summation of the Jacobian matrix by area, resulting in a final sensitivity unit of $\log_{10}(S/m)/m^2$. The output sensitivity contours can be useful to understand the depth in which to limit interpretation of the model, although quantitative interpretation can be difficult. One contour of this sensitivity is plotted as a black line in Fig. 5.3. The normalized sensitivity reflects the diminishing sensitivity of the system with depth and conductivity. We found that a

sensitivity value of -3.5 $\log_{10}$(S/m)/m$^2$ generally corresponds with the depth of peak resistivity

values. Below this depth, the resistivity of the feature decreases, indicating diminishing

sensitivity of the CSEM systems below this depth. Additionally, this normalized sensitivity depth

is, of course, driven by skin depth and is thus affected by the resistivity values present within the

model. This can be observed in the left half of all the models presented in Fig. 5.3 where the

sensitivity contour is deeper within the resistive feature (within the bounds of the white dashed

line) compared to the 1 $\Omega$m portion of the quarter space model. This highlights the value of using

these sensitivity contours when interpreting real world data as the structure in the model

influences the depth of sensitivity so each model will have its own unique DOI.
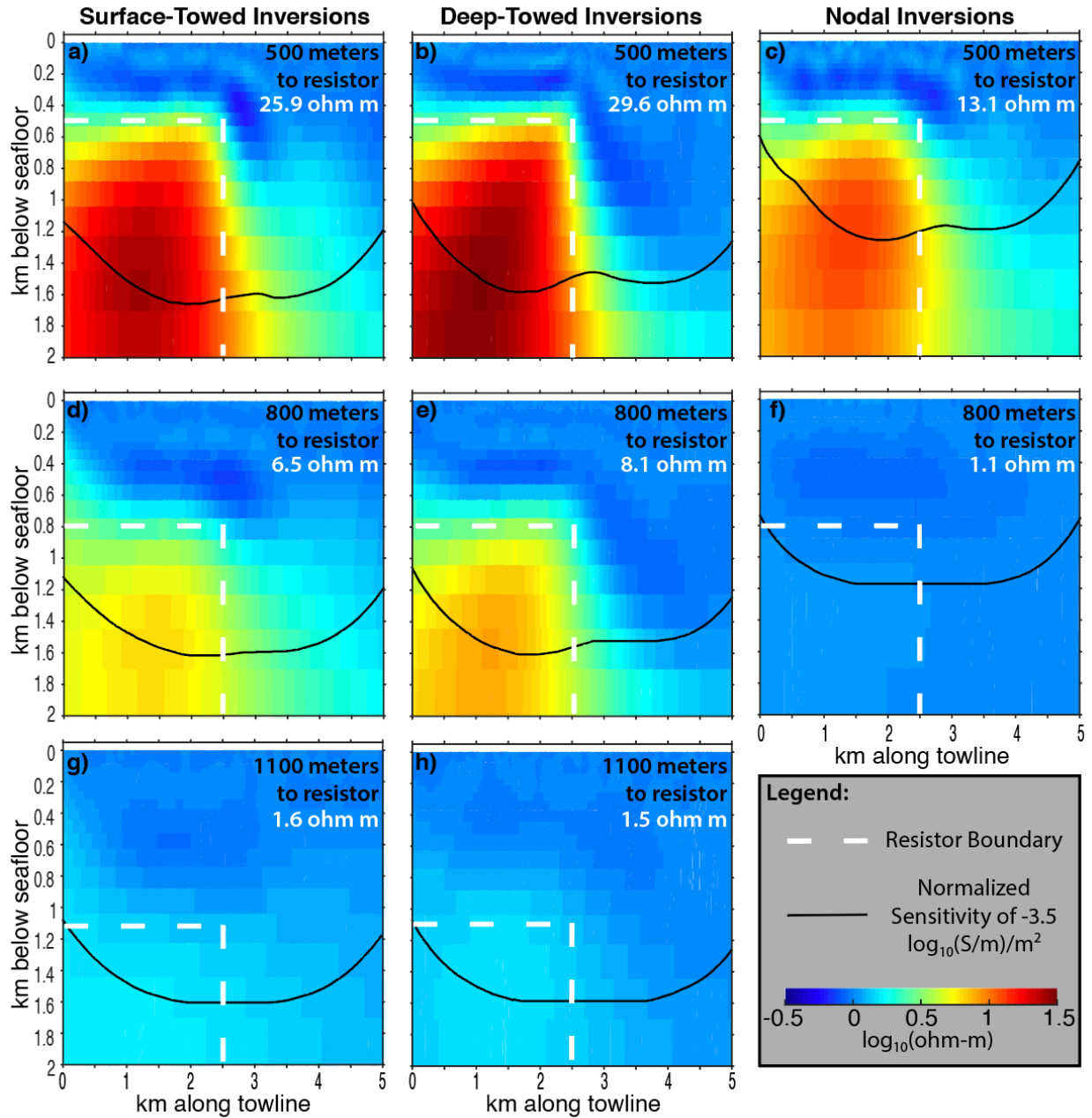
Fig. 5.3: Plots of quarterspace tests of resolution for surface-towed, deep-towed, and nodal CSEM surveys. All inversions presented here have an RMS of 1. The dashed white line indicates the extent of the 100 Ωm starting QS resistor included in the forward model. The black line is a contour of a normalized sensitivity value of -3.5 log10(S/m)/m2 output by the MARE2DEM code.

## 5.6 Discussion

The sensitivity and resolution tests presented here are intended to provide the reader with general information to aid in survey design and in later inversion and interpretation. It is limited

in that there are many other factors such as survey noise, navigational error, or geology that will influence the DOI for any given data set, but we aim to provide insight into the difference between towed CSEM surveys and nodal systems and, more specifically, the tradeoffs between these survey techniques.

Our results indicate that nodal systems have a DOI of approximately 70 percent of the maximum source-receiver offset in ideal scenarios. This ratio of DOI to maximum source-receiver offset is smaller than that achievable with towed CSEM systems. However, since the source-receiver offset in a nodal survey can be increased to much greater values than is possible with a towed array, the ultimate DOI of a nodal system can be extended to deeper depths than towed systems. This has been done in numerous CSEM nodal surveys and, in some extraordinary circumstances, a DOI of approximately 65 km has been achieved (S. Constable & Cox, 1996).

Despite the increased maximum DOI possible with a nodal system, the resolution possible from towed CSEM systems appear to be superior in some sense. This is most likely a result of the higher density of data achieved from continuously towing the array and is a strong argument for use of towed systems, which can also resolve finer-scale shallow structure in the inversions.

## 5.7 Conclusion

Overall, the DOI obtained from the tests presented here indicate that the DOI of both towed and nodal systems are deeper than previously thought. This was observed both with rigorous tests of sensitivity that rely on the depth a resistor would no longer influence overall RMS, but also in less rigorous quarter-space tests of resolution. When maximum source-receiver offset was held constant, the towed systems outperformed the nodal systems in both sensitivity

and resolution tests. Our study highlights the trade-offs between using nodal and towed CSEM

systems when aiming to achieve greater sensitivity with depth of resolution, and can be used to

better optimize surveys for future exploration efforts.

## 5.8 Acknowledgments

## 5.9 References:

Christensen, N. B. (2022). Resolution attributes for geophysical inversion models: Depth of investigation and novel measures. Near Surface Geophysics, 20(1), 3–15. https://doi.org/10.1002/nsg.12188

Connell, D., & Key, K. (2013). A numerical comparison of time and frequency-domain marine electromagnetic methods for hydrocarbon exploration in shallow water. Geophysical Prospecting, 61(1), 187–199. https://doi.org/10.1111/j.1365-2478.2012.01037.x

Constable, S. (2010). Ten years of marine CSEM for hydrocarbon exploration. Geophysics, 75(5). https://doi.org/10.1190/1.3483451

Constable, S. C., Parker, R. L., & Constable, C. G. (1987). Occam' s inversion: A practical algorithm for generating smooth models from electromagnetic sounding data. GEOPHYSICS, 52(3), 289–300.

Constable, S., & Cox, C. S. (1996). Pegasus. Journal of Geophysical Research, 101, 5519–5530. Constable, S., Kannberg, P. K., & Weitemeyer, K. (2016). Vulcan: A deep-towed CSEM receiver. Geochemistry, Geophysics, Geosystems, 17(3), 1042–1064. https://doi.org/10.1002/2015GC006174

Edwards, R. N. (1997). On the resource evaluation of marine gas hydrate deposits using sea-floor transient electric dipole-dipole methods. Geophysics, 62(1), 63–74. https://doi.org/10.1190/1.1444146

Engelmark, F., Mattsson, J., McKay, A., & Du, Z. (2014). Towed streamer EM comes of age. First Break, 32, 75–78. www.firstbreak.org

Farquharson, C. G., & Oldenburg, D. W. (1996). Approximate sensitivities for the electromagnetic inverse problem. Geophysical Journal International, 126(1), 235–252. https://doi.org/10.1111/j.1365-246X.1996.tb05282.x

Kannberg, P. K., & Constable, S. (2020). Characterization and Quantification of Gas Hydrates in the California Borderlands. Geophysical Research Letters, 47(6), no. https://doi.org/10.1029/2019GL084703

Key, K. (2009). 1D inversion of multicomponent, multifrequency marine CSEM data: Methodology and synthetic studies for resolving thin resistive layers. Geophysics, 74(2). https://doi.org/10.1190/1.3058434

Key, K. (2016). MARE2DEM: A 2-D inversion code for controlled-source electromagnetic and magnetotelluric data. Geophysical Journal International, 207(1), 571–588. https://doi.org/10.1093/gji/ggw290

Key, K. (2022, April 20). MARE2DEM: Modeling with Adaptively Refined Elements for 2D Electromagnetics. https://mare2dem.bitbucket.io/about.html

Key, K., Constable, S., Matsuno, T., Evans, R. L., & Myer, D. (2012). Electromagnetic detection of plate hydration due to bending faults at the Middle America Trench. Earth and Planetary Science Letters, 351–352, 45–53. https://doi.org/10.1016/j.epsl.2012.07.020

King, R. B., Danskin, W. R., Constable, S., & Maloney, J. M. (2022). Identification of fresh submarine groundwater off the coast of San Diego, USA, using electromagnetic methods. Hydrogeology Journal. https://doi.org/10.1007/s10040-022-02463-y

McGillivray, P. R., Oldenburg, D. W., Ellis, R. G., & Habashy, T. M. (1994). Calculation of sensitivities for the frequency-domain electromagnetic problem. Geophysical Journal International, 116(1), 1–4. https://doi.org/10.1111/j.1365-246X.1994.tb02121.x

Ming, D., Wei, W., Zhang, W., Sheng, Y., Li, Y., & Wang, M. (2010). Electric field responses of different gas hydrate models excited by a horizontal electric dipole source with changing arrangements. Petroleum Exploration and Development, 37(4), 438–442.

Myer, D., Constable, S., & Key, K. (2011). Broad-band waveforms and robust processing for marine CSEM surveys. Geophysical Journal International, 184(2), 689–698. https://doi.org/10.1111/j.1365-246X.2010.04887.x

Oldenburg, D. W., & Li, Y. (1999). Estimating depth of investigation in dc resistivity and IP surveys. Geophysics, 64(2), 403–416. https://doi.org/10.1190/1.1444545

Parker, R. L. (1982). The existence of a region inaccessible to magneto-telluric sounding (Vol. 68). https://academic.oup.com/gji/article/68/1/165/704026

Parker, R. L., & Whaler, K. A. (1981). Numerical methods for establishing solutions to the inverse problem of electromagnetic induction. Journal of Geophysical Research, 86(B10), 9574–9584. https://doi.org/10.1029/JB086iB10p09574

Roy, A., & Apparao, A. (1971). DEPTH OF INVESTIGATION IN DIRECT CURRENT METHODS. GEOPHYSICS, 36(5), 943–959. https://doi.org/10.1190/1.1440226

Schlumberger, C., & Schlumberger, M. (1932). Electrical Studies of the Earth's Crust at Great Depths. Transactions of the American Institute of Mining and Metallurgical Engineers (Incorporated), 97, 134–140.

Schwalenberg, K., Haeckel, M., Poort, J., & Jegen, M. (2010). Evaluation of gas hydrate deposits in an active seep area using marine controlled source electromagnetics: Results from Opouawe Bank, Hikurangi Margin, New Zealand. Marine Geology, 272(1–4), 79–88. https://doi.org/10.1016/j.margeo.2009.07.006

Sherman, D. E. (2018). Surface-towed controlled source electromagnetic system for mapping extent of subsea permafrost on the Beaufort shelf, Alaska [PhD thesis]. University of California, San Diego.

Sherman, D., Kannberg, P., & Constable, S. (2017). Surface towed electromagnetic system for mapping of subsea Arctic permafrost. Earth and Planetary Science Letters, 460, 97–104. https://doi.org/10.1016/j.epsl.2016.12.002

Spies, B. R. (1989). Depth of investigation in electromagnetic sounding methods. Geophysics, 54(7), 872–888. https://doi.org/10.1190/1.1442716

Wang, M., Deng, M., Wu, Z., Luo, X., Jing, J., & Chen, K. (2017). The deep-tow marine controlled-source electromagnetic transmitter system for gas hydrate exploration. Journal of Applied Geophysics, 137, 138–144. https://doi.org/10.1016/j.jappgeo.2016.12.019

# CHAPTER 6

# CUESI: A near seafloor CSEM system

## 6.1 Introduction

Coastal regions are some of the most densely populated areas on Earth which means that communities living there have a high demand for energy and food sources, but also commonly have limited available land for infrastructure which addresses their needs. Thus, many communities are considering the region offshore as a potential area for infrastructure projects such as wave power systems, aquaculture, and wind farms. As a result, the large-scale development of offshore infrastructure projects has seen significant investment and consideration from industry and political entities all around the world. However, before the construction of any offshore infrastructure projects can begin, baseline studies with minimal seafloor impact of the planned development areas are required. Baseline studies will often involve the collection of data pertinent to the identification and characterization of culturally and biologically sensitive regions, benthic habitats, and seafloor hazards. Additionally, many offshore projects require appropriate seafloor conditions for the anchors and moorings to function. Proper installation of anchors and moorings is dependent on geotechnical conditions such as sediment stratigraphy and porosity in the upper tens of meters of the seafloor.

Bottom-dragged EM surveys have become an established geophysical approach to study changes in seafloor porosity in a variety of shallow seafloor settings (e.g. Cheesman et al., 1993; Evans, 2001, 2007; Evans et al., 1999; Micallef et al., 2020; Schwalenberg et al., 2005, 2010). However, due to their disturbance of the seafloor during data collection, existing bottom-dragged

EM systems are limited to seafloor settings that are heavily sedimented and without protected status, eliminating many seafloor areas from study. Thus, when a project was launched in a National Marine Sanctuary to identify debris piles (e.g., shell middens) left from Pleistocene hunter gatherers, these original bottom-dragged EM systems were not appropriate for use. Instead, a new, neutrally buoyant CSEM system, known as the CUESI (Compact Undersea Electromagnetic Source Instrument) system, was developed to fly between 1 to 2 meters above the seafloor, thereby minimizing seafloor disturbance. The original debris pile targets for this new CSEM system result in subtle changes in porosity in the seafloor, can be small (~3 meter wide and 20 cm thick), and will likely be within the top tens of meters of sediment. To achieve sensitivity to these targets, the CUESI system collects both inline and vertical electric field data and improves resolution in the shallow seafloor by emitting higher frequency signals and using shorter source-receiver offsets than previous systems.

This chapter will describe a series of case studies on the sensitivity and resolution of the CUESI system over a variety of targets offshore Santa Barbara, California and within the Channel Islands Marine Sanctuary, and present preliminary results on a new CSEM system. The goals of these studies are to develop and iterate on a potential new EM tool to collect porosity data of the shallow seafloor for use in offshore infrastructure projects and in studies of shallow subseafloor character.

## 6.2 Existing Systems

Inductive electromagnetic methods rely upon the skin depth, which describes the length scale at which fields decay in conductive media. The skin depth equation (1) describes the

approximate distance ($\delta$) in meters in which the field amplitudes are reduced to 1/e and phase progresses 1 radian in a uniform medium.

$$\delta = 503(^1/_{\sigma f})^{1/2} \tag{1}$$

Here, $\sigma$ is the conductivity of the medium (Siemens per meter) and $f$ is the frequency of the transmission. One may note that higher frequencies would sample shallower geology in the seafloor, whereas lower frequencies would be sensitive to deeper depths. Thus, to enhance resolution in the shallow seafloor, higher frequencies are used. However, higher frequency signals quickly diminish in conductive seawater, so the source and receivers need to be close to the seafloor to reduce this effect.

Bottom-dragged systems can minimize the attenuation from the seawater, as well as achieve maximum coupling to the seafloor and simplify navigation in the vertical direction. These EM systems have been developed to characterize and map the top tens of meters of the seafloor over the past three decades to study a range of targets from groundwater discharge to gas hydrates (e.g., Cheesman et al., 1993; Evans, 2001, 2007; Schwalenberg et al., 2005, 2010). However, because these systems are dragged across the seafloor, they can only be used in seafloor settings that are heavily sedimented and without protected status.

This limitation significantly restricts potential survey areas as nearly 41 percent of U.S. marine waters are classified as protected and many offshore infrastructure projects require a baseline study of a planned development area during which the environment should not be significantly altered. Thus, an EM system with minimized impact on the seafloor is essential for surveying in these scenarios and regions. In order to investigate the shallow subseafloor in

protected areas (e.g., marine protected regions, national parks, cultural heritage sites) or beneath regions with rocky or variable benthic habitats, an EM system would need to limit seafloor contact, while not losing sensitivity to the seafloor.

Limiting contact with the seafloor, or 'flying' the system over the seafloor, has the added benefit of potentially collecting vertical electric field data, which are particularly sensitive to changes in near-seafloor resistivity variations (Constable et al., 2016). Indeed, during preliminary sensitivity tests for this study, much of the sensitivity to a small conductive target, representative of an anthropogenic pile of shell debris, was from changes in vertical electric field amplitude. Thus, a 'flying' system was designed which would allow for three-axis electric field receivers. The design is inspired by a system of Sheehan et al. (2014) which was tested and proven to be non-destructive to benthic habitat over a range of seafloor settings.

## 6.3 CUESI system design

The new CSEM system is designed to fly within 1 to 2 meters of the seafloor while minimizing impact on benthic habitats. This system, illustrated in Fig. 6.1, is made up of a negatively buoyant EM transmitter, CUESI, followed by three towfish. CUESI doubles as a depressor weight, dampening the effects of variable tow speeds and surface wave action on the vertical positions of the towfish. To stabilize the position of the source dipole, CUESI transmits the source signal to an instrument towed 10 meters behind CUESI, labeled as the transmitter towfish. Here, a current controlled signal is transmitted into the seawater with two 10 cm long, 1.5 cm diameter soft copper tubing sections held 2 m horizontally apart on the rigid frame of the transmitter towfish (see Fig. 6.2 for a photo of the CUESI array and winch on deck).
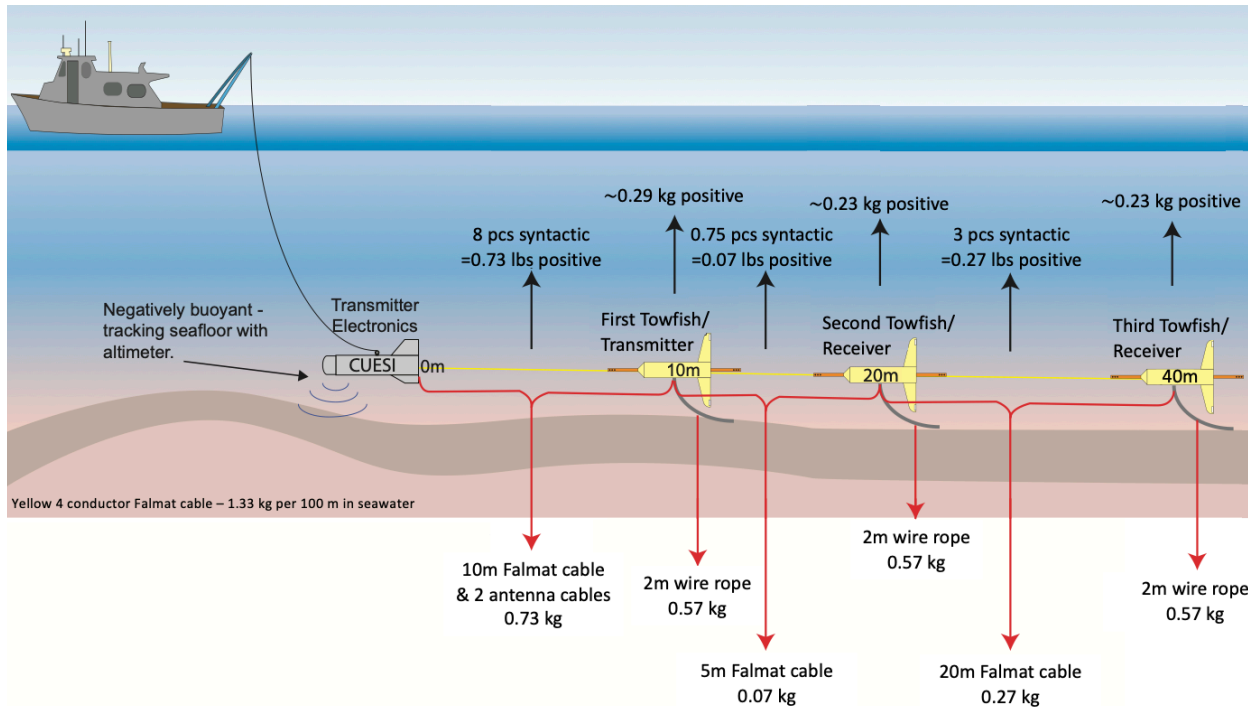
Fig. 6.1: Schematic of the CUESI array with buoyancies for all components labeled. CUESI is negatively buoyant to act as a depressor weight for the array. The towfish are trimmed to tow within 2 meters of the seafloor. Syntactic foam is attached to the cables between the instruments to offset the weight of the cable and wire ropes are attached to the base of each towfish to act as counterweights.

The following two towfish, labeled as receiver towfish, are the three-axis electric field "Vulcan" receivers of Constable et al. (2016). These receiver towfish are tethered and towed 20 meters and 40 meters behind CUESI. All three of the towfish are designed to be slightly positively buoyant instruments (noted in Fig. 6.1) with a small counterweight in the form of a short cable affixed to the base of each frame. When the cable contacts the seafloor, the overall buoyancy of the towfish becomes neutrally buoyant, allowing the frame to maintain a 1 to 2 meters distance from the seafloor depending on water conditions. A similar 'flying' array design was included in a study comparing a variety of bottom-towed systems for seafloor disturbance (Sheehan et al. 2014). This design was incorporated into the CUESI system design because the

'flying' array was found to be non-destructive to the benthic habitats even over a range of seafloor settings.
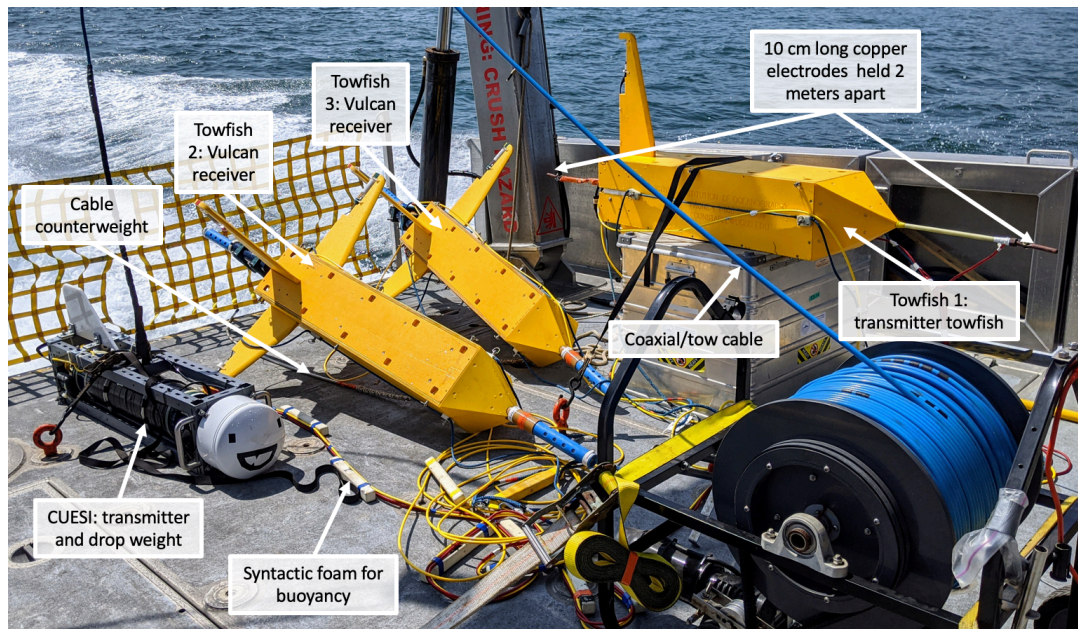


Fig. 6.2: CUESI system ready for deployment on the back deck of a vessel with several components labeled. Yellow cable spooled around the towfish is the telemetry and towing cable connecting the towfish together and to CUESI. The red cable on deck is the antenna cable supplying power from CUESI to the electrodes mounted on towfish 1. The blue cable is the coaxial/tow cable connecting CUESI to the vessel.

## 6.4 CUESI system build

The CUESI system was initially developed to detect the debris pile sites, known as shell middens, of Pleistocene hunter-gatherers submerged offshore from the northern Channel Islands. Some of these sites straddle the present shoreline and others may be theoretically located in waters as deep as 110 meters. The initial research goals aimed to target the submerged sites in a range of water depths from 5 to 110 meters. Vessels capable of navigating these shallow water depths are typically smaller and without specialized towing equipment. Thus, during the development of the CUESI system, deck-space, instrument weight, and power limitations were considered and incorporated into the design.

The CUESI system was developed at the Scripps Marine Electromagnetic Laboratory which also developed the three-axis electric field receivers known as 'Vulcans' (Constable et al., 2016;. Weitemeyer et al., 2006; Weitemeyer & Constable, 2010). These Vulcan receivers are included as towfish in the CUESI system array. The last two towfish in the array are standard Vulcan receivers as described by (Constable et al., 2016) that have been altered only to change buoyancy, affix counterweight cables, and reduce gain on the loggers to avoid signal saturation associated with the reduced source-receiver distances. The first towfish, the transmitter towfish, in the array is a Vulcan that has been altered to function as a mount for the horizontal electric dipole. This Vulcan also has a counterweight cable and the buoyancy has been trimmed. Most notably, the first Vulcan is altered to only record the vertical electric field with a nominal gain of 1 on a set of stainless steel electrodes.

This chapter discusses the most recent build of the CUESI system. See Appendix A for more information on the iterative development and initial tests of the system.

### 6.4.1 CUESI hardware

CUESI, pictured in Fig 3, is 140 cm long, 23 cm wide, and 60 cm in height (including the tail wing; 31 cm without wing). The frame is constructed with stainless steel Unistrut fittings that are welded and reinforced at the joints for added support. The frame weighs approximately 140 lbs in air and is outfitted with handles at the front and aft of the instrument to simplify recovery and deployments. The frame is attached to the tow cable slightly aft of center so the instrument will have minimal pitch when towed through the water. Following initial field tests, the tow point was redesigned to have a single pivot point, reducing the range of motion of the instrument. The frame is open sided to reduce drag in the water and provide ease of access to the instrumentation inside. A camera in a pressurized case on a pivot bar, a LED light, a CT sensor,

an altimeter, a depth sensor in pressure bottle (not pictured), and a pressure case are all mounted inside the CUESI frame.

Power and communications from topside are transmitted through the towline to CUESI with a single coaxial cable. Commands from the user are given using a frequency shift key at 30 characters per second. Within CUESI, the 110 VAC vessel power is transformed down to 10 VAC, rectified, and switched under computer control, to provide arbitrary binary or ternary waveforms switched in increments of 1/2000 second time units. The timing and switching of the waveform are controlled by internal CUESI hardware using specifications given by the user and stabilized using an internal Seascan oscillator/clock. The Seascan clock is synchronized to GPS time before launch and maintained by an internal battery to avoid timing disruptions associated with power interruptions or surveying complications. CUESI outputs a current-controlled waveform of up to 10 amps on a 2 meter horizontal electric dipole mounted on the transmitter towfish.
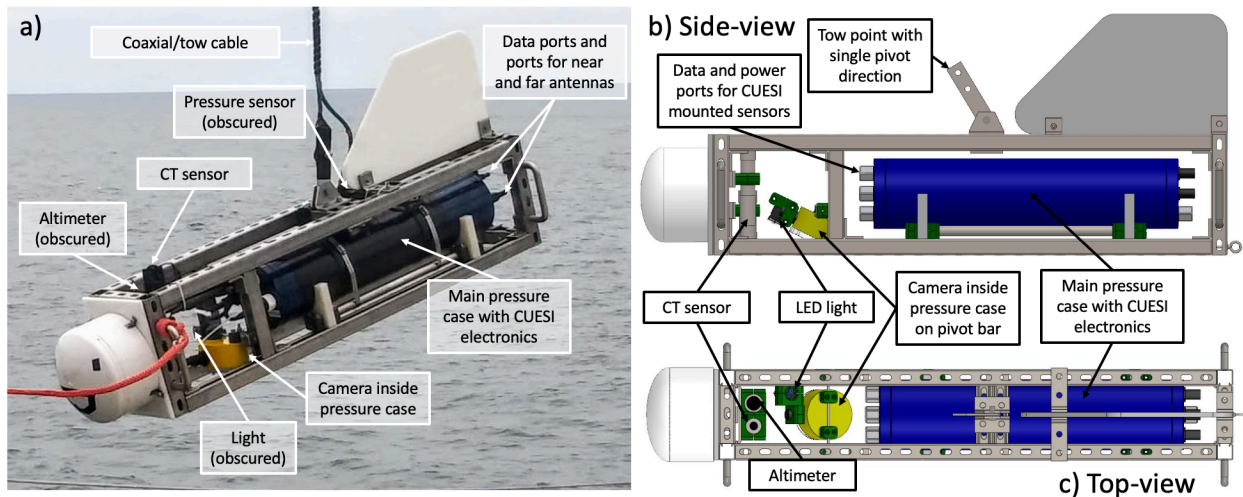


Fig. 6.3: a) Photo of CUESI during pier tests with sensors and frame-mounted instruments labeled. The pressure sensor was not attached during this test, but the location of the sensor is indicated. B) Schematic of the side-view of CUESI. C) Schematic of the top-view of CUESI.

### 6.4.2 Telemetry for real time navigation

The CUESI system is designed to be towed within 5 meters of the seafloor. Therefore, accurate navigation data must be received in real-time from the full instrument array to avoid impact with the seafloor and troubleshoot problems with navigation.

All three towfish telemeter the output from a depth sensor in each towfish as well as time, pitch, roll, and heading to CUESI via a data port. The towfish are strung together via data ports with a tow cable that consists of two twisted pairs of polypropylene insulated 22 AWG copper wire, a para-aramid strength member, and an outer jacket of polyurethane. The shared transmission cable for telemetry means that information traveling up the cable could be subject to 'cross talk' if the instruments telemetered information at the same time. To avoid telemetry interference, the instruments have a staggered start time and frequency of communications to telemeter information to CUESI.

Once the towfish navigation is sent to CUESI, this information is included in the data stream being sent topside using a microprocessor within CUESI. CUESI includes altitude readings from the altimeter, output current and voltage, sea temperature and conductivity, and time in the data package sent topside. Topside, navigation data for each instrument may be monitored in real-time to ensure consistent towing altitudes. If necessary, tow speeds may be adjusted or CUESI may be lifted or lowered using winch controls to correct tow heights. In most settings, towing CUESI between 2 to 5 meters off the seafloor allowed the towfish to maintain a consistent distance of 1 to 3 meters from the seafloor (see Fig. 6.4 show image of towing heights of the array). This configuration also had the added benefit of effectively maneuvering the array to account for changes in the bathymetry or to avoid seafloor obstacles.
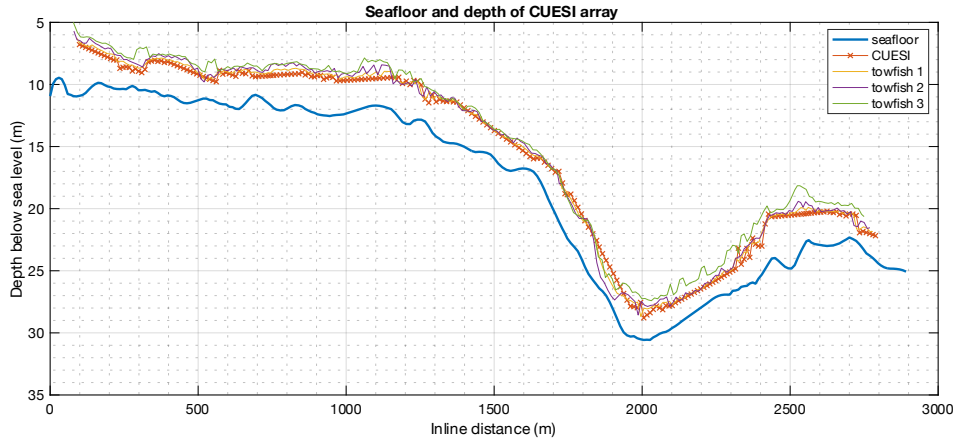
Fig. 6.4: Plot of the depth of the array while surveying. The towfish maintained a distance between 1 to 4 meters off the seafloor during the survey.

### 6.4.3 Time correction signal

Each towfish records electric field data that are timestamped with an internal Seascan clock. These clocks have drift rates of approximately 2 milliseconds per day. To achieve more accurate timing measurements and as a redundancy within the tow packages, CUESI also sends a digital signal corresponding to the transmitted waveform to the towfish. This digital signal is recorded on a logger channel using a 500 Hz sampling rate in each towfish. The digital signal can be used to correct for clock drift on the phase data recorded on each instrument.

The timing of the emitted signal can also be compared to the digital signal directly using the data recorded on the transmitter towfish. This transmitter towfish is a novel design and the recorded data can be used to capture zero-time offsets or any timing errors with the emitted signal. The transmitter towfish both emits a current-controlled waveform on a 2 meter rigid dipole, and also records this same signal on a 1 meter vertical dipole using stainless steel electrodes. This means that the transmitter towfish directly records the emitted signal as well as the digital signal corresponding to the transmitted waveform. As the field is being recorded at the source and on the same internal clock, the transmitter towfish can capture any timing errors

between the emitted source and the digital signal. Generally, drift rates from the Seascan clocks appear to be linear, but there is a timing offset upon starting transmission. Accurate phase data can be achieved with a measurement of both the timing offset (a fraction of a sample in most cases) and the linear drift rates.
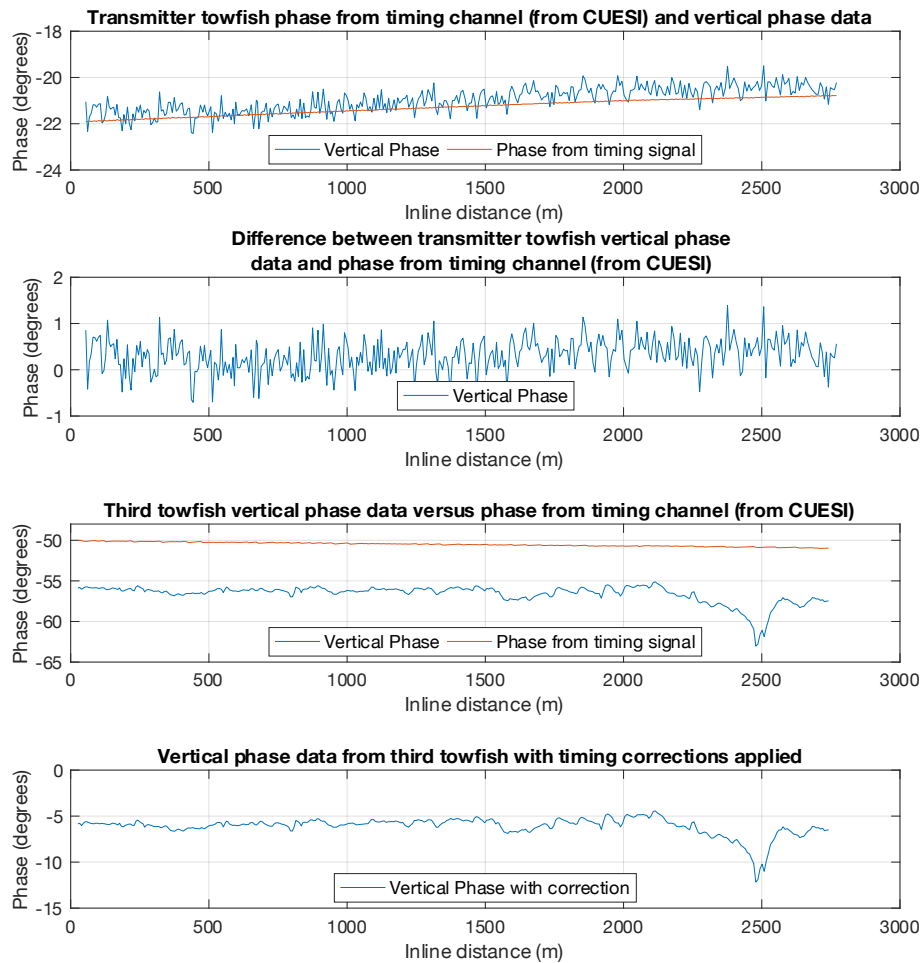


Fig. 6.5: All phase data presented in these panels are from a 25 Hz frequency signal. Top panel is a plot of the phase from the digital timing pulse recorded on the fifth channel of the first towfish and the phase from the recorded vertical electric field data. Both digital timing phase and electric field phase appear to drift as both sets of data are time stamped with an internal clock which drifts at a rate of approximately 2 miliseconds per day. Both sets of phase data have a zero-time offset of 22 degrees consistent with the 0.0024 second time tag recorded from the internal clock in CUESI. The second panel is a plot of the difference between the digital timing phase and electric field phase which is generally 0.5 degrees, capturing the timing offset of 0.055 miliseconds ( a fraction of a sample) beteen the two sets of phase data. The third panel plots the digital timing phase and electric field phase from the third towfish in the array. The bottom panel is the electric field phase from the third towfish corrected both from the internal clock drift on this instrument and from the timing offset from CUESI (shown in the second panel).

109

As an example, Fig. 6.5 shows the 25Hz phase data and phase corrections using both the linear drift correction from internal clock and static shift correction captured with the transmitter towfish. In Fig. 6.5, the top panel is of the phase from the digital timing channel and phase from the vertical dipole. Phase drift, from the internal clock, is generally linear; however, a zero-time offset of around -22 degrees is noted for both the digital timing channel phase and vertical dipole phase which is consistent with the time tag of 0.0024 seconds recorded from the internal clock in CUESI before deployment. The second panel of Fig. 6.5 shows the difference between the phase from the digital timing channel and vertical dipole. Here, the phase from the vertical dipole is shifted to be 0.5 degrees higher than the phase from digital timing channel. This timing shift is the equivalent to a timing error of 0.055 milliseconds on a 25Hz signal which is a fraction of sample and indicates a that the digital timing signal arrived just after transmission began. The phase from the vertical dipole and digital timing channel for the last towfish in the array are plotted in the third panel where linear drift from the clock can be observed. Finally, the last panel plots the corrected phase for the third towfish. The correction included the individual clock drift from the third towfish as well as the 0.5 degree shift from the timing lag of the digital signal. Using these correction values, the corrected phase for the third towfish is in good agreement with the predicted response generated from forward models.

## 6.5 System performance and navigation

In the conductive marine environment, electromagnetic signals attenuate quickly. Thus, the received signal is dependent on the distance between the electromagnetic source, receivers, and the seafloor. If this distance is overestimated, the resistivity of the seafloor will be inferred as

more resistive than it is. To reduce error in the models, the depth of the array and the bathymetry must be well constrained. Additionally, navigational errors can lead to large errors in CSEM data with short source-receiver offsets (e.g., Myer et al., 2012), so navigational data such as pitch and heading of the instruments should be captured and included in data processing.

CUESI and all three of the towfish measure depth to a fraction of a meter in 1 second increments using pressure sensors. This provides depth data for each instrument, but the height of the seafloor also must be established. Depth to the seafloor is measured both by CUESI and by the vessel. The vessel typically measures the full water depth, while CUESI measures its current distance to the seafloor using an altimeter with centimeter accuracy. The altimeter data and pressure data from CUESI can be combined into a depth profile of each survey line. Assuming fixed offsets, the altitude of each towfish is calculated. Fig. 6.4 shows the altitude of CUESI system above the seafloor and the overall water depth. Generally, the tow height of the array appears to be within 1 to 3 meters of the seafloor with a few exceptions when more irregular seafloor bathymetry is encountered. The altitude of the last towfish in the array tended to be slightly greater with distances between 2 to 4 meters of the seafloor. Overall, the array functioned as designed, flying within 5 meters of the seafloor for the duration of the surveys.

The location of the CUESI array is not directly measured during the survey. Thus, the location of the array is calculated using the layback distance and heading of the vessel and instruments. Layback can be determined by first recording the length of cable out to CUESI during the survey. The length of cable will fluctuate depending on tow speeds and water depth so measurements of the length are recorded every 5 minutes during surveying. Using trigonometry, the approximate location of the array can be determined with cable out, but more accuracy can be achieved by comparing depth profiles made from the vessel versus CUESI. If the array

tracked behind the vessel, the layback is the distance the vessel depth profile must be moved

laterally to match the CUESI bathymetric profile while still considering cable out. With this

method and with heading data, a location for each towfish can be generated.
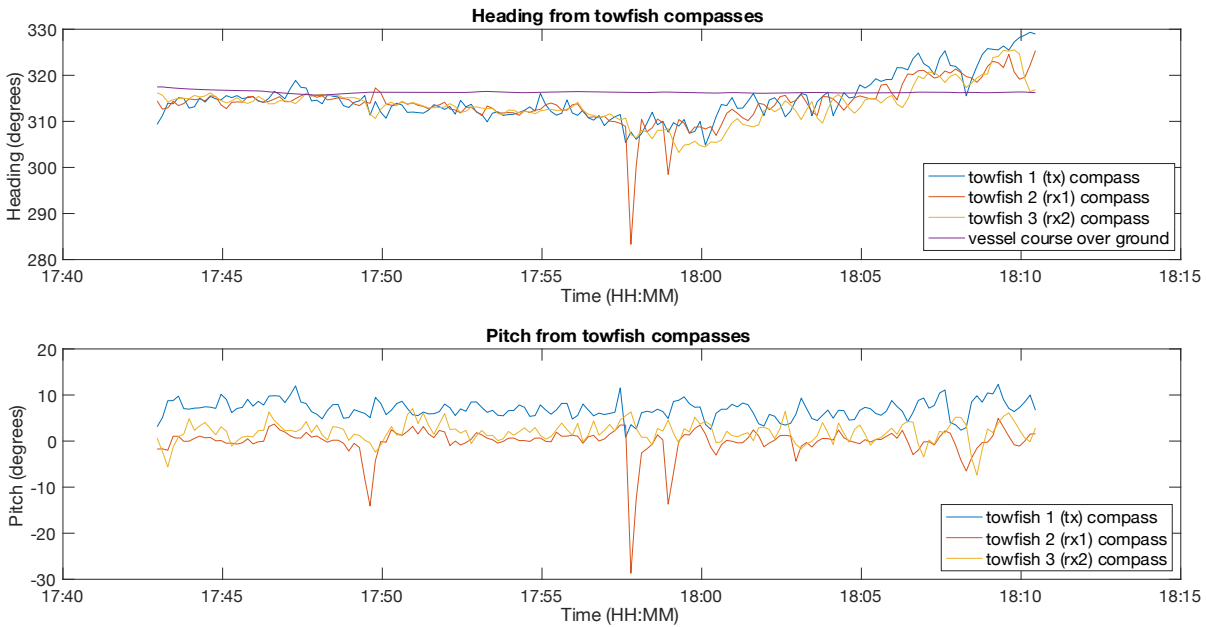


Fig. 6.6: Top panel shows the heading recorded on the external compasses mounted to each towfish and the course over ground of the vessel The three towfish appear to have similar headings indicating that the array towed in a straight line; however the heading of the towfish compared to the vessel's course over ground indicates that the array did not track directly behind the vessel, but instead crabbed through the water possibly due to currents near the seafloor. The bottom panel is pitch recorded on the external compasses of each towfish. Towfish 2 and 3 have a pitch near 0 inidcating that these two towfish maintained a horizontal orientation during towing except for in a few locations where snagging may have occurred on the line or tow speeds may have been inconsistent. The first towfish has a positive pitch (front end up) throughout the survey which may have been from CUESI pulling the front of this towfish upward during towing.

Crossline distances along the array are not measured and are more difficult to determine.

However, if all instruments record similar headings, the array is inferred to have tracked in a line

and a crossline distance of zero is assumed. It is likely that this assumption does not fully

represent the reality of towing behavior and is therefore a potential source of error in the models.

The top panel of Fig 6 is the heading data for each towfish recorded on external compasses as

well as the course over ground of the vessel. The course over ground of the vessel does not align with the towfish headings which indicates that the array may have been crabbing through the water. However, as the transmitter heading is comparable to the receiver headings, the array appears to be towing in a straight line. When heading is irregular, such as at the approximately 17:57 in Fig. 6.6, data associated with this point in time are excluded from the final models. Pitch of the instruments also effects the amplitude and phase of the electric field. Thus, pitch data are recorded and included in the models to reduce the effects of navigational error. The bottom panel of Fig. 6.6 is the pitch of the towfish. Generally, the two receiver towfish (2 and 3) have a pitch around zero with brief periods of irregularity. The transmitter towfish appears to have a consistently positive pitch, aft down and front facing upward, configuration during towing. This pitch may be from CUESI pulling the front of the transmitter towfish upward slightly as it is at a higher altitude than the rest of the array.

## 6.6 Case Studies

During its development, the CUESI system has been tested in several areas offshore Southern California. The case studies presented here are limited to the two regions highlighted in Fig. 6.7. Coal Oil Point is a known location of multiple marine hydrocarbon seeps. Hydrocarbons are highly resistive making this region an attractive area to initially test the sensitivity of the CUESI system to significant changes in resistivity within the seafloor. Additionally, this region has been previously surveyed using the more established surface-towed CSEM system of Sherman et al. (2017) so comparison between datasets is possible.

The northern Channel Islands were chosen as a test site for the CUESI system because sediment core, acoustic reflection, and CSEM data are available in this region. Using the

sediment core data, the CUESI system was tested for its ability to resolve porosity changes within the shallow seafloor. The acoustic reflection profiles provide context for the core locations and lateral constraints on the local geology.
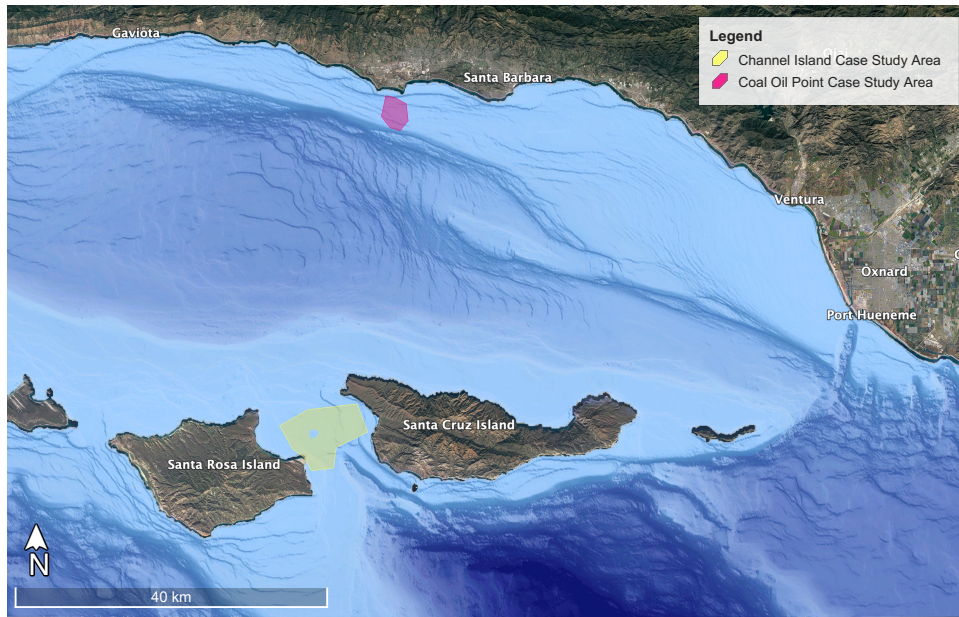


Fig. 6.7: Case study survey areas offshore Southern California. The pink region marks the approximate boundary of the Coal Oil Point seep field south of Santa Barbara and the yellow polygon marks the boundary of the study area between Santa Rosa Island and Santa Cruz Island within Channel Islands National Marine Sancturary.

### 6.6.1 Sensitivity to Seafloor Resistors – Coal Oil Point

An initial test of the CUESI system was conducted in May of 2021 and targeted the Coal Oil Point seep field. This case study aimed to test how the system functions, tows through the water, and if the system is sensitive to a known resistive feature. This test occurred during the initial development of the CUESI system so there were few navigational constraints and sparse data collection.

The Coal Oil Seep field was previously imaged with a surface-towed CSEM system (King et al., 2022) so the locations of resistive features were well defined prior to the CUESI survey. In Fig. 6.8, amplitude data from a CUESI survey are compared to a resistivity profile of an active seep. In this image, the red feature at the seafloor is interpreted as hydrocarbons on the seafloor. The blues are indicative of typical marine sediment which has a resistivity between 1 to 2 $\Omega$m. The top panel of Fig. 6.8 is the amplitude of the inline electric field response stacked in 10 second windows from the third towfish. Electric fields are attenuated in conductive mediums which results in a decrease in the amplitude data; conversely resistive features preserve electric fields resulting in higher amplitude responses. Therefore, the amplitude of the response data is expected to be higher over the resistive hydrocarbons compared to over the more conductive marine sediment.

The amplitude of the inline response data recorded with the CUESI system is as predicted, with higher amplitude responses recorded over the seep field compared to the more conductive surrounding area. The correlation between the amplitude response and the location of the seafloor resistors indicates general functionality of the system toward detecting changes in resistivity. Unfortunately, there were inadequate navigational data collected from this survey to create pseudosections, but the overall response of the system to the seafloor was promising and led to further development.
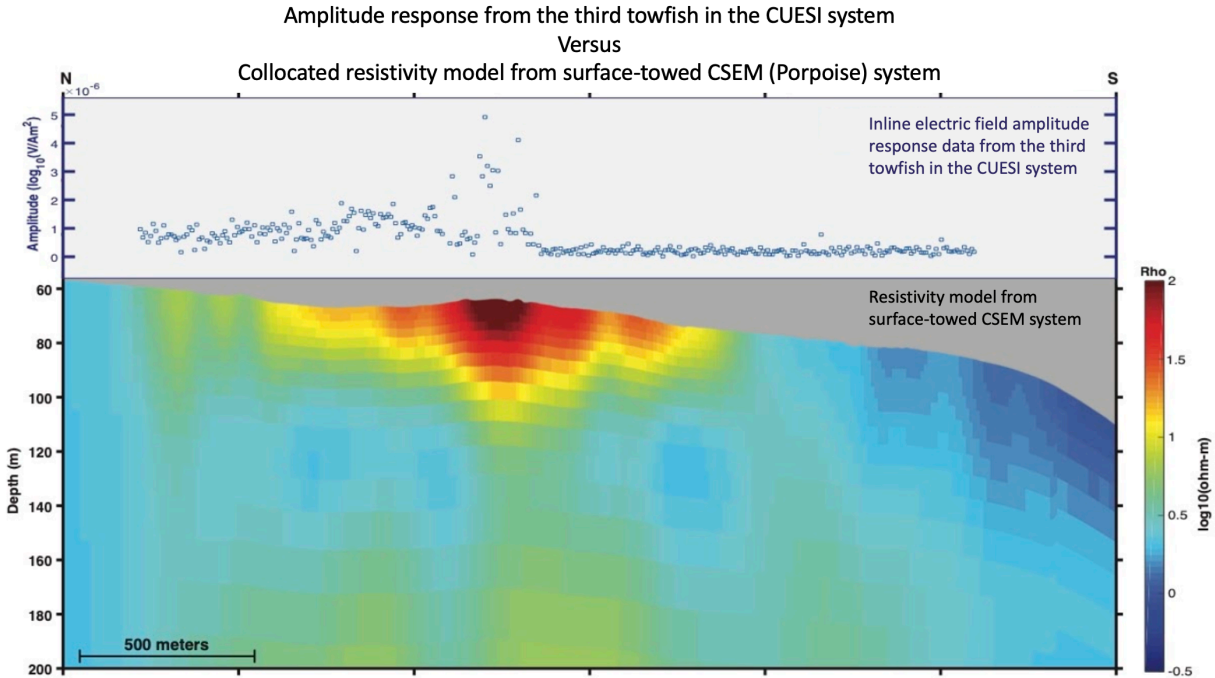
Fig. 6.8: Comparison between amplitude data from the CUESI system and a resistivity profile generated from surface-towed CSEM data over an active seep within the Coal Oil Point seep field. The top panel is the inline amplitude data from the third towfish in the CUESI array. The bottom panel is a collocated resistivity profile from King et al. (2022).

### 6.6.2 Comparison to core data – Channel Islands National Park

Following the initial functionality tests of the CUESI system, the array was moved to northern Channel Islands National Marine Sanctuary. Here, the CUESI system was used to survey several areas where sediment cores were collected on a previous cruise. Due to sea-conditions, surveying time was limited and the survey areas were reduced to a few locations within the survey area mapped in Fig. 6.7. During the survey, a 25 Hz, 2.5 Amp square wave was transmitted on a 2 meter horizontal dipole.

The inline electric time series measured on the second and third towfish during these surveys was Fourier transformed and stacked into 10 second windows. Stacking the data

provides error estimates as well as increasing the signal to noise ratio. The first and third

harmonics from the transmitted 25 Hz square wave were included in the processing.

From these surveys, pseudosections were generated using the inline electric field data

from the second and third towfish. Pseudosections use the navigation data collected from each

towfish and the water depth and conductivity collected by CUESI during the survey. Forward

solutions are calculated from 1D models that include the water depth and seawater conductivity

underlain by halfspaces ranging from 0.1 to 1000 $\Omega$m. Apparent resistivity values are obtained

by interpolating between the forward solutions and each value of the stacked amplitude data. The

general depth of each apparent resistivity value is calculated from the approximate skin depth of

each frequency used and the source receiver offset. Each apparent resistivity value is then

represented by a pixel with location data and these pixels are combined to create pseudosections.

Pseudosections are good indicators of lateral changes in resistivity, but have limited ability to

determine actual depths to features (Weitemeyer et al., 2006).

Pseudosections generated from data collected over two core locations are shown in Fig.

6.9. Here, the top pseudosection was created from data collected while targeting sediment core

CI-VC-B4. This sediment core was initially collected to target a mound identified in acoustic

reflection data shown in Fig. 6.10. The core is more porous than the surrounding sediment cores

presumable because it contains abundant intact and fragmented shells which have created voids

in the sediment. To test the ability of the CUESI system to detect changes in seafloor porosity,

the apparent resistivity values must first be converted into porosity values. Typically, resistivity

and pore fluids are related using Archie's law which is given by the equation:

$$\rho_o = \rho_f \phi^{-m} \tag{2}$$

where $\rho_o$ is the bulk resistivity of the water-saturated material, $\rho_f$ is the resistivity of the pore

fluids, $\phi$ is the porosity of the material, and $m$ is the cementation factor. Generally, the

cementation factor is a measure of how the resistivity of a rock changes with permeability,

assuming the pore fluids are more conductive than the grains. The original form of this equation

(2) does not account for grain texture, and thereby could underestimate porosity by up to 20

percent (Glover, 2016; Winsauer et al., 1952). Therefore, Winsauer et al. (1952) introduced the

'tortuosity' or 'lithology' parameter, $a$, to Archie's law which has the form:

$$\rho_o = a\rho_f\phi^{-m} \qquad (3)$$

In this study, the Winsauer et al.'s (1952) Humble formula, which is commonly used for

unconsolidated sediments or loose formations such as marine sands (El-khatib, 1997), was used.

The Humble formula, named after Humble Oil where it was first created, uses a cementation

exponent of 2.15 and a tortuosity factor of 0.62. Using this formula and data collected by the

CUESI system (see upper right panel of Fig. 6.9), the apparent porosity of sediment collocated

with core CI-VC-B4 was calculated to be 68.8 percent, consistent with the bulk porosity of the

core which was 69%.

Unfortunately, due to strong currents between the islands, the CUESI profile could not be

collocated with the acoustic reflection profile shown in Fig. 6.10. However, the mound

associated with core CI-VC-B4 is the intersection point of the two profiles (the CUESI profile

has a 112 degree heading and the acoustic reflection profile has a 52 degree heading) and is

apparent in both profiles. The mound in Fig. 6.10 appears to be 45 meter-wide discrete feature

within marine sands. In the top panel of Fig. 6.9, a 45 to 50 meter-wide discrete high-conductivity feature is observed to be collocated with the mound, showing good agreement between acoustic reflection data and the apparent resistivity profile.
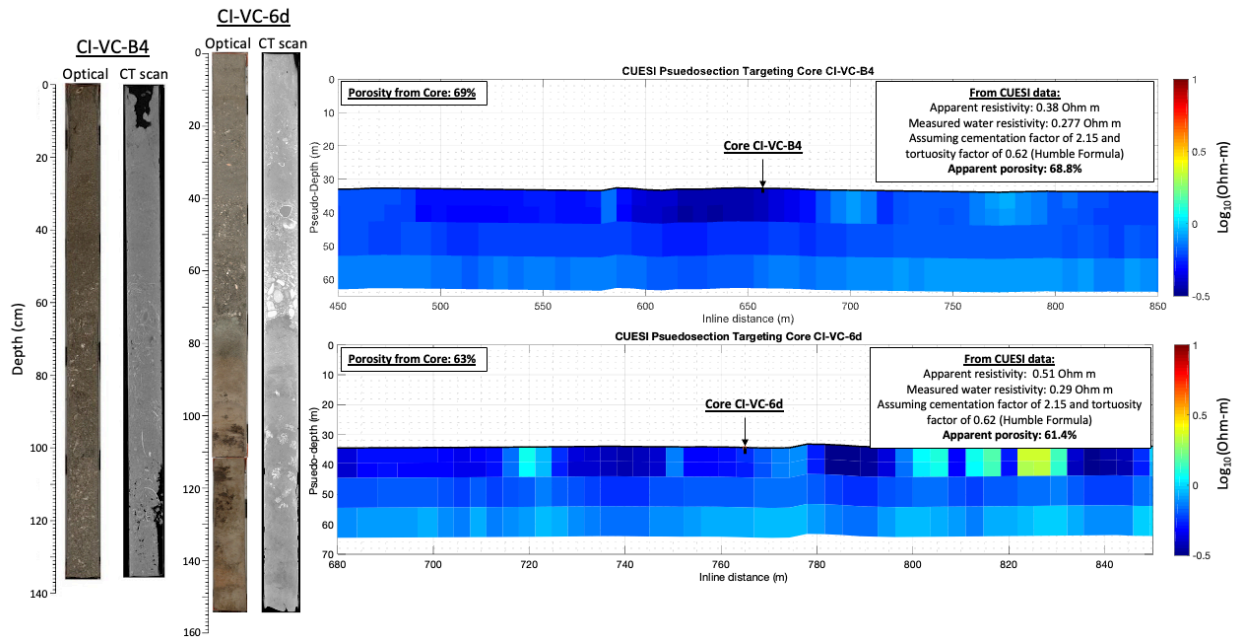


Fig. 6.9: The top profile is a pseudosection generated from a CUESI survey targeting core CI-VC-B4. The CI-VC-B4 core is from a mound-like feature within marine sediment as shown in Fig. 6.10. The bottom profile is a pseudosection generated from a CUESI survey targeting core CI-VC-6d. The CI-VC-6d core contains lithics and layers of silt resulting in a lower overall porosity value compared to the surrounding sediment. Photos and CT scans of both cores are shown to the left.

The bottom panel of Fig. 6.9 is a pseudosection created from data collected while targeting core CI-VC-6d. This core is predominately comprised of sand, fragmented shells, lithics, and thin layers of silt resulting in moderately porous sediment. Again, using the Humble formula and data from the CUESI system (see Fig. 6.9), the apparent porosity of the seafloor collocated with the core was calculated to be 61.4% whereas the bulk porosity of the core was 63%.
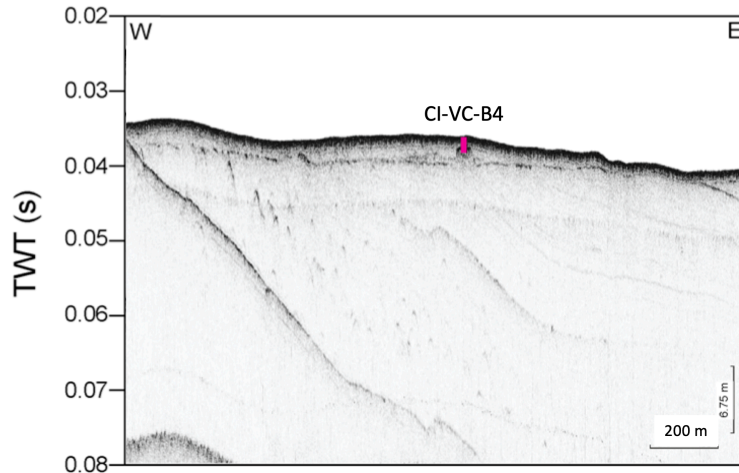
Fig. 6.10: High-resolution Chirp subbottom profile over core CI-VC-B4 collected in 2016. Courtesy of Jillian Maloney.

The agreement between apparent porosity values from the CUESI system and the core porosity indicates that the CUESI system is sensitive to the porosity of the shallow subseafloor. However, this test was extremely limited and the CUESI system will need to be tested over more core locations and over a variety of seafloor types before determining the overall sensitivity of the system.

### 6.6.3 Comparison with existing CSEM systems – Channel Islands National Park

The final case study presented here uses the most current version of the CUESI system, which includes more navigational constraints and data with a higher signal to noise ratio than prior surveys. These data were included in inversions and used for direct comparison of resistivity profiles created using an existing CSEM system and the CUESI system.

#### 6.6.3.1 CUESI and Surface-Towed Data Processing and Model Design

The CUESI system was used to resurvey a profile mapped in Fig. 6.11 where data were previously collected using a surface-towed CSEM system, known as the porpoise system. In this

profile, the porpoise system previously passed over a known fault and identified several resistive features. For the CUESI survey discussed here, the transmitter towfish emitted a 25 Hz 2.8 Amp square wave on a 2 meter horizontal dipole. The CUESI system was towed within 1 to 4 meters of the seafloor at 1 to 2 knots for 45 minutes resulting in data collected over ~2350 meters of seafloor. During this survey, the camera mounted to the CUESI frame collected images of the seafloor every 3 seconds which are shown in Fig. 6.12.

As described in the previous section, amplitude and phase of the CSEM response functions were extracted from the raw time-series data on the second and third towfish using the methods detailed by Myer et al. (2011). To increase the signal-to-noise ratio, the resulting transfer function estimates were stacked using an arithmetic mean to obtain transfer function estimates every 10 seconds along with error estimates. As the tow rates of the survey ranged between 1 and 2 knots, each transfer function estimate from this level of stacking resulted in one sample per towfish per frequency every 5 to 10 meters along the survey line. This approach yielded high quality amplitude and phase response data for the last two towfish as a function of position and frequency.

Navigational error has a greater effect on amplitude data than phase data and this effect is worse at short source-receiver offsets. Thus, only phase data from the second towfish, a 10 meter source-receiver offset, were included in the inversion whereas both amplitude and phase data from the third receiver, a 30 meter source-receiver offset, were included in the inversion. As the harmonics of a square wave fall off geometrically, only data from the first and third harmonics (25 Hz and 75 Hz) were used. Using these constraints, the profile from the CUESI survey shown in Fig. 6.12 has a total of 1446 CSEM data and these data were assigned a 5 percent error floor to

account for navigational uncertainties before being included in the inversion as finite-length dipoles.
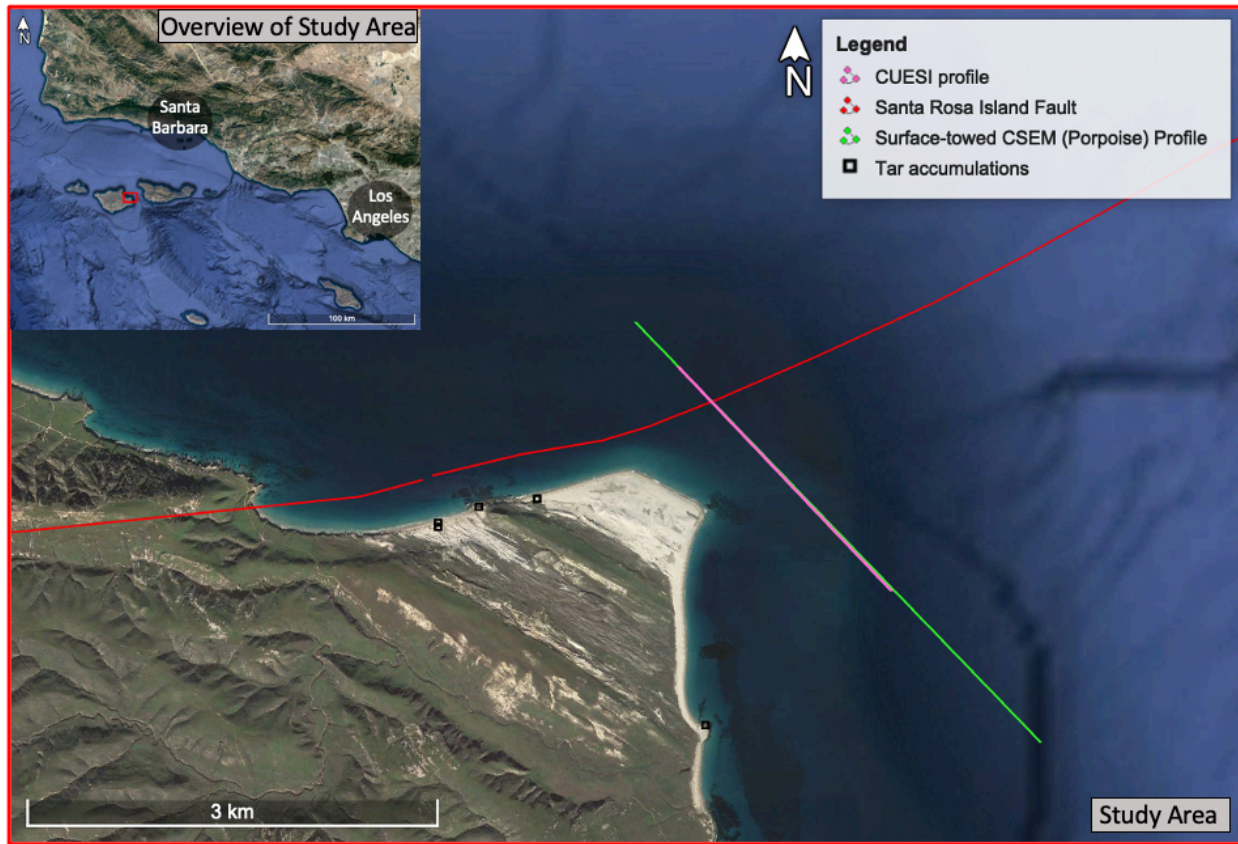


Fig. 6.11: Location of the resistivity profiles presented in Fig. 6.12. The green line marks the location of the surface-towed CSEM survey and the pink line marks the location of the CUESI survey line. The red lines represent the surface trace of the Santa Rosa Island Fault which crosses through both surveys and is marked with dashed red line in Fig. 6.12. Black squares mark the locations of documented tar accumulations on the beaches from Lorenson et al. (2009).

The modeling software used in this study is the publicly available, goal-oriented, adaptive, finite-element two-dimensional (2D) MARE2DEM inversion and modeling code of Key (2016). This code uses Occam's Inversion, a method that regularizes the inversion to the smoothest resistivity model that fits the data to a specified misfit (Constable et al., 1987). The starting model included the seawater as a fixed parameter, using conductivity data collected by CUESI. The bathymetry profile included in the starting model was generated by combining the

depth and altimeter data, also collected by CUESI. This bathymetry profile was checked with depth data collected by the vessel and with the depth profile generated using an altimeter from the prior surface-towed CSEM survey, as a test of the functionality of the CUESI depth sensor and altimeter. Using this model structure, the free inversion regions were reduced to the area below the seafloor and set to a uniform starting resistivity of 1 $\Omega$m. An inversion parameter grid was constructed using 10-meter-wide quadrilateral cells that increased in height with depth to mimic the loss of resolution of the EM method. Intrinsic to the adaptive nature of the MARE2DEM code, the computation mesh was allowed to refine where necessary to produce accurate responses. The resistivity inversion was allowed to run until the final inversion model response converged to a root-mean-square misfit of 1. The final resistive inversion, labeled 'CUESI Profile', in shown in Fig. 6.12.

The surface-towed CSEM data were collected using the CSEM system of Sherman et al. (2017) in January 2019, nearly two years prior to the CUESI data in January of 2019. The surface-towed survey is described in detail in King et al. (2022). During the surface-towed CSEM survey, the transmitter output was a 2 Hz, 30-amp, current-controlled waveform-D of Myer et al. (2011) on a 10-meter antenna. The array was made up of 4 receivers spaced 100 meters apart for a total array length of 400 meters. Only the second and third receivers in the array (200- and 300-meter source-receiver offsets) collected data on the survey line described here.

The surface-towed CSEM data were processed using the method described above and by Myer et al. (2011); however stacking windows were increased to 30 seconds to account for the rough wave conditions encountered during this survey. Additionally, waveform-D results in a broader range of high amplitude harmonics, and so amplitude and phase data for the 3rd, 7th,

and 13th harmonics (6 Hz, 14 Hz, and 26 Hz) were included in the inversion for both receivers. The amplitude data were subjected to a two-percent error floor and the phase data were subjected to a one-percent error floor before being included in the model as finite-length dipoles. The surface-towed CSEM array was towed at a rate of 3 to 4 knots which when combined with 30 second stacking windows results in one sample per receiver per frequency every 45 to 60 meters along the survey line. The profile from the surface-towed CSEM, shown and labeled 'Porpoise Profile' in Fig. 6.12, has a total of 752 CSEM data.

The MARE2DEM inversion code was used to generate inversions for the surface-towed CSEM survey. Here, the starting models included seawater as a fixed parameter, using conductivity data collected by a separate towed instrument in the porpoise array and available bathymetric data. The free inversion region below the seafloor was set to a uniform starting resistivity of 1 Ωm and parameterized using 20-meter-wide quadrilateral cells that increased in height with depth. The resistivity inversion was allowed to run until the final resistivity inversion converged to a root-mean-square misfit of 1. The final resistive inversion, labeled 'Porpoise Profile', is shown in Fig. 6.12. The extent of the CUESI profile is outlined with a black box and overlain on the Porpoise Profile.
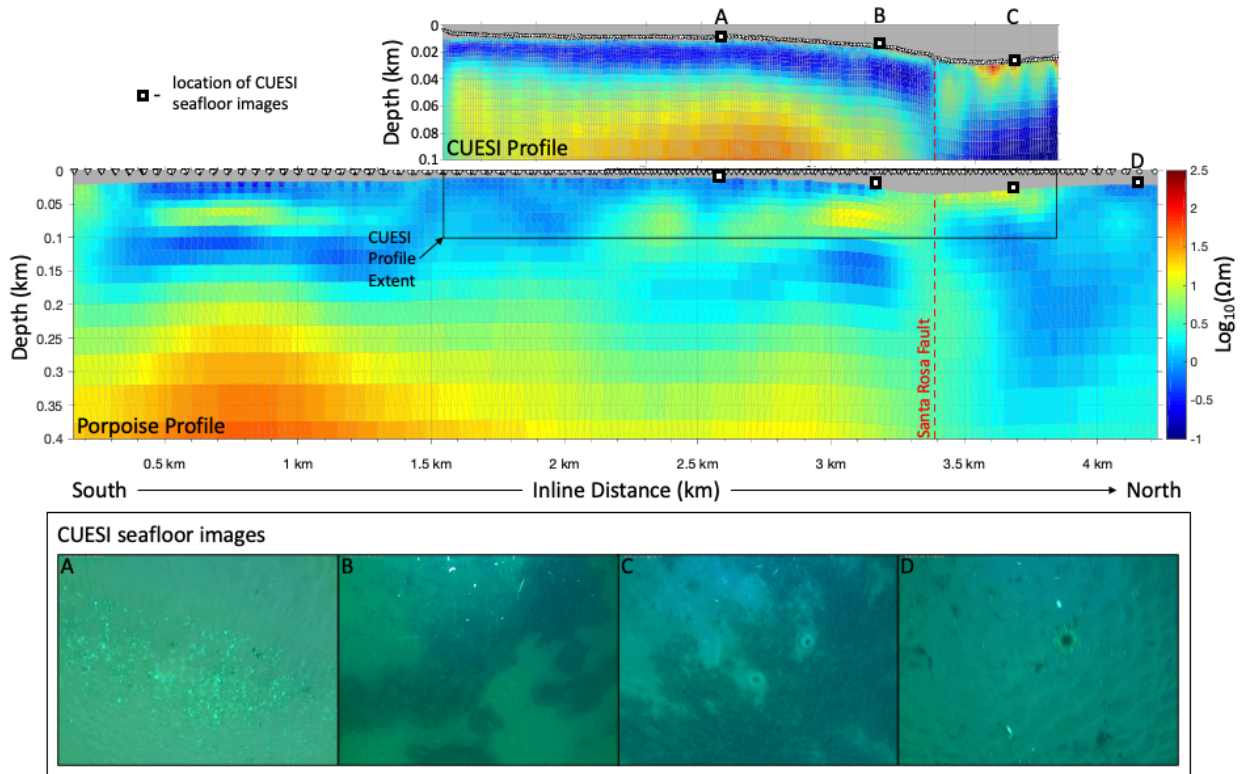
Fig. 6.12: Resistivity models from the CUESI survey and surface-towed CSEM (Porpoise) survey offshore Santa Rosa Island. The top panel, labeled 'CUESI Profile', is a resistivity model from the survey line mapped as a pink line in Fig. 6.11. The location of the CUESI profile is marked by a black box on the middle panel. The middle panel, labeled 'Porpoise Profile', is a resistivity model from the surface-towed CSEM survey mapped as a green line in Fig. 6.11. Warm colors indicate high resistivity and cool colors indicate conductors in both resistivity profiles. The black and white circles and triangles in both profiles mark the locations of the transmitters and receivers used in the modeling code. The black squares on both the top and middle panels are the locations of the photos captured by the CUESI system and shown in the bottom panel.

## 6.6.3.2 CUESI and Surface-towed CSEM System Model Comparison and Interpretation

The two resistivity models shown in Fig. 6.12 are in good agreement where the models are co-located. The CUESI system resulted in a higher resolution model of the subseafloor resistivity due to shorter source-receiver offsets and higher source frequencies. This survey design resulted in greater sensitivity to changes in the immediate seafloor resistivity, but with the trade-off of reducing the depth of sensitivity compared to the Porpoise system. The depth of

sensitivity with the Porpoise system used in this study is around 400 meters below sea level whereas the CUESI system shows a significant reduction in sensitivity (sensitivity value of -3.5 $\log_{10}(S/m)/m^2$ using the MARE2DEM code) between 80 to 100 meters below sea level (60 to 90 meters below the seafloor). This depth of sensitivity for the CUESI system corresponds to approximately one skin depth in a 1 $\Omega$m medium. The depth of sensitivity achieved with the CUESI system is deeper than what is expected from a towed CSEM array with a maximum source-receiver offset of 40 meters. The deeper depth of inference obtained with the CUESI system could be explained by the high frequencies used in the survey possibly resulting in a signal limited by parametric aspects of EM propagation instead of geometric limitations, the increased data density achieved with the CUESI system, and/or the placement of the transmitter and receivers near the seafloor.

The higher resolution of the CUESI model, is evident in the better defined fault trace of the Santa Rosa Island Fault in the CUESI profile compared to the Porpoise profile. In the CUESI profile, the fault clearly laterally separates a more conductive material underlain by a resistor from a resistor underlain by a conductor to the north. This general resistive structure is resolved, but smoothed, in the Porpoise profile. At depth the fault appears to be collocated with a vertical resistor in the Porpoise profile, possibly indicating resistive fluid migration, such as freshwater or hydrocarbons, up the fault. Historically, accumulations of hydrocarbons have been documented on the nearby beaches on Santa Rosa Island (Lorenson et al., 2009) so the resistors along the fault could be interpreted to be tar.

Fig. 6.13: Photo of tar accumulation on the seafloor offshore Angola. Image from Jones et al. (2014).

This interpretation is supported by the photos captured by the CUESI system during the survey. The images captured during the survey are in the bottom panel of Fig. 6.12 and the locations are marked with black squares on both the CUESI and Porpoise profiles. In photo A, the seafloor appears to be made up of sand with several sparce accumulations of fractured shells. Here, the seafloor resistivity in the CUESI profile is approximately 1 Ωm, signifying typical marine sediment with saline pore fluids. The location of photo B marks the southern edge of a 10 Ωm resistor on the seafloor of the CUESI profile and is the first occurrence of dark material in the photo series along the tow line. Photo B appears to capture a seafloor character similar to Fig. 6.13, which is a photo of confirmed asphalt/tar mounds offshore Angola. The resistivity and appearance of the seafloor at the location of photo B indicate the presence of tar accumulations on the seafloor. The Porpoise profile also includes a resistive feature at the seafloor in this approximate location.

Travelling farther north along the towlines, photo C is located above a strong resistor (>30 Ωm) in the CUESI profile. Photo C captures a dark patchy seafloor environment and this

photo is consistent with other photos taken between 3.5 km to 3.7 km along the towline, the approximate span of the seafloor resistor. The seafloor along this section of the towline may be seafloor sediments with hydrocarbon coatings or seafloor sediment saturated with hydrocarbons. This type of hydrocarbon accumulation is associated with hydrocarbon seeps that may become temporarily sealed or slowed due to changes in sea state or reservoir pressure (Leifer, 2019). Both the CUESI and Porpoise profiles resolve a strong resistor at the seafloor collocated with the regions of darkly colored seafloors captured in the photos. The seafloor resistor extends from the photo B location until approximately 3.85 km along the towline where the seafloor resumes a ~1 Ωm resistivity in the Porpoise profile and a seafloor character shifts to resemble the seafloor captured in Photo D.

The photo observations and resistivity profiles indicate that this survey imaged a previously unidentified hydrocarbon seep at the seafloor that is fed from a deeper source, resolved as a resistor ~250 to 350 meters below sea level in the Porpoise profiles, along the Santa Rosa Island Fault.

## 6.7 Conclusion

Through a series of tests comparing the CUESI system to profiles of known resistors and sediment core data, the new system appears to be in good agreement with existing datasets. The results from these tests indicate that the CUESI system is sensitive to changes in porosity in the upper few meters of seafloor. Additionally, when compared to the surface-towed CSEM system of Sherman et al. (2017), higher resolution resistivity profiles of the shallow subseafloor are achieved using the CUESI system with the tradeoff of a significant decrease in the depth of

investigation. More tests of the CUESI system over a variety of seafloor types and targets are necessary to better understand the sensitivity and resolution available with the new system.

## 6.8 Acknowledgements

## 6.8 References:

Cheesman, S., Law, L., & St Louis, B. (1993). A porosity mapping survey in Hecate Strait using a seafloor electro-magnetic profiling system. In *Marine Geology* (Vol. 10).

Constable, S. C., Parker, R. L., & Constable, C. G. (1987). Occam' s inversion: A practical algorithm for generating smooth models from electromagnetic sounding data. *GEOPHYSICS*, *52*(3), 289–300.

Constable, S., Kannberg, P. K., & Weitemeyer, K. (2016). Vulcan: A deep-towed CSEM receiver. *Geochemistry, Geophysics, Geosystems*, *17*(3), 1042–1064. https://doi.org/10.1002/2015GC006174

El-khatib, N. (1997, March 15). A Fast and Accurate Method for Parameter Estimation of Archie Saturation Equation. *All Days*. https://doi.org/10.2118/37744-MS

Evans, R. L. (2001). Measuring the shallow porosity structure of sediments on the continental shelf: A comparison of an electromagnetic approach with cores and acoustic backscatter. *Journal of Geophysical Research*, *106*(C11), 27047–27060.

Evans, R. L. (2007). Using CSEM techniques to map the shallow section of seafloor: From the coastline to the edges of the continental slope. *Geophysics*, *72*(2). https://doi.org/10.1190/1.2434798

Evans, R. L., Law, L., St Louis, B., Cheesman, S., & Sananikone, K. (1999). The shallow porosity structure of the Eel shelf, northern California: results of a towed electromagnetic survey. In *Marine Geology* (Vol. 154).

Glover, P. W. J. (2016). Archie's law - A reappraisal. *Solid Earth*, *7*(4), 1157–1169. https://doi.org/10.5194/se-7-1157-2016

Jones, D. O. B., Walls, A., Clare, M., Fiske, M. S., Weiland, R. J., O'Brien, R., & Touzel, D. F. (2014). Asphalt mounds and associated biota on the Angolan margin. *Deep-Sea Research Part I: Oceanographic Research Papers*, *94*, 124–136. https://doi.org/10.1016/j.dsr.2014.08.010

Key, K. (2016). MARE2DEM: A 2-D inversion code for controlled-source electromagnetic and magnetotelluric data. *Geophysical Journal International*, *207*(1), 571–588. https://doi.org/10.1093/gji/ggw290

King, R. B., Constable, S., & Maloney, J. M. (2022). A case study in controlled source electromagnetism: Near seabed hydrocarbon seep systems of Coal Oil Point, California, USA. *Marine and Petroleum Geology*, *139*. https://doi.org/10.1016/j.marpetgeo.2022.105636

Leifer, I. (2019). A Synthesis Review of Emissions and Fates for the Coal Oil Point Marine Hydrocarbon Seep Field and California Marine Seepage. In *Geofluids* (Vol. 2019). Hindawi Limited. https://doi.org/10.1155/2019/4724587

Lorenson, T. D., Hostettler, F. D., Rosenbauer, R. J., Peters, K. E., Dougherty, J. A., Kvenvolden, K. A., Gutmacher, C. E., Wong, F. L., & Normark, W. R. (2009). Natural Offshore Oil Seepage and Related Tarball Accumulation on the California Coastline; Santa Barbara Channel and the Southern Santa Maria Basin; source identification and inventory. *US Geological Survey Open-File Report*, *1225*, 2009–2030.

Micallef, A., Person, M., Haroon, A., Weymer, B. A., Jegen, M., Schwalenberg, K., Faghih, Z., Duan, S., Cohen, D., Mountjoy, J. J., Woelz, S., Gable, C. W., Averes, T., & Kumar Tiwari, A. (2020). 3D characterization and quantification of an offshore freshened groundwater system in the Canterbury Bight. *Nature Communications*, *11*(1). https://doi.org/10.1038/s41467-020-14770-7

Myer, D., Constable, S., & Key, K. (2011). Broad-band waveforms and robust processing for marine CSEM surveys. *Geophysical Journal International*, *184*(2), 689–698. https://doi.org/10.1111/j.1365-246X.2010.04887.x

Myer, D., Constable, S., Key, K., Glinsky, M. E., & Liu, G. (2012). Marine CSEM of the Scarborough gas field, Part 1: Experimental design and data uncertainty. *Geophysics*, *77*(4). https://doi.org/10.1190/geo2011-0380.1

Schwalenberg, K., Haeckel, M., Poort, J., & Jegen, M. (2010). Evaluation of gas hydrate deposits in an active seep area using marine controlled source electromagnetics: Results from Opouawe Bank, Hikurangi Margin, New Zealand. *Marine Geology*, *272*(1–4), 79–88. https://doi.org/10.1016/j.margeo.2009.07.006

Schwalenberg, K., Willoughby, E., Mir, R., & Edwards, R. N. (2005). Marine gas hydrate electromagnetic signatures in Cascadia and their correlation with seismic blank zones. *First Break*, *23*(4).

Sheehan, E., Rodriguez-Rodriguez, D., Foster, N., Nancollas, S., Cousens, S., Holmes, L., Attrill, M., Pettifer, E., Jones, I., Vaz, S., Facq, J.-V., & Germain, G. (2014). A comparative study of towed underwater video methodology to monitor benthic habitats in Marine Protected Areas. *Ifremer, Sussex IFCA and Marine Institute for the Protected Area Network Across the Channel Ecosystem (PANACHE) Project*.

Sherman, D., Kannberg, P., & Constable, S. (2017). Surface towed electromagnetic system for mapping of subsea Arctic permafrost. *Earth and Planetary Science Letters*, *460*, 97–104. https://doi.org/10.1016/j.epsl.2016.12.002

Weitemeyer, K. A., Constable, S. C., Key, K. W., & Behrens, J. P. (2006). First results from a marine controlled-source electromagnetic survey to detect gas hydrates offshore Oregon. *Geophysical Research Letters*, *33*(3). https://doi.org/10.1029/2005GL024896

Weitemeyer, K., & Constable, S. (2010). Mapping shallow geology and gas hydrate with marine CSEM surveys. *First Break*, *28*(6).

Winsauer, W. O., Shearin Jr., H. M., Masson, P. H., & Williams, M. (1952). Resistivity of Brine-Saturated Sands in Relation to Pore Geometry1. *AAPG Bulletin*, *36*(2), 253–277. https://doi.org/10.1306/3D9343F4-16B1-11D7-8645000102C1865D

# CHAPTER 7

# Discussion and Conclusions

The work presented in this dissertation highlights the versatility of the CSEM method to detect and characterize a variety of features on the continental shelves. The results presented are in good agreement with other datasets, but also build upon and expand previous research, in that these studies mapped novel hydrocarbon migration systems, imaged a previously unidentified hydrocarbon seep, and even identified a new source of freshwater for San Diego. Additionally, much of the data presented was collected on small vessels and with modest budgets, establishing CSEM as an effective and efficient tool for use in shallow marine studies.

The use of CSEM toward investigating resources on the continental shelves is likely to increase, especially in the search for new sources of freshwater. As over a quarter of the world's population is expected to face extreme water stress in the next two decades (Hofste et al., 2019), many countries and communities are looking for more sources of freshwater, and in some cases, looking offshore. The search for submarine groundwater can be conducted with onshore modeling or through offshore drilling projects if the geology is relatively simple. For example, submarine groundwater can sometimes be connected to onshore freshwater systems through continuous lenses meaning that onshore groundwater modeling can effectively capture the system. Conversely, the study offshore San Diego demonstrated that submarine groundwater systems can also be more complex than previously predicted, highlighting the need to map these systems directly to effectively model groundwater flow. Thus far there have been a limited number of studies using CSEM to identify submarine freshwater in a range of geologic settings (Attias et al., 2020; Gustafson et al., 2019; King et al., 2022; Micallef et al., 2020), but these

studies demonstrate that CSEM is a powerful tool to identify submarine groundwater. In a 2020 U.N. Brief, CSEM was recognized as a promising and effective tool to identify offshore fresh groundwater (Qadir, 2020).

Demand for food and energy, like water, is also expected to increase in the coming decades. Thus, large-scale development of offshore infrastructure projects, such as wave power systems, aquaculture, and wind farms has seen significant investment from industry and political entities all around the world to meet demand. Problematic to many of these developments is the existence of marine hydrocarbon seeps which are pervasive across nearly all continental margins and pose a significant hazard when developing offshore regions (Zolezzi & Parker, 2009). Many remote sensing systems have been established as effective tools to map the seafloor extent of marine hydrocarbon seeps. However, many of these methods are not sensitive to the hydrocarbons below the seafloor and instead rely on the seep being active at the time of surveying for identification. As shown in Chapter 4 of this dissertation, the near seabed (<25 meters below the seafloor) accumulations of hydrocarbons can be much more extensive than the seafloor expressions of the seeps. This observation is not only pertinent to accurately modeling the emission rates of seeps, but is also important to offshore development. For example, the misidentification of seep sources in these scenarios could complicate efforts to install wind farm foundations which commonly penetrate the seafloor to depths of 30 meters or more. It is likely then, that as wind farm and other infrastructure development occurs offshore, CSEM methods will be added to the suite of existing tools to identify suitable areas for development.

The geotechnical conditions of the seafloor, such as sediment stratigraphy and porosity, must also be considered for safe and stable installation of many types of offshore infrastructure. Currently, there are very few methods to quickly and effectively map changes in seafloor

porosity and many of these methods are limited in the areas that they can be used. Thus, the newly developed near seafloor CSEM system discussed in Chapter 6 may be a useful new tool in these seafloor characterization studies. This new system is still in early development, but the initial tests are promising. The system will need to be iterated upon to improve navigational data collection so that the vertical field data can be used in future inversions. The sensitivity of the system is expected to improve noticeably with the addition of vertical field data (Constable et al., 2016). Additionally, the photos from the camera mounted to the front of the array, although blurry, were surprisingly useful when interpreting the resistivity models. These images, if improved, could also be useful for identifying archeological sites, sensitive benthic habitats, or setting target points for sample collection using diving or ROV operations. The CUESI system will likely be developed further in the coming years and if these improvements are made, may be added to the suite of commonly used CSEM systems available today.

## 7.1 References

Attias, E., Thomas, D., Sherman, D., Ismail, K., & Constable, S. (2020). Marine electrical imaging reveals novel freshwater transport mechanism in Hawai'i. In Sci. Adv (Vol. 6). http://advances.sciencemag.org/

Constable, S., Kannberg, P. K., & Weitemeyer, K. (2016). Vulcan: A deep-towed CSEM receiver. Geochemistry, Geophysics, Geosystems, 17(3), 1042–1064. https://doi.org/10.1002/2015GC006174

Gustafson, C., Key, K., & Evans, R. L. (2019). Aquifer systems extending far offshore on the U.S. Atlantic margin. Scientific Reports, 9(1). https://doi.org/10.1038/s41598-019-44611-7

Hofste, R. W., Kuzma, S., Walker, S., Sutanudjaja, E. H., Bierkens, M. F. P., Kuijper, M. J. M., Sanchez, M. F., van Beek, R., Wada, Y., & Rodríguez, S. G. (2019). Aqueduct 3.0: Updated decision-relevant global water risk indicators. World Resources Institute, 1–53.

King, R. B., Danskin, W. R., Constable, S., & Maloney, J. M. (2022). Identification of fresh submarine groundwater off the coast of San Diego, USA, using electromagnetic methods. Hydrogeology Journal. https://doi.org/10.1007/s10040-022-02463-y

Micallef, A., Person, M., Haroon, A., Weymer, B. A., Jegen, M., Schwalenberg, K., Faghih, Z., Duan, S., Cohen, D., Mountjoy, J. J., Woelz, S., Gable, C. W., Averes, T., & Kumar Tiwari, A. (2020). 3D characterisation and quantification of an offshore freshened groundwater system in the Canterbury Bight. Nature Communications, 11(1). https://doi.org/10.1038/s41467-020-14770-7

Qadir, M. (2020). UN-Water, 2020: UN-Water Analytical Brief on Unconventional Water Resources. Geneva, Switzerland.

Zolezzi, F., & Parker, E. J. (2009). Offshore Geohazards and their Implication to Industry. https://www.researchgate.net/publication/279280711

# APPENDIX A

# Using Controlled Source Electromagnetic Methods for Detecting Submerged Archaeological Resources
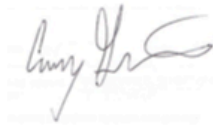
NPS NCPTT Grant: P19AP00140

## FINAL REPORT
## December 2021

Prepared For:
National Center for Preservation Technology and Training



Prepared By:

Amy Gusick, Principal Investigator
Associate Curator, Archaeology
Natural History Museum Los Angeles County
agusick@nhm.org
213-763-3370

Project Team:
Amy Gusick, Natural History Museum Los Angeles County
Jillian Maloney, San Diego State University
Steven Constable, Scripps Institution of Oceanography
Todd Braje, San Diego State University
Kristin Hoppa, Channel Islands National Park
Roslynn King, Scripps Institution of Oceanography

**TABLE OF CONTENTS**

**Figures**

**Tables**

# 1. Executive Summary

Sea-level rise following the last glacial maximum (~20 kya) has resulted in the submergence of paleochannels, tar seeps, and archaeological sites on continental shelves. The distribution of these sites is important for archaeological research, offshore infrastructure development, and environmental hazard assessment. Identification of these sites is typically attempted using a combination of side scan and subbottom sonar remote sensing methods, followed by evaluation of hundreds of resulting images to select targets for sampling. Our recent research suggests that the process of narrowing down targets for sampling may be facilitated by incorporating controlled source electromagnetic (CSEM) equipment into the remote sensing surveys. CSEM measures the apparent resistivity of the submerged units (i.e., porosity).

Using MARE2DEM software, we developed a model to test CSEM effectiveness for identifying shell midden deposits, tar seeps, and paleochannels. Results indicated that a modified bottom-towed CSEM system should be able to resolve all three targets. We, therefore, designed and built CUESI, a Compact Undersea Electromagnetic Source Instrument. Initially beginning with Porpoise, a surface-towed CSEM system developed by the Electromagnetic Laboratory at Scripps Institution of Oceanography, we created a modified CSEM system to be deep-towed with frequencies that can detect specific targets of interest for identifying submerged maritime cultural landscapes within the Southern California Bight.

Testing the CUESI system included basic functionality tests (23 & 25 September 2020) as well as field tests (24-25 May 2021). The testing program was designed as a proof of concept using areas of known targets of interest. Previous subbottom data collected offshore from the Northern Channel Islands during a Bureau of Ocean Energy Management project focused on identifying features on the landscapes for core testing. The resulting core data show areas on the submerged landscapes where deposits containing shell and rock are located beneath marine sediment. These core locations were surveyed using the CUESI to test the sensitivity of the system toward characterizing changes in seafloor porosity.

Initial tests of the system acted as guides to better understand CUESI functionality and, importantly, modifications to the system needed for successful use in the field. The initial results of the data collected in May 2021 show that the CUESI system is sensitive to hydrocarbons. However, data collected on 24 May 2021 were found to be chaotic. The lack of a depth sensor on CUESI created uncertainties in correspondence with navigation data. After modifications to the system, CUESI was used to collected data on a subsequent project and these data appear, at least in initial processing, to be effective at identifying a known lag deposit, to model porosity of a core sample with a shell deposit, and identify a known tar seep. These results suggest that CUSEI may be an effective system for consideration in surveys focused on identifying features across paleolandscapes and may narrow target selection for subsequent sampling.

## 2. Introduction

Sea-level rise following the Last Glacial Maximum (LGM) (~20 kya) submerged millions of square kilometers of coastal landscapes around the world, complicating efforts to understand the paleolandscapes, paleoecology, human dispersals, and the cultural histories of these now drowned regions (Clark et al. 2014). One of these regions surrounding the Northern Channel Islands (NCI) boasts one of the highest densities of terminal Pleistocene (15,000-11,500 yrs BP) and early Holocene (11,500-8,000 yrs BP) archaeological sites in the New World (Figure 1) (Erlandson 1994; Erlandson et al. 2001; Gusick and Erlandson 2019; Rick et al. 2005). Evidence from these terrestrial sites indicates: 1) that the earliest occupants of the NCI were seafaring maritime hunter-gatherers; and 2) that additional Paleocoastal archaeological sites (~15,000-8,000 cal BP) are likely located on the submerged landscapes of the NCI. The search for submerged sites has extended onto the regional continental shelf, but Paleocoastal sites have not yet been identified on this submerged landscape (Gusick et al. 2021). Recent research, however, suggests that with the right technologies features such as paleochannels, shell deposits and offshore tar seeps – all features used and/or created by indigenous communities during the terminal Pleistocene and Holocene along the Pacific Coast – can be identified and used to model paleolandscape and paleoecology on archaeologically sensitive submerged landscapes (Gusick et al. 2019).
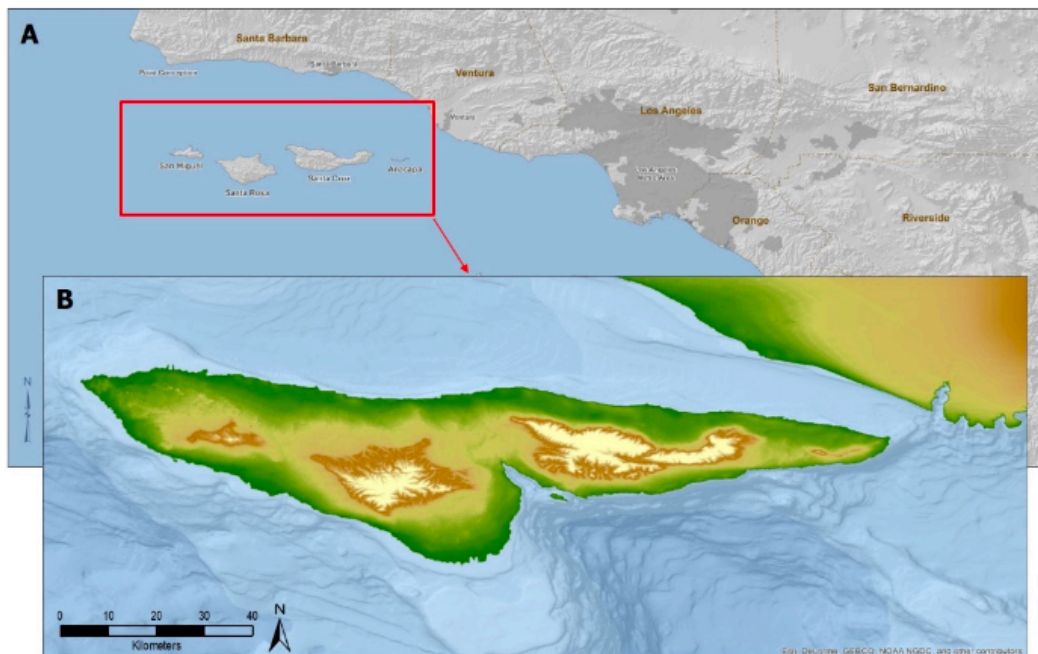
The identification of these landscapes is important for archaeological research, offshore infrastructure development, and environmental hazard assessment. Identification of culturally important features or culture sites on submerged landscapes is typically attempted using a combination of side scan and subbottom sonar remote sensing methods, followed by evaluation of hundreds of resulting images to select targets for sampling. Yet, the process of narrowing down targets for sampling may be facilitated by incorporating controlled source electromagnetic (CSEM) equipment into the remote sensing surveys. CSEM measures the apparent resistivity of the submerged units (i.e., porosity), a different variable than that detected by sonar methods. While typically used to identify hydrocarbon in offshore geology, initial modelling of a CSEM system modified to be deep-towed and to detect shallow, varying porosities was promising and the project team worked with the Marine Electromagnetic (EM) Laboratory at Scripps Institution of Oceanography (SIO) to build a modified CSEM system. This equipment was then tested for functionality by surveying over known locations with shell and rock deposits buried beneath sediment on the continental shelf of the California mainland and the NCI.

## 3. Design Methods and Materials

Initially beginning with Porpoise, a surface-towed CSEM system developed by the Marine EM Laboratory in the Institute of Geophysics and Planetary Physics, University of California, San Diego (Sherman et al. 2017), we modelled and then built CUESI, a Compact Undersea Electromagnetic Source Instrument. CUSEI is a CSEM system modified to be deep-towed with frequencies that can detect specific targets of interest for identifying submerged maritime cultural landscapes within the Southern California Bight (SCB).

### A. Initial Modeling

Using MARE2DEM software (Key 2012; Key and Ovall 2011) we developed a model to test CSEM effectiveness for identifying shell midden deposits, tar seeps, and paleochannels, three targets of interest in on the paleolandscapes of the SCB. Characteristic porosities of these targets and the surrounding geologic units of modern medium to course sands and underlying shale were used in the model. These data were related to resistivity values using Archie's law (Archie 1942) and then used to develop an initial model to determine if our targets could be detected with CSEM. This methodology should also allow shell middens to be distinguishable from other anomalous targets identified by sonar systems (i.e., buried rock outcrops, corals, etc.).

The model assumed three targets: 1) a 10,000 year old paleochannel that is 200 meters (m) wide, 8 m deep and is overlain with 2 m of Holocene sediments; 2) a shell midden of 10 m in diameter and 1 m in height located on the paleosurface overlain with Holocene sediments; and 3) a tar seep mound that rises 1 m above the sea floor and is 30 m in diameter. Results indicated that the Porpoise surface-towed CSEM system can resolve

the tar seep and the paleochannel, but not the shell midden. We reran the model assuming a CSEM system modified to be bottom-towed that emits an electric ternary waveform of frequencies at 3Hz, 9Hz, 15Hz, 21Hz, and 39Hz, and receivers spaced at 5 m, 10 m, 20 m, and 40 m. The model shows that this modified system is capable of resolving all three targets, including the shell midden (Figure 2). This new CSEM system is CUESI.
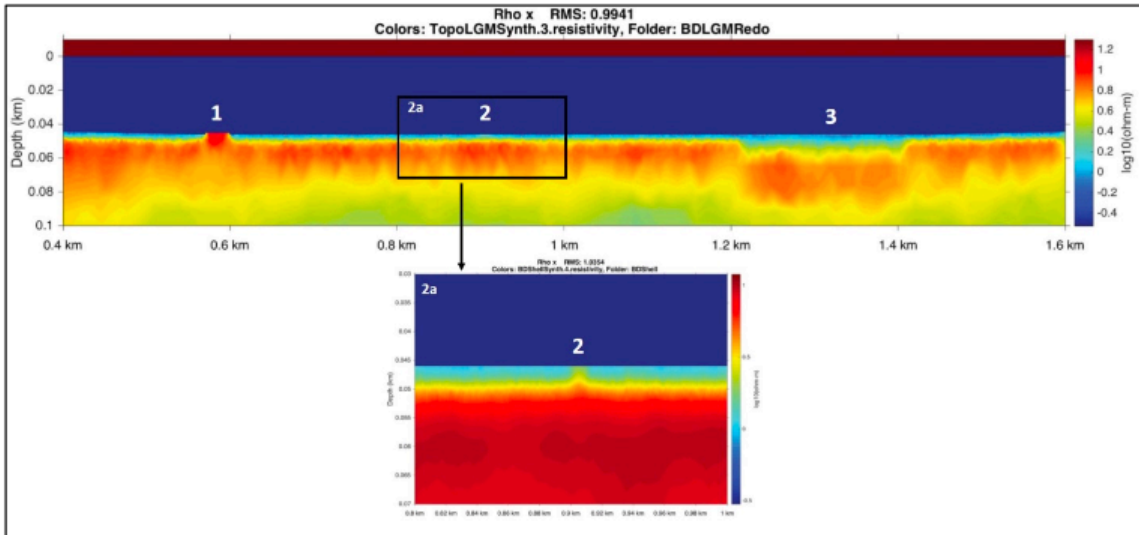


Figure 2. MARE2DEM model output showing resolution of three targets using a bottom towed CSEM system. Targets are, 1) Tarseep/mound; 2) Shell midden; 3) Paleochannel. Image 2a is magnification of target 2 results showing resolution of shell midden. Image modified from King et al. 2018.

## B. CUESI Design

The CUESI was designed as a horizontal electric dipole electromagnetic transmitter for CSEM sounding within 5 m of the seafloor. The instrument uses external power to output a current up to 5 amps to a towfish 10 m behind the transmitter (noted as Transmitter Electrode Dipole in Figure 3). Here, 5 amps is transmitted into the seawater with two 10 cm long, 1.5 cm diameter soft copper tubing held 2 m horizontally apart on a rigid frame for a source dipole moment up to 10 Am. Behind the dipole are two three-axis electric field receivers (noted as 3-axis Vulcan receivers in Figure 3) spaced 10 and 25 meters from the dipole respectively. All three towfish are positively buoyant (0.57 to 0.63 lbs) so that when a wire touches the seafloor, the towfish become neutrally buoyant at an altitude between 90 to 100 cm. CUESI is designed to double as a drop weight in continuous towing operations so that wave energy is not transferred to the array allowing towing altitude to remain consistent.

All towfish are equipped with internal and external instruments to record navigational data. The towfish loggers record pressure, compass data, acceleration on 3-axis on 1 to 2 second intervals and an externally mounted compass allows for redundancy. The receiver towfish record the electric field in three directions on a 500 Hz logger and, in order to achieve consistent timing along the array, a timing pulse from CUESI. CUESI is equipped with a camera, lights, clock, altimeter, conductivity and temperature sensor, and a pressure gauge. The entire array sends packages of data to the surface systems on 2 to 10 second intervals to aid in navigation and survey troubleshooting.
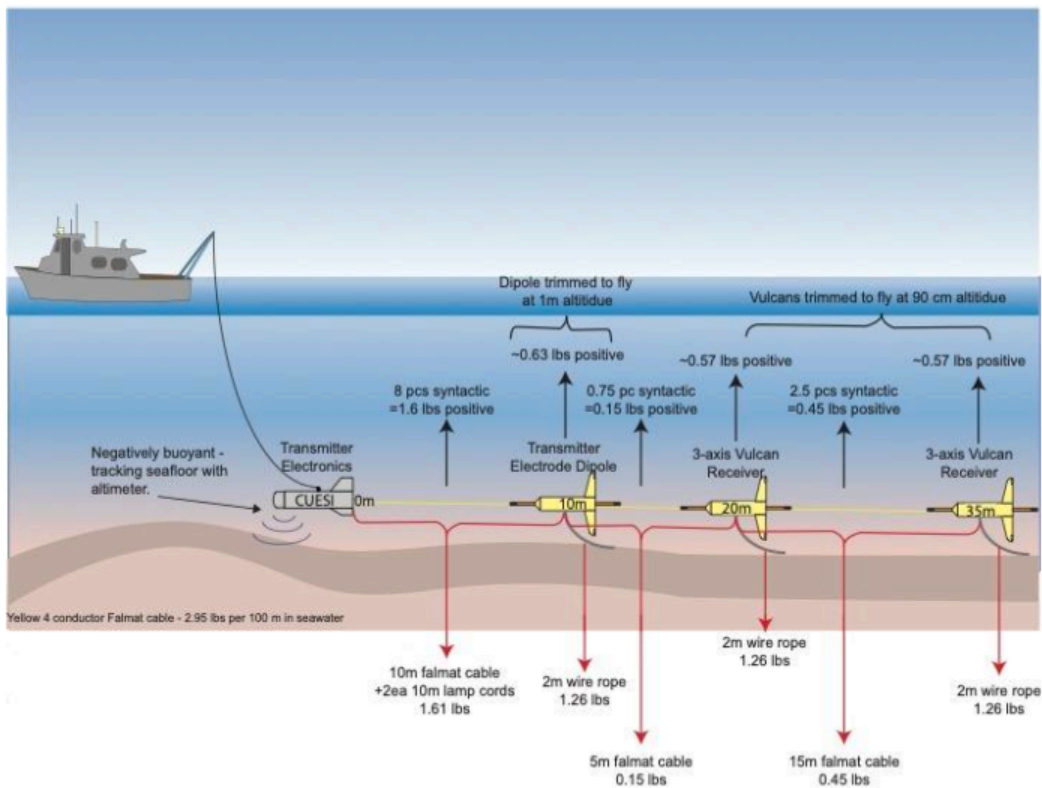


Figure 3. Schematic of CUESI array illustrating instrument spacing and buoyancy of the array.

## C. CUESI Build

The CUESI system includes four pressure cases in tow frames housing the equipment: one transmitter and three receivers.

**Transmitter Tow Frame:**
*Dimensions:* ~18 inches x 36 inches, Weight: ~200 lbs max
*Houses:* transmitter, altimeter, and camera

145

*Input:* 120v AC power from tow-vessel
*Output to receivers:* 1-10 Amp current-controlled Waveform and timing pulse
*Output to tow vessel:* altimeter readings
*Build:* The electronics designed and built by the EM lab are housed in a MkII pressure case. Figure 4 shows the tow frame design. There is real time communication and commands to and from the transmitter.
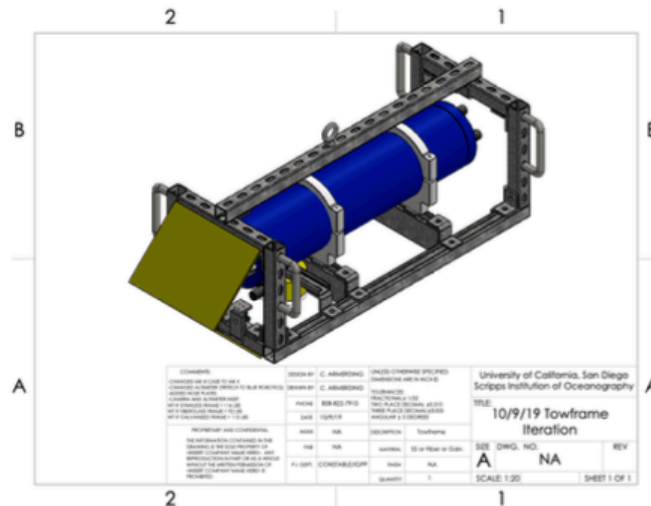


Figure 4. Transmitter tow frame schematic.

**Receiver Tow Frames (3):**

*Dimensions:* 10 inches x 48 inches, Weight: 70 lbs each
*Build:* First Receiver Tow Frame supports a 2-meter horizontal electric dipole with 10 cm long electrodes and a vertical 1-meter dipole. The horizontal electric dipole transmits the electric current generated from the transmitter housed in the MkII pressure case of the transmitter tow frame. The vertical 1-meter dipole records the vertical electric field to the logger housed within a receiver pressure case. Second and Third Receiver Tow Frames support a 2-meter horizontal stinger with two standard electrodes and a 1-meter vertical fin with two small electrodes at each tip (Figure 5). The dipoles record the inline and vertical components of the electric field respectively and record the responses within the data logger housed in receiver pressure case. Additionally, the receivers record the timing pulse generated from the transmitter on a serial data logger.
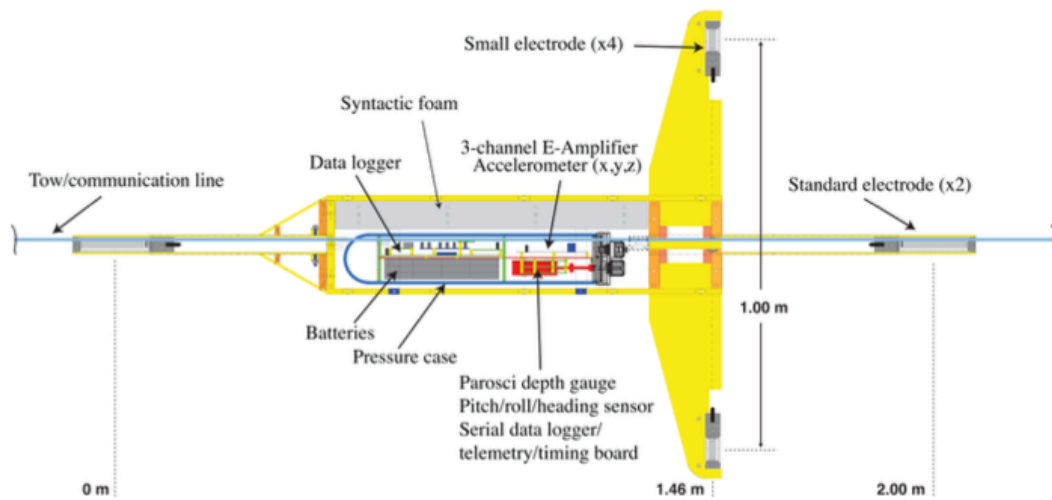
Figure 5. Cut-away schematic of the receiver tow package (Constable et al. 2016)

## 4. CUESI System Tests

Testing the CUESI system included basic functionality tests as well as field tests. The testing program was designed as a proof of concept using areas of known targets of interest. Previous subbottom data collected offshore from the NCI during a Bureau of Ocean Energy Management (BOEM) project focused on identifying features on the landscapes for core testing. These core data show areas on the submerged landscapes where deposits containing shell and rock are located beneath marine sediment. These core locations were surveyed using CUESI to test system sensitivity toward characterizing changes in seafloor porosity. This is critical to the CUESI success as targets of interests, especially shell middens sites, are predicted to have a higher pore volume than typical marine sediment and in theory could be identified with the CUESI system.

### A. Study Areas

The CUESI study areas included the channel between Santa Cruz and Santa Rosa islands and in the area of the La Goleta tar seep off Isla Vista (Figure 6).
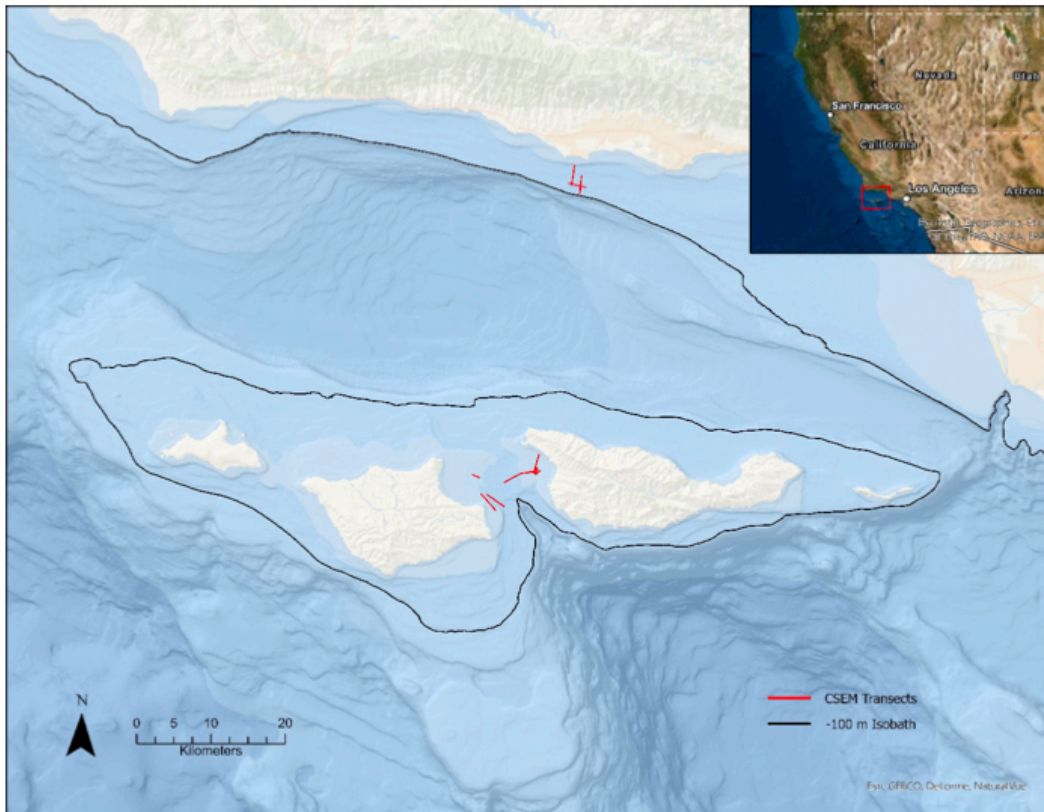
Figure 6. Regional project location showing areas surveyed during the current testing. Red lines indicate CUESI survey lines. Black lines indicate the -100 m isobath.

## B. Deployment/Recovery Operations

As part of the testing, receiver preparation, deployment and retrieval operations for the CUESI were developed.

*Receiver Preparation*

At the start of every survey day, 25 cm silver-silver chloride electrodes must be fixed and cabled to the receiver loggers and rigid frames. External compasses for the receivers must also be set and fixed to the receiver frames. Receivers are then cabled together to create the intended array geometries on four conductor Falmat cables using detachable/reusable pins.

*Deployment*

      1.      CUESI pressure sensor must be plugged into an external pressure case that logs output and provides power to the pressure sensor. Pressure sensor will start recording immediately upon charge.

      2.      Set CUESI camera to intended sampling interval, plug into CUESI power, and secure camera in pressure case. Fasten the pressure case using hex bolts and

then attach the pressure case to CUESI facing downward at an angle between 10 to 30 degrees.

3.      Start CUESI by plugging in 'start box' to the CUESI pressure case and then sync CUESI internal clock using the external GPS clock within the start box. Record time tag, time, and scrutinize direction and severity of time drift on GPS clock. If satisfied, unplug GPS clock and seal the CUESI pressure case with seal screws.

4.      On the deck computer and on the CUESI winch, switch power to CUESI from internal batteries to external (boat) AC power. Review data stream on CUESI graphical user interface (GUI) from CUESI to ensure CUESI and all three towfish are sending data packages up the cable at the intended intervals.

5.      Hand-deploy the third towfish in the array off the stern of the vessel. Depending on currents, the water speed for deployments should be between 0.5 to 2 knots for safe deployment. Use boat power to achieve these conditions.

6.      Once the towfish pulls the Falmat cable out behind the vessel, hand deploy the second towfish in the array in a similar fashion to the third towfish taking care to not catch the wire rope on the deck. Allow array to straighten before hand-deploying the Transmitter Electrode Dipole towfish.

7.      Allow the array to straighten behind the vessel before using an A-frame, two taglines, and the CUESI winch to deploy CUESI. When CUESI is at the water line, remove tag lines and drop CUESI 1 m below the water line. Check that altimeter readings are expected considering the water depth and start transmitting. Check that the voltage and amperage are within expected (programmed) ranges and that all instruments are still sending data packages up the cable.

8.      Lower the array using the winch until the altimeter reads between 2 and 5 m (depending on sea-state). Tow the array at 2 knots (speed through water) adjusting CUESI height above seafloor using the winch controls.

*Recovery*

1.      Stop CUESI transmission using the deck computer.

2.      Notify the crew of intent to recover the array. Station two people at stern with hook and pole (for later taglines) to watch for the array and tend the winch line.

3.      Use winch to haul in CUESI and towfish array, noting altimeter reading. Slow haul in when altimeter readings approach water depth. When CUESI is first sighted at the water line, stop the winch, and hook the CUESI frame with two taglines.

4.      Recover using the taglines, A-frame, and winch and secure CUESI to the deck.

5.      Hand pull in each towfish while tending Falmat cable and secure to deck.

6.      Once all gear is secured on deck, remove CUESI seal screw, plug in start box, and record time tag.

7.    Power down CUESI using the start box and then switch off power to the winch.

8.    If no surveying is planned for the next twelve hours, remove silver-silver chloride electrodes from receivers and unplug CUESI pressure sensor from the external pressure case.

## C. Functionality and Field Tests

The tests of the system included two functionality tests that occurred near to SIO, and two field tests.

### 23 September 2020 – Functionality Test

Initial tests of the system occurred on 23 September 2020 aboard the SIO R/V *Beyster* (Figure 7). This was the first test of the CUESI system aboard a vessel and the test was designed to gain an understanding on how the system tows through the water, outputs current, responds to winch and computer operations, and if the receivers collect data on all three channels. The altimeter malfunctioned on this first test and the ship time was cut short in order to bring the equipment back to the EM lab for modification.

Test Results:
- Altimeter is not functioning.
- The cables that connect CUESI to the two 10 cm long 1.5 cm diameter soft copper tubing on the transmitter electrode dipole towfish has too much resistance and is inadequately shielded from seawater to output current on the horizontal electric dipole.
- CUESI was not hydrodynamic and required more weight and less drag. CUESI needs only one stabilizer wing and needs a stronger connection to the tow cable.
- The connection between the CUESI cables and the two 10 cm long 1.5 cm diameter soft copper tubing on the transmitter electrode dipole towfish need to be improved.
- CUESI needs a conductivity and temperature sensor to remove variables during data processing.

### 25 September 2020 – Functionality Test

Another test of the system occurred on 25 September 2020 after modifications to the CUESI tow frame including, removal of side panels, 24 lbs of weight added to the frame, and a single vertical wing was attached to the frame for stability. The connection between CUESI and the tow cable was reinforced to reduce roll on CUESI during towing and a new altimeter was installed on the CUESI frame. This test was successful.

Test Results:
- The 0.5-inch diameter shielded aluminum wire resulted in consistent output current.

- Modifications to the weight, panels, and wings of CUESI reduced pitch and roll of CUESI.
- The new altimeter functioned without issue.
- The CUESI frame should be modified to have permanent weight and a more robust frame considering the drag on the system.
- A conductivity sensor will need to be added to the CUESI system.
- In order to use phase data, we will need accurate timing. This can be achieved if the CUESI internal clock can be synced to a GPS clock. We need to alter CUESI for these capabilities.
- The buoyancy of the receiver towfish is too high and need to be trimmed to decrease buoyancy.
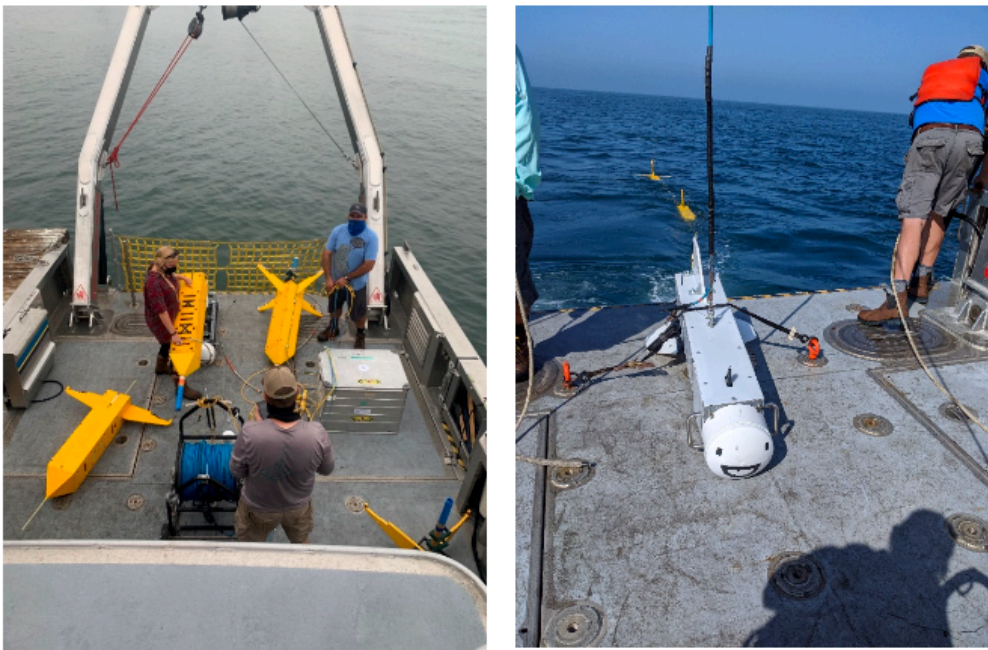


Figure 7. Left: The EM crew getting ready to deploy the system. Yellow objects are the three receiver tow frames that house the receivers. Right: Deploying the EM system. The white object is the transmitter tow frame that houses the transmitter.

### 24 May 2021 – Field Test

The initial field test for the CUESI system focused on areas with known targets buried beneath marine sediment off the western coast of Santa Cruz Island (Figure 8). This was to test CUESI frequencies over core locations with known varying sediment types from a prior BOEM survey. These cores exhibit changes in lithology that offer a unique test of the sensitivity of the CUESI system to thin (>50 cm) lenses of material of varying character. Additional tests of the CUESI system focused on the La Goleta tar seep

offshore Isla Vista (Figure 9). This tested the sensitivity of the CUESI system to hydrocarbons and to compare the data collected with the CUESI system to that collected with the surface-towed CSEM Porpoise system.
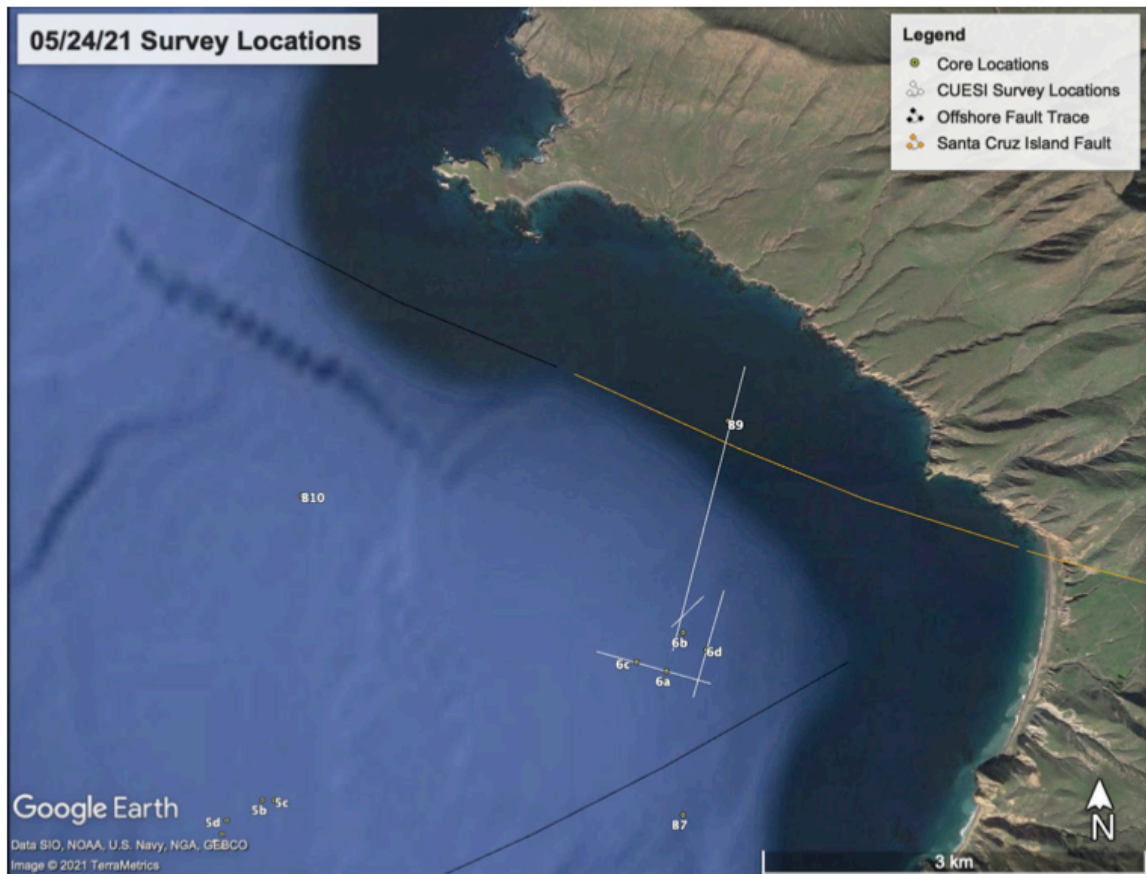


Figure 8: Survey location for CUESI survey off the western coast of Santa Cruz Island. Targeted cores locations from BOEM survey are shown.

Table 1. CUESI survey lines off Santa Cruz Island – 05/24/2021.

| Site | Survey Line Name | Start Lat. (DD) | Start Lon. (DD) | End Lat. (DD) | End Lon. (DD) | Length (km) |
|------|------------------|-----------------|-----------------|---------------|---------------|-------------|
| NCI | C_052421_NCI_L1 | 34.024434° | -119.915818° | 34.022035° | -119.905759° | 0.98 |
| NCI | C_052421_NCI_L2 | 34.021103° | -119.907179° | 34.028807° | -119.904493° | 0.92 |
| NCI | C_052421_NCI_L3 | 34.028380° | -119.906299° | 34.026150° | -119.909210° | 0.37 |
| NCI | C_052421_NCI_L4 | 34.024487° | -119.909014° | 34.045192° | -119.902707° | 2.41 |
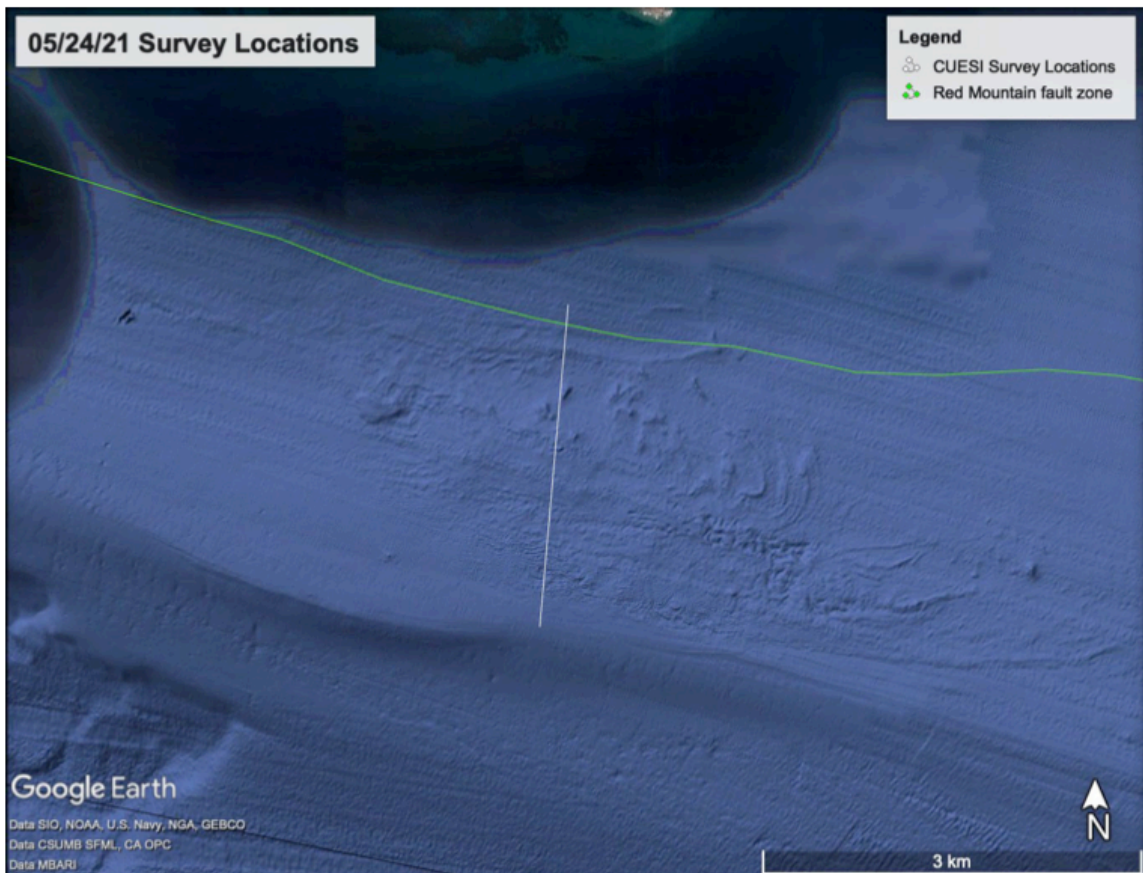
Figure 9: Survey location for CUESI survey offshore Isla Vista targeting La Goleta Seep Field.

Table 2. CUESI survey lines off Isla Vista – 05/24/2021

| Site | Survey Line Name | Start Lat. (DD) | Start Lon. (DD) | End Lat. (DD) | End Lon. (DD) | Length (km) |
|------|------------------|-----------------|-----------------|---------------|---------------|-------------|
| IV | C_052421_IV_L1 | 34.384871° | -119.851949° | 34.362481° | -119.854339° | 2.54 |

Test Results:
- The relationship between internal CUESI clock drift and commands sent along the tow cable must be better understood.
- The communication box electronics should be investigated to avoid further cruise disruptions.
- The current control within CUESI needs to be calibrated and refined for more control over output current.

## 25 May 2021 – Field Test

This survey extends the area surveyed the previous day with CUESI as well as allowing for comparison between CUESI and Porpoise datasets (Figure 10). Additionally, several tie-lines were collected to directly compare the data collected by CUESI in different directions to gain a better understanding as to the influence of navigational noise or currents on data collection and quality.
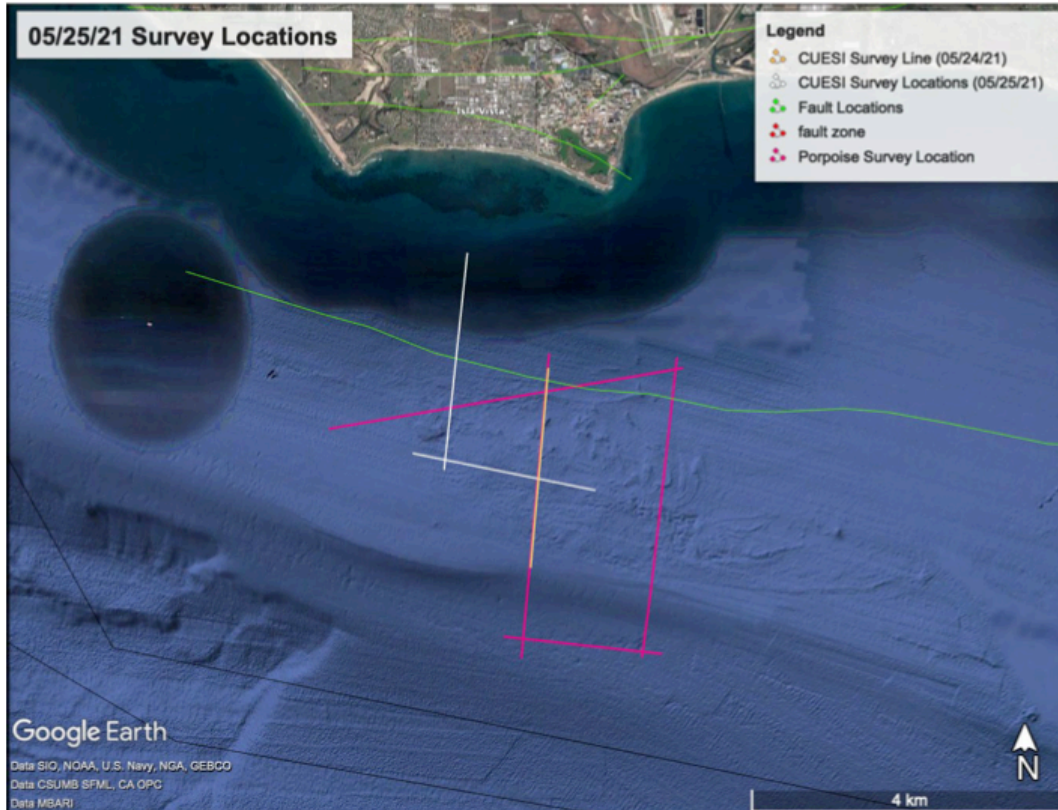


Figure 10. Survey location for CUESI survey and Porpoise survey offshore Isla Vista targeting La Goleta Seep Field. This survey extends the area surveyed the previous day with CUESI (noted in orange) and provides a direct comparison with Porpoise datasets.

Table 3. CUESI survey lines off Isla Vista – 05/25/2021

| Site | Survey Line Name | Start Lat. (DD) | Start Lon. (DD) | End Lat. (DD) | End Lon. (DD) | Length (km) |
|------|------------------|-----------------|-----------------|---------------|--------------|-------------|
| IV | C_052521_IV_L1 | 34.371202° | -119.845562° | 34.375373° | -119.870117° | 2.36 |
| IV | C_052521_IV_L2 | 34.373666° | -119.866080° | 34.397609° | -119.862828° | 2.71 |

Table 4. Porpoise survey lines off Isla Vista – 05/25/2021

| Site | Survey Line Name | Start Lat. (DD) | Start Lon. (DD) | End Lat. (DD) | End Lon. (DD) | Length (km) |
|------|------------------|-----------------|-----------------|---------------|--------------|-------------|
| IV | PS_052421_IV_L1 | 34.386521° | -119.852128° | 34.353107° | -119.856133° | 3.9 |
| IV | PS_052421_IV_L2 | 34.355452° | -119.858445° | 34.353427° | -119.837322° | 2.03 |
| IV | PS_052421_IV_L3 | 34.353165° | -119.839996° | 34.386027° | -119.835083° | 3.82 |
| IV | PS_052421_IV_L4 | 34.384896° | -119.834129° | 34.378229° | -119.881618° | 4.51 |

Test Results:
- The CUESI frame needs to be rebuilt out of heavier and stronger materials, possibly welding a frame for maximum strength.
- Deployment of both the CUESI system and the Porpoise system should be avoided if possible as transitioning between these two systems takes a significant amount of time.
- To reduce uncertainties in navigation, CUESI should be outfitted with a depth sensor.

## 5. Results and Discussion

Initial tests of the system acted as guides to better understand CUESI functionality and, importantly, modifications to the system needed for successful use in the field. While some needed modifications are apparent in the field, others are identified during data processing, which in some instances can take months. The CSEM data in real time does not produce images akin to those from sonar data. The processing of CSEM data involves extracting amplitude and phases of the CSEM response functions from the collected raw time-series data. To increase the signal-to-noise ratio, the resulting transfer function estimates are stacked using an arithmetic mean to obtain the transfer function estimates for every stacking window along with an error estimate. This method yields high quality amplitude and phase response data for the receivers as a function of position and frequency. The signal to noise ratios for these data are scrutinized to ensure the CSEM data associated with the harmonics are well above the noise floor, making them suitable for inversion.

These data are then modelled with a modeling software that uses the publicly available, goal-oriented, adaptive, finite-element two-dimensional (2D) MARE2DEM inversion and modeling code of Key (2016). This code uses Occam's Inversion, a method that regularizes the inversion to obtain the smoothest resistivity model that fits the data (Constable et al. 1987). CSEM data are scrutinized manually for obvious outliers and subjected to an error floor, dependent on data quality, before being included in the model as finite-length dipoles.

The starting models include the seawater as a fixed parameter, using conductivity data collected by the dorsal and available bathymetric data. Thus, the free inversion regions are reduced to the area below the seafloor and set to a uniform starting resistivity of 1 $\Omega$m. Inversion parameter grids are constructed using quadrilateral cells that increase in height with depth to mimic the loss of resolution of the EM method with distance. Due to the adaptive nature of the MARE2DEM code, this computation grid is allowed to refine where necessary to fit the data. The resistivity inversions are allowed to run until a minimum root mean square is achieved; this value is then increased by ten percent to avoid overfitting. The final resistivity inversions are then ready for analysis and discussion (Figure 11).
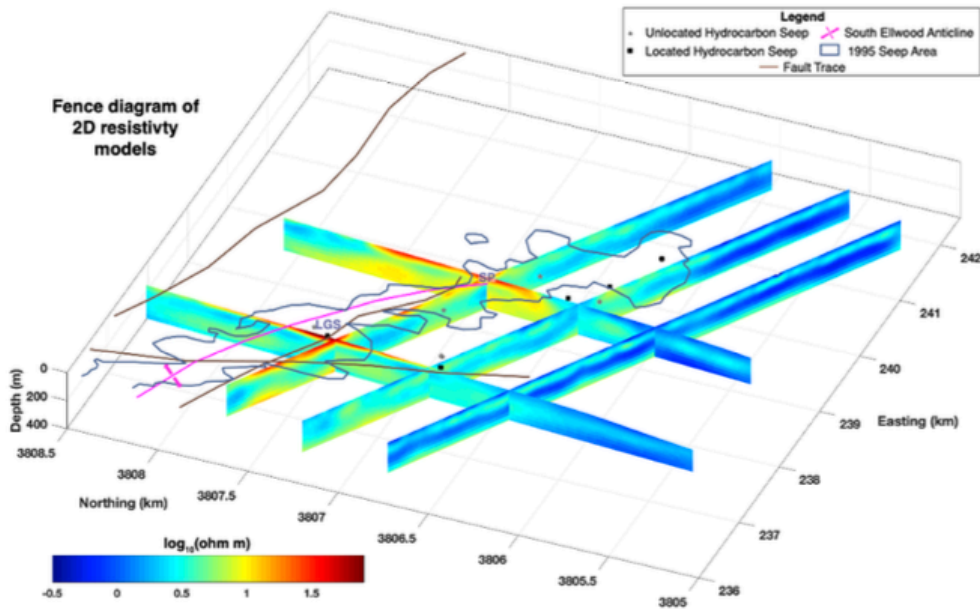


Figure 11. Example of a fence diagram created using processed CSEM data showing locations of tar seeps in red. This is not from the current project. Image by Roslynn King.

The initial results of the data collected with the current project show that the CUESI system is sensitive to hydrocarbons. As seen in Figure 12, the amplitude response data from the CEUSI system shows sensitivity to the hydrocarbon that has been identified by the Porpoise system. The model and amplitude responses are collocated as seen in Figure 10 and target La Goleta Seep Field. The amplitude response is in agreement with the final resistivity model of the surface-towed Porpoise system and demonstrate that both systems are sensitive to hydrocarbon accumulation associated with La Goleta Seep field. This was an important test of the CUESI system to ensure overlapping identification from a system that has already been established. Future tests of the CUESI sensitivity to hydrocarbons will include variations in final models as CUESI is likely to better model the shape and type of seep.
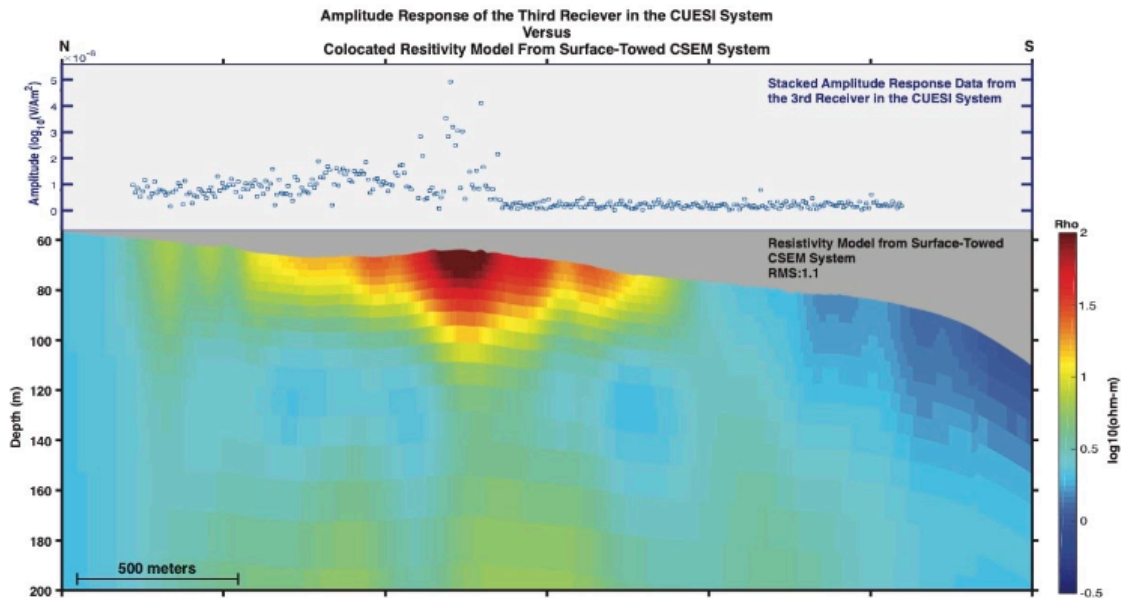
156

Figure 12: Figure illustrating the final resistivity model generated from Porpoise data versus the 10-second stacked amplitude response recorded by the third receiver in the CUESI system/array. Warm colors in the lower figure (resistivity model) indicate areas of higher resistivity typical of hydrocarbon occurrence. In the upper amplitude response figure, higher amplitude generally corresponds to regions of higher resistivity. Image by Roslynn King.

Data collected on the 24 May 2021 field test were processed and found to be chaotic. The lack of a depth sensor on CUESI created uncertainties in correspondence with navigation data. Additionally, the error in output current was 10% of the signal. This is too large to reach the sensitivity needed to identify targeted features in on the sea floor. Due to the nature of CSEM data processing, these issues were identified during post-processing. Once identified, this allowed us to modify the system to include depth sensor for accurate navigational data.

After completion of the needed CUESI system modifications identified from the NCPPT cruises, we were able use the CUESI system on a subsequent project funded by the National Oceanic and Atmospheric Administration Office of Ocean Exploration (OER). With the inclusion of a depth sensor, in addition to the altimeter, and an adjustment in frequencies, the CUESI system appears to have functioned as intended.

On 09 September 2021, we surveyed coring locations offshore western Santa Cruz Island using CUESI array (Figure 13). This repeated some of the transect lines run during our field tests for the NCPTT project, and added new areas that were consistent with our goals for the OER project (Figure 14).
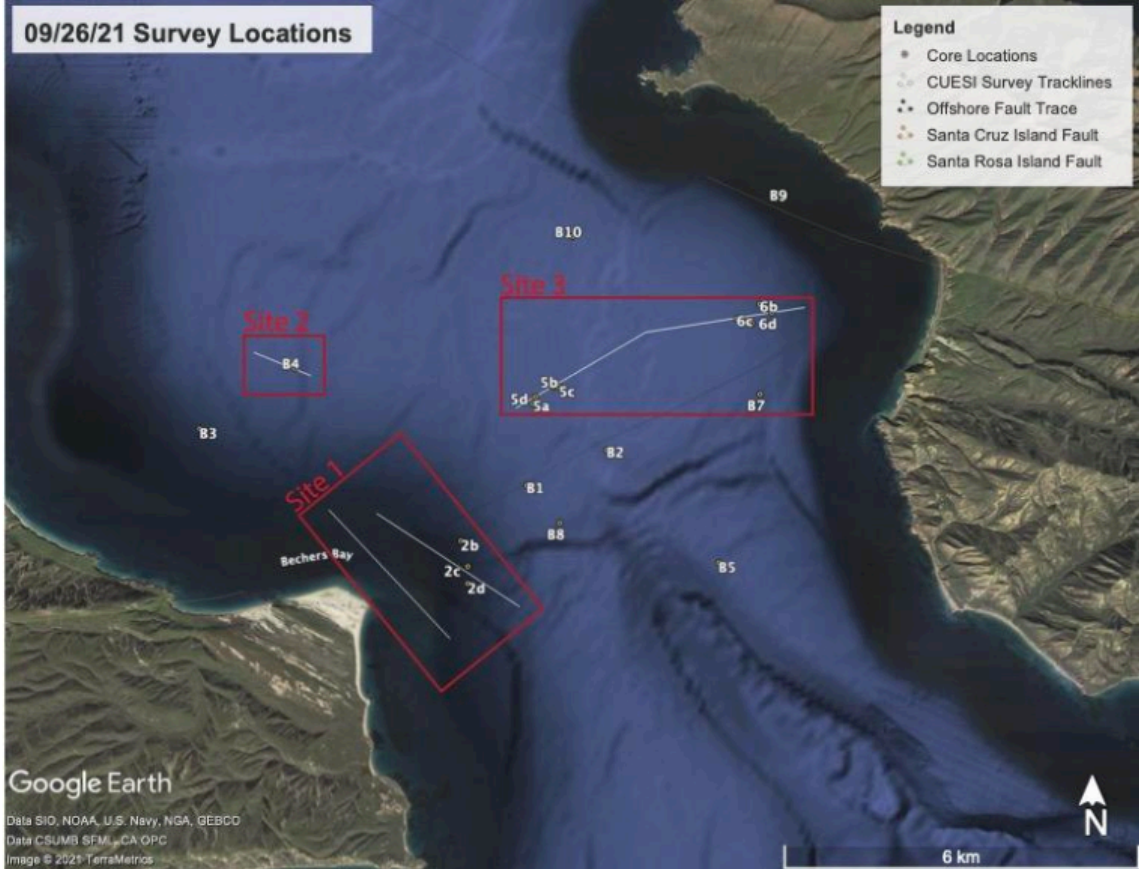
Figure 13: Survey location for CUESI survey on 09/26/21. This CUESI survey targeted possible seepage along a fault trace and several core locations.

Table 5. CUESI survey lines in Santa Cruz Island Channel – 09/26/2021

| Site | Survey Line Name | Start Lat. (DD) | Start Lon. (DD) | End Lat. (DD) | End Lon. (DD) | Length (km) |
|---|---|---|---|---|---|---|
| 1 | CUESI_092621_L1 | 33.976089° | -119.963633° | 33.995084° | -119.985243° | 2.92 |
| 1 | CUESI_092621_L2 | 33.994707° | -119.976740° | 33.980817° | -119.951200° | 2.81 |
| 2 | CUESI_092621_L3 | 34.018664° | -119.998754° | 34.015043° | -119.988362° | 1.0 |
| 3 | CUESI_092621_L4 | 34.010419° | -119.951853° | 34.021606° | -119.928425° | 2.51 |
| 3 | CUESI_092621_L5 | 34.021606° | -119.928425° | 34.025226° | -119.900086° | 2.64 |

One of the modifications to the CUESI system was to correct the auto-shot camera that was installed inside a pressure case on the CUESI frame. This camera was set to take photos every four seconds. This resulted in over 2000 images. These images can be location-related to the CSEM data to provide images of the sea floor. This was a test of this concept and the results were blurry, but helpful in collecting images of various types of sea floor and marine animals (Figure 14). Plans for this improving imaging capability on the CUESI include a more advanced camera, and the possibility of adding a data cable that can transmit images topside during survey.
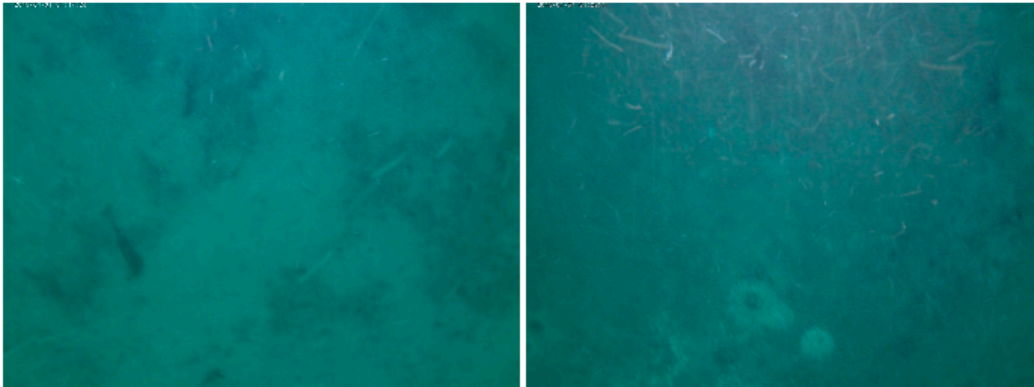


Figure 14. Examples of images of images from the CUESI camera. These are blurry, but the type of sea floor can be inferred from the photos. These also show that the concept was successful.

Although full processing of CUESI data is forthcoming, preliminary results are promising. Two of the core locations surveyed with the CUESI appeared in the processed data as areas with high resistivity and/or porosity values set in our starting models.

#### Core 6c
This core location showed a lag deposit starting at approximately 100 cm depth beneath the sea floor. The ability of the CUESI to identify these types of deposits is important for identification of buried lithic material, as well as changes in the sediment that can indicate a paleoenvironmental shifts, or ancient habitats covered with marine deposits during marine transgression (Figure 15).
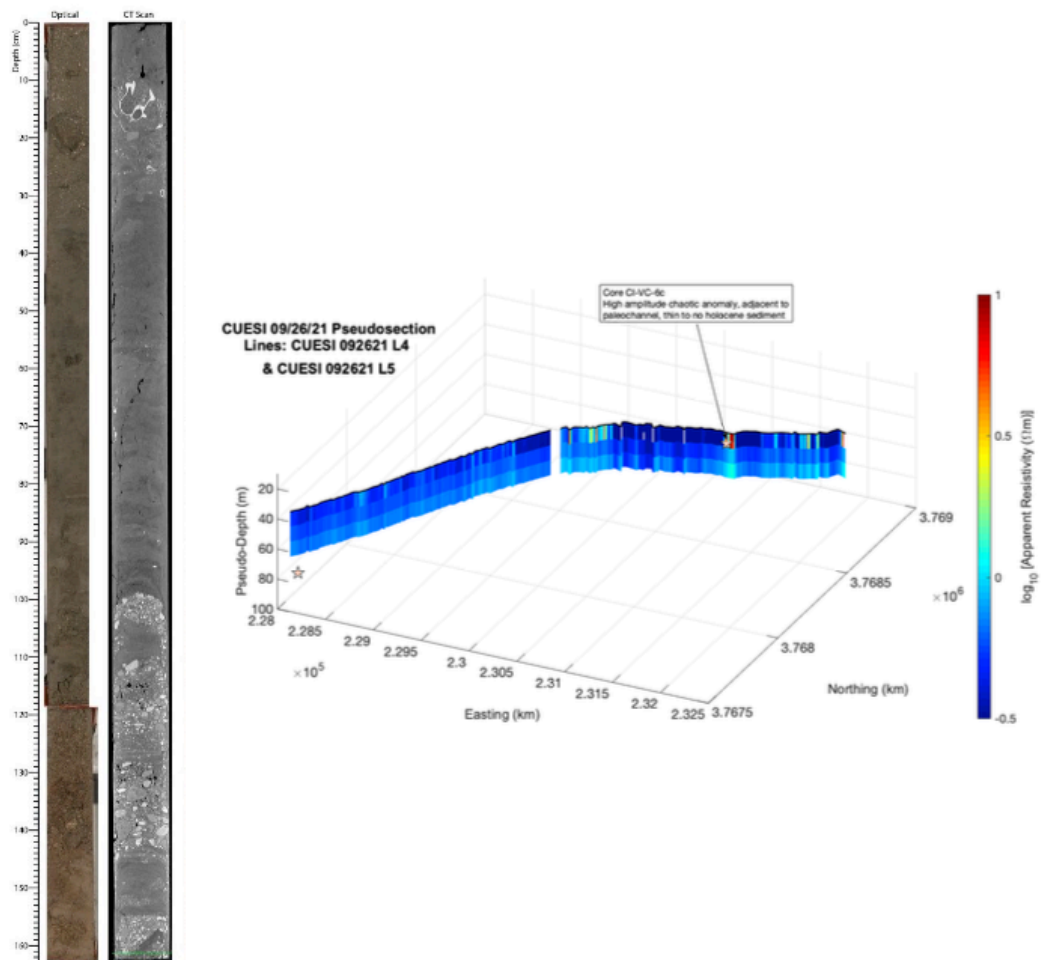
Figure 15. Left: Split core with lag deposit starting at ~100 cm. Right: Pseudosection of survey over this core (starred location) showing high resistivity values, indicated as red colors on the chart. Image by Roslynn King.

## Core B4

This core location showed a shell deposit starting at approximately 55 cm depth beneath sea floor. The ability of the CUESI to identify buried shell deposits was one of the main goals of the system design. CUESI ability to identify shell porosity values, which would be unique, can aid in narrowing down areas to target for testing based on remote sensed data. The pseudosection shown in Figure 16 includes only porosity values pulled from the CUESI data. The location over core B4 shows a porosity value of 68.8%, an almost exact match for the modelled porosity volume of the core sample, measured at 69%. Additional processing of these data can help to clarify these finding. In future surveys, the CUESI system could potentially generate porosity maps for further investigation or identify areas with little consolidation, which is valuable to offshore infrastructure projects.
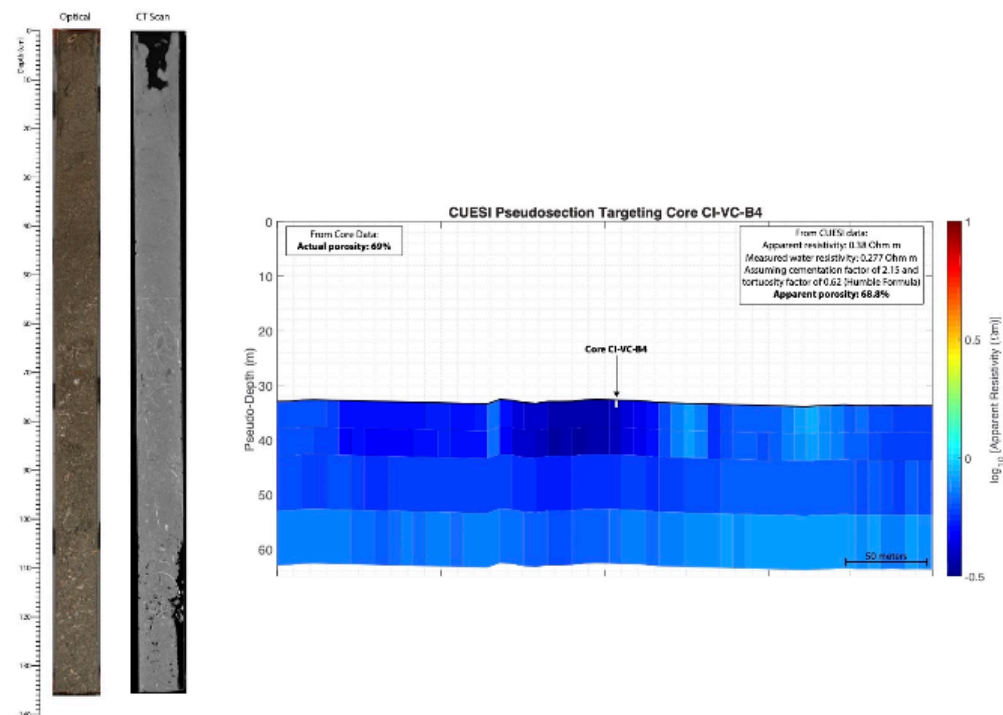
Figure 16: Left: Split core with shell deposit starting at ~55 cm. Right: This pseudosection highlights the sensitivity of the CUESI system toward characterizing changes in seafloor porosity that can aid in identifying shell middens which are predicted to have a higher pore volume than typical marine sediment. Image by Roslynn King.

The results of the field tests as well as the data collection on the subsequent project show that the CUESI system may be a beneficial addition to remote sensing data surveys focused on identifying targets on submerged paleolandscapes. CUESI collects altimeter, pressure, conductivity, and temperature data as designed. These data provide conductivity profiles both vertically and laterally through the water column that can aid in identifying seafloor seepage (either through changes in temperature or conductivity) and stratified water columns. The altimeter and pressure data, when processed and combined, can create high-resolution (.5 meter lateral resolution and 10 cm vertical resolution) bathymetric profiles. These datasets are useful toward building accurate starting models for, thereby reducing error in, later inversions. Additionally, the response data from the receiver towfish can be used to create resistivity pseudosections of the upper 40 m of seafloor material. These data and pseudosections can be used to identify possible changes in porosity in the seafloor (Figure 16), lithics (Figure 15), or hydrocarbons (Figure 12). Resolution and sensitivity to these targets could be improved by collecting more sets of higher resolution navigational data as well as incorporating phase data. Efforts to use this data in 2D inversions are still underway.

Incorporation of the camera on the CUESI system shows promise, though modifications are needed. The camera collected thousands of photos of the seafloor during a dive on 26 September 2021. The camera later malfunctioned due to power interruptions, which will be addressed in future lab tests. The lights associated with the camera provided adequate light when the system was within 5 m of the seafloor. Many of the photos were out of focus due to the adaptive focal settings on the camera; this will be addressed by setting a permanent focal distance for future surveys.

The design of CUSEI to be deep-towed is integral to the success of the system. This design included a drop weight with the transmitter electric dipole and receiver towfish 1 to 2 meters (or within 5 m) above the seafloor with minimal contact with the seafloor. The navigational data collected on 26 September 2021 demonstrates that the transmitter electric dipole and receiver towfish maintained an altitude of 1 to 2 meters above the seafloor. Additionally, the navigational data indicates that CUESI functioned effectively as a drop weight as little wave noise was recorded on the transmitter electric dipole and receiver towfish. These data also show that CUESI is able to generate a consistent current controlled signal between 1 to 5 amps and these signals propagate to the receivers in a predictable manner. Further analysis of receiver data may help better understand the stability of this signal and could help improve modeling efforts.

## 6. Conclusions

The CUESI system was initially developed as a novel bottom-towed CSEM system to survey the immediate seafloor and shallowly buried features on the continental shelf with minimal impact of the seafloor substrate and benthic community. A major goal of the datasets and models generated by this system were to map changes in porosity that could be indicative of shell middens left from human occupation. To achieve a level of sensitivity to image middens, the system would need to generate small EM signals and the receivers would need to 'flown' within 5 m of the seafloor and be highly sensitive to minor perturbations in the electric field. Reducing seafloor impact and maintaining a consistent altitude above the seafloor would require precise control of instrument buoyancy and ship speeds. Additionally, from forward models, the presence of middens generates a small fluctuation, around 5% total change in recorded signal, in the electric field. Therefore, all sources of noise, especially navigational noise need to be below this threshold. The influence of navigational error on the final resistivity models can be minimized by collecting accurate and high-density navigational data.

Through several iterations, test cruises, and pier tests, the functionality and data collected by the CUESI system has significantly improved and sensitivity to changes in porosity is apparent. CUESI was used to collected data on a subsequent project and these data appear, at least in initial processing, to be effective at identifying a known lag deposit. CUESI was also able to effectively locate modelled porosity of a core sample with a shell deposit, and a known tar seep. These results suggest that CUSEI may be an

effective system for consideration in surveys focused on identifying features across paleolandscapes that may narrow target selection for subsequent sampling. This selection can create a more efficient process to collect data germane to geological, biological, and paleontological disciplines, and narrow search parameters to identify archaeological "hot spots'' on the continental shelf. These data are crucial in our ability to identify sensitive cultural landscapes and eventually identify, document, and preserve underwater cultural heritage resources.

## 7. Acknowledgements

## 8. References

Archie, G.E., 1942. The electrical resistivity log as an aid in determining some reservoir characteristics. *Transactions of the AIME*, *146*(01), pp.54-62.

Clark, J., J.X. Mitrovica, and J. Alder. 2014. Coastal Paleogeography of the California–Oregon–Washington and Bering Sea Continental Shelves During the Latest Pleistocene and Holocene: Implications for the Archaeological Record. *Journal of Archaeological Science* 52:12-23.

Constable, S.C., Parker, R.L. and Constable, C.G., 1987. Occam's inversion: A practical algorithm for generating smooth models from electromagnetic sounding data. *Geophysics*, *52*(3), pp.289-300.

Erlandson, J.M. 1994. Early Hunter-Gatherers of the California Coast. Springer, New York.

Erlandson, J. M., T. C. Rick, T. J. Braje, M. Casperson, B. Culleton, B. Fulfrost, Tracy Garcia, D. Guthrie, N. Jew, D. Kennett, M. L. Moss, L.Reeder, C. E. Skinner, J. Watts, L. M.

Willis. 2011. Paleoindian Seafaring, Maritime Technologies, and Coastal Foraging on California's Channel Islands. *Science* 441:1181-1185.

Gusick, A.E. and J.M. Erlandson. 2019. Paleocoastal Landscapes, Marginality, and Initial Settlement of California's Islands. In, An *Archaeology of Abundance: Re-evaluating the Marginality of California's Islands*, edited by K. Gill, J. Erlandson, and M. Fauvelle, pp. 59-97. University of Florida Press, Gainesville.

Gusick, A.E., J. Maloney, T. Braje, and J.M. Erlandson. 2021. Above and Below the Waves: Advances in the Search for a Late Pleistocene Colonization of California's Islands. In, *The Archaeology of Island Colonization: Global Approaches to Initial Human Settlement*, edited by M. Napolitano, J. Stone, B. Dinapoli, pp. 105-131. University Press of Florida, Gainesville.

Key, K. and Ovall, J., 2011. A parallel goal-oriented adaptive finite element method for 2.5-D electromagnetic modelling. *Geophysical Journal International*, *186*(1), pp.137-154.

Key, K., 2012. Marine EM inversion using unstructured grids: a 2D parallel adaptive finite element algorithm. *SEG Technical Program Expanded Abstracts 2012*. Society of Exploration Geophysicists. pp. 1-5

King, R., Maloney, J.M., Constable, S., Gusick, A.E., Braje, T., Ball, D., 2018. Feasibility of detecting submerged landforms, and archaeological resources using controlled source electromagnetic methods. Poster presented at the American Geophysical Union Annual Meeting, Washington D.C.

Rick, T.C., J.M. Erlandson, R.L. Vellanoweth, and T.J. Braje. 2005. From Pleistocene Mariners to Complex Hunter-Gatherers: The Archaeology of the California Channel Islands. *Journal of World Prehistory* 19(3):169-228.

Sherman, D., Kannberg, P. and Constable, S., 2017. Surface towed electromagnetic system for mapping of subsea Arctic permafrost. *Earth and Planetary Science Letters*, *460*, pp.97-104.